Elucidation of Anode Reaction of Magnesium Rechargeable Batteries by *operando* Soft X-ray Absorption Spectroscopy

Masashi Hattori

Elucidation of the Anode Reaction of Magnesium Rechargeable Batteries by *operando* Soft X-ray Absorption Spectroscopy

Masashi Hattori

Department of Interdisciplinary Environment,

Graduate School of Human and Environmental Studies,

Kyoto University

Contents

..

Chapter 1: General Introduction

1.1 Background

Currently, depletion of fossil fuels such as oil and natural gas, which are major energy sources, is a worldwide issue. Further, there is concern about global warming caused by CO_2 emitted when using fossil fuels.[1] In addition, interest in environmental and energy problems has increased in recent years. For these reasons, it is essential to develop new energy sources to replace fossil fuels.

Renewable resources, such as sunlight, geothermal power, and wind power, are potential candidates for new energy sources.[2,3] However, since renewable energy depends on the season and the weather, the output varies. To stabilize output, attention has been focused on energy storage media, such as rechargeable batteries. Among rechargeable batteries, lithium ion rechargeable batteries, which have high energy densities and high output densities, are considered most promising.

1.2 Current lithium ion rechargeable batteries

In 1976, Whittingham discovered that lithium ions reversibly intercalate/deintercalate into TiS_2 through an electrochemical reaction in the Li/TiS_2 system.[4,5] This discovery formed the basic concept for lithium ion batteries in which topochemical reactions are used.[6] Lazzari and Scrosati developed a Li_xWO_2/TiS_2 system consisting of two insertion electrodes based on obtaining Li_xWO_2 electrochemically by inserting lithium ions into a WO_2 anode.[7] Mizushima *et al.* have reported that $LiCoO_2$ with a layered rock salt structure shows reversible intercalation/deintercalation of lithium ions, with an open circuit voltage of Li_xCoO_2 after extraction of lithium of about 4 V vs. lithium metal.[8] In 1987, Auborn and Yazami proposed $LiCoO_2/MoO_2$ and $LiCoO_2/WO_2$ systems as lithium ion intercalation cells without lithium metal.[9,10] A few years after the discovery of Whittingham, the $LiCoO_2$/graphite-based lithium ion battery developed by Yoshino was first commercialized by Sony in 1991. A schematic diagram of a lithium ion battery is shown in Figure 1-1.[3] Lithium ion batteries include an anode, an electrolyte (in a separator), and a current collector. The cathode and the anode are isolated by an electrolyte. For a typical $LiMO_2$ (M: transition metal)/graphite cell, as shown in Figure 1-2, the operating principle can be described as follows. In the discharge process, lithium ions are simultaneously extracted from graphite and solvated with a solvent in the electrolyte. The solvated lithium ions migrate to the $LiMO_2$ side, where they are simultaneously desolvated and inserted into $LiMO_2$. When $LiMO_2$ receives lithium ions from the electrolyte, it also receives electrons from an external circuit. Each electrode reaction and the total reaction for the discharge process are represented by the following equations:

Anode $Li_xC_6 \rightarrow C_6 + xLi^+ + xe^-$

Cathode $Li_{1-x}MO_2 + xLi^+ + xe^- \rightarrow LiMO_2$

Total $Li_xC_6 + Li_{1-x}MO_2 \rightarrow C_6 + LiMO_2$

In the charge process, the reverse reaction occurs.

Modern lithium ion rechargeable batteries hold more than twice the energy of the first commercial system sold by Sony in 1991;[11] however, to further improve the performance of the reaction occurring in lithium ion battery cells, it is necessary to understand the mechanism. Reactions within battery cells are divided into three groups according to the space–time scale. The largest scale response occurs at the composite electrode. The composite electrode is composed of an active material, a conductive additive (carbon), and a binder, which form a complicated structure. In the composite electrode, there is considerable internal resistance related to electron conductivity and ion conductivity. As the electrode reaction occurs preferentially in regions of lower resistance, a reaction distribution is generated within the composite electrode.[12-16] This reaction distribution greatly affects battery performance characteristics, such as safety and circulation. The reaction on the second largest scale occurs in the active material. There are many active materials that have various crystal structures.[17-19] The crystal structure is modified by the lithium ion extraction/insertion reaction, leading to phase transitions.[20,21] Battery performance parameters, such as energy density and durability, are largely affected by the crystal structure and/or phase transition behavior of the active material.[17,18,22-24] The reaction on the smallest scale occurs at the anode/electrolyte interface. When lithium ions are inserted into or extracted from the active material, a charge transfer reaction occurs at the interface. As the interfacial reaction is the basis for all reactions occurring in the battery, it greatly affects performance characteristics, such as power density and durability.[25,26]

1.2.1 Cathode materials

Various compositions have been investigated as cathode materials, including the presently used layered rock salt type oxides. Ni–Co-type, Ni–Co–Mn-type, and Ni–Mn-type materials have also been proposed, which have theoretical capacities of about 300 mAh g^{-1}. In the 4 V region, the spinel structure of $LiMn_2O_4$ and the olivine structure of $LiFePO_4$ have capacities of about 150 mAh g^{-1}. The positive electrode material has limited the increase in capacity of lithium ion rechargeable batteries.

Lithium cobalt oxide ($LiCoO_2$) has a layered rock salt type (α-$NaFeO_2$ type) structure (space group: R-3m). In this structure, oxide ions form a face centered cubic close-packed lattice structure. Lithium ions are alternately arranged at the octahedral position on one side of this oxide ion structure and cobalt ions are alternately arranged at the opposite octahedral position. That is, lithium ions are present between layers of CoO_6 octahedra. In 1980, Mizushima e*t al.* showed that $LiCoO_2$ exhibits a potential of 4 V vs. lithium metal and that lithium ions can be reversibly inserted/extracted for compositions of $LiCoO_2$ to $Li_{0.4}CoO_2$ (3.8–4.3 V vs. Li^+/Li),[8] with a theoretical capacity of 274 mAh g^{-1} for $LiCoO_2$. During the initial charge of $LiCoO_2$, a two-phase reaction of two hexagonal phases progresses, and the composition–OCV curve shows a plateau.[27] When the amount of extracted lithium ions exceeds 0.5, a phase transition to a monoclinic system occurs, which corresponds to a small plateau around 4.1 V. The monoclinic crystal has the same basic skeleton as the original hexagonal crystal, but the stacking of the oxide layers is shifted. Therefore, the reversibility of the cell reaction is maintained. Increasing the number of extracted lithium ions to 0.5 or more causes a phase transition from a monoclinic to a hexagonal system, and the reaction results in decomposition.[28] Therefore, the crystal structure cannot be maintained, so 120–130 mAh g^{-1} can only be used as batteries.[29] In addition, as cobalt is expensive, highly toxic, and has few reserves, inexpensive and safe materials are being sought to replace Co.

Unlike the layered structures of the above-mentioned materials, the three-dimensional skeleton of $LiMn_2O_4$ has a cubic spinel structure (space group: Fd3m).[30] In $LiMn_2O_4$, position 8a of the cubic space group Fd3m corresponds to Li^+, position 16d corresponds to trivalent and tetravalent Mn, and position 16c corresponds to vacancies. One-dimensional diffusion of lithium proceeds in a zigzag manner along the 8a→16c diffusion path (8a→16c →8a→16c), where the 16c site is an empty octahedral position immediately adjacent to the 8a site.[31] $LiMn_2O_4$ shows two plateaus (in the 4 V region and the 3 V region), but two-phase coexistence of cubic $LiMn_2O_4$ and tetragonal $Li_2Mn_2O_4$ occurs in the 3 V region. As tetragonal $Li_2Mn_2O_4$ is formed in this region, a large volumetric expansion occurs and this material does not exhibit cycle characteristics that can withstand practical use.[32] Advantageously, Mn is an inexpensive, resource-rich material, allowing a stable supply of materials, but the cycle characteristics of $LiMn_2O_4$ are inferior to those of $LiCoO_2$ and Mn is ejected into the electrolyte under high temperature conditions. In order to solve these problems, capacity is reduced, but substitution with various kinds of dissimilar metals (Co, Cr, Al, Ni, Fe, etc.) has been made to improve cycle characteristics.[33,34]

Polyanion materials include tetrahedral XO_4 (X = P, Si, S, etc.) in their crystal structures. As this polyanion unit does not participate in the charge–discharge reaction, the theoretical capacity is lower than that of oxide materials such as $LiCoO_2$ and $LiMn_2O_4$. However, the structure is stable owing to the effect of this polyanion unit. The resulting high thermal stability of makes it is possible to react all Li^+ in such compounds. Numerous polyanion compounds have been reported as positive electrode materials for lithium ion rechargeable batteries and $LiFePO_4$ is described here as a representative material.

$LiFePO_4$ is an olivine-type positive electrode material with a polyanion structure containing iron as the main component, as reported by Padhi *et al.* Iron has the fourth highest Clarke value, and as resources of this element are abundant, a stable supply of materials is possible and the cost can be reduced to 1/100 of that of Co. In addition, the permissible amount of iron in exhaust gas is about 100 times that of cobalt, and the environmental compatibility is also excellent.[21] The theoretical capacity of $LiFePO_4$ is 170 mAh g^{-1} and the reaction potential is 3.4 V vs. Li^+/Li, whereas the real capacity of $LiCoO_2$ is 137 mAh g^{-1} and the reaction potential is 3.7 V vs. Li^+/Li. Thus, a sufficient energy density can be expected vs. lithium metal. The crystal structure of $LiFePO_4$ is an orthorhombic system (space group: Pnma (62)). The basic structure is a hexagonal close-packed structure of oxide ions, in which metal cations occupy half of the octahedral sites and P occupies 1/8 of the tetrahedral sites. The FeO_6 octahedra are connected in a zigzag manner by vertex sharing to form a layer parallel to the *bc* plane. Lithium atoms in octahedral sites form a chain along the *b* axis by ridge sharing, and lithium ions diffuse in the direction of this chain.[35-37] This material exhibits a plateau in a wide composition range, with a two-phase coexistence reaction of $LiFePO_4$ and $FePO_4$ occurring in this region. Solid solution reactions progress in other regions, and the solid solution region tends to expand with decreasing grain size.[38]

$LiFePO_4$ is an olivine type positive electrode material having a polyanion structure containing Fe as a main component reported by Padhi *et al.* Fe is the fourth largest element of Clarke, and since resources are abundant, stable supply of materials is possible, and the cost can be suppressed to 1/100 times of Co. Also, the permissible amount in the exhaust gas is about 100 times that of Co, and the environmental compatibility is also extremely excellent[21]. The theoretical capacity of $LiFePO_4$ is 170 $mAhg^{-1}$, the reaction potential is 3.4 V vs. Li^+/Li, the real capacity of $LiCoO_2$ is 137 $mAhg^{-1}$, the reaction potential is 3.7 V vs Li^+/Li. A sufficient energy density can be expected compared with Li^+/Li. The crystal system of $LiFePO_4$ is orthorhombic system. The space group belongs to Pnma (62). The basic structure is the hexagonal close-packed structure of oxide ions, the metal cation occupies half of the octahedral site, and the typical element P occupies 1/8 of the tetrahedral site. The FeO_6 octahedron is connected to the zigzag by the vertex sharing and forms a layer parallel to the bc plane. Li existing in the octahedral site forms a chain in the direction of the b axis by ridge sharing, and Li diffuses in the direction of this chain[35-37]. This material exhibits a plateau in a wide composition range, and in this region it is proceeding in a two-phase coexistence reaction of $LiFePO_4$ and $FePO_4$. Solid solution reaction progresses in other ranges. Solid solution region tends to expand with decreasing grain size[38].

1.2.2 Electrolytes

The theoretical values of the capacity and the energy density, which are the basic performance parameters of a battery, depend on the cathode material and the anode material. The electrolyte is also a critical component of batteries, but it does not directly contribute to the energy density. In practical batteries, the electrolyte often determines fundamental performance parameters such as the output characteristics and lifetimes of batteries, and optimization of the electrolytes is an extremely important process. The performance requirements for the electrolyte of lithium ion batteries are as follows.

(1) High ion conductivity over a wide temperature range.

(2) Electrolytes contain lithium ions and have a high ion transport rate.

(3) Electrochemically stable in a wide potential range.

(4) Electrolytes do not inhibit the electrochemical reaction between the positive electrode and the negative electrode.

(5) High thermal stability.

Since the operating voltage of lithium ion rechargeable batteries is as high as 3.6 V and exceeds the electrochemical potential window of water (1.23 V), it is impossible to use aqueous electrolytes. For this reason, organic electrolytes (in which a lithium salt is dissolved in an organic solvent) that can withstand a high voltage are currently used. Physical properties and structures of major organic solvents proposed for electrolytes for lithium ion rechargeable batteries. The necessary properties of the electrolyte solvent are as follows. The solvent must dissolve the lithium salt to give high ionic conductivity and a high transportation rate, and it must not react with the electrode. Therefore, it is desirable that the solvent has a wide potential window, a high dielectric constant, and a low viscosity. Further, parameters such as the melting point and boiling point of the solvent directly affect the operating temperature range of the battery. It is desirable to maintain the electrolyte in a liquid state not only at room temperature, but also at low temperatures of around -20°C.

Typically, electrolytes in current lithium ion rechargeable batteries consist of a lithium salt (~1 mol dm^{-3}) dissolved in a solvent with a high dielectric constant and a relatively wide potential window. Ethylene carbonate (EC) has a high dielectric constant and high stability against oxidation and reduction. Further, it has been used as a solvent for lithium ion rechargeable batteries in order to form a surface coating (solid electrolyte interface; SEI) capable of intercalating/deintercalating lithium ions in carbon-based negative electrodes. However, owing to its high melting point, EC is solid at room temperature and has high viscosity and low ionic conductivity. Therefore, EC alone cannot be used as a solvent, and mixtures of EC and dimethyl carbonate (DMC), diethyl carbonate (DEC), ethyl methyl carbonate (EMC), or similar linear carbonates with low melting points and low viscosities are used instead.

The solute is a salt that dissolves in solvents and dissociates to give Li^+. There are many lithium salts, but many have high ion conductivity and wide potential window. Further, the solute has considerable influence on the shape of the SEI. The combination of EC and lithium hexafluorophosphate ($LiPF_6$) forms a good SEI for carbon-based negative electrodes as compared with the combination of EC and lithium tetrafluoroborate ($LiBF_4$). In addition, as $Li(CF_3SO_2)_2N$ (LiTFSA) corrodes Al, which is commonly used as a cathode current collector, it is not suitable as a solute. From the above viewpoints, $LiPF_6$ is typically used owing to its wider potential window and better SEI shape. However, $LiPF_6$ reacts with water to generate hydrofluoric acid (HF), which causes degradation. In addition, $LiPF_6$ has poor thermal stability and disadvantageously, the solvent is decomposed by PF_5 produced by degradation.

Since the ionic conductivities of organic electrolytes are as low as about 10 mS cm^{-1}, the separator holding the electrolyte and the electrode are manufactured to be as thin as possible to reduce ohmic loss. While the electrode thickness in lead storage batteries with an aqueous sulfuric acid solution of high ionic conductivity is on the order of millimeters, the electrode thickness of lithium ion rechargeable batteries is on the order of microns.

The solvent is strongly coordinated to Li^+ in the electrolyte; therefore, the radius of solvated Li^+ is larger than that of the anion, causing large resistance during movement. Therefore, the Li^+ transport rate of the electrolyte is low (below 0.3). A concentration distribution occurs in the electrolyte owing to the low transportation rate of Li^+.

There are safety issues associated with organic electrolytes, as organic solvents are flammable. Research and development of flame-retardant/nonflammable electrolytes have been actively conducted in order to guarantee the safety of the entire battery toward the development of larger batteries for electric vehicles and similar applications. Since being reported by Wright in 1975, polymer electrolytes have been widely studied for all-solid-state lithium ion rechargeable batteries.[39] However, the conductivity is high and it is about 1 mS cm^{-1} or less, which is 1 or more digits inferior to the organic electrolyte. Therefore, the transportation rate of Li^+ is inferior in polymer electrolytes. Ion conductors with a transmission rate of 0.75 have also been reported. However, the conductivity of 10^{-5} mS cm^{-1} is three orders of magnitude lower than those of organic electrolytes.[40] Furthermore, when a solid electrolyte is used. The reaction takes place at the solid/solid interface. If a good solid/solid interface cannot be constructed, the number of reaction sites decreases and the charge transfer resistance is large. Many aspects of the mechanism of Li^+ migration at the solid interface are unknown, and it is the present situation that the interfacial formation with performance that can withstand practical use has not been reached. Research and development of all-solid-state lithium ion rechargeable batteries using inorganic solid electrolytes other than polymer electrolytes have also attracted attention in recent years.[41,42]

1.2.3 Anode materials

It is desirable for negative electrode active materials to have as low as possible a potential and a small electrochemical equivalent. In addition, it is preferable that the constituent elements are found in large quantities in nature. Graphite is the mainstream material currently used for negative electrodes in lithium ion secondary batteries. Alloy-based negative electrodes which have high capacity in recent years and have reduced defects of the lithium metal and current lithium ion batteries. We describe materials that carry out charge–discharge reactions by conversion reactions other than insertion/extraction of Li^+.

Graphite is a layered compound consisting of hexagonal network graphene sheets, which are formed of strong conjugated sp^2 bonds, laminated together by van der Waals forces. During the insertion/extraction reaction of Li^+, the conjugated sp^2 bonding network on the graphene surface does not change significantly.

The Li^+ insertion capacity of the graphite negative electrode is relatively large with capacity densities per weight and volume of 372 mAh g^{-1} and 855 mAh L^{-1}, respectively, and a potential window of 0.07–0.23 V (vs. Li^+/Li). As a negative value almost equal to that of the lithium negative electrode is achieved, a battery system with a high voltage can be expected. Further, since the reversibility of the Li^+ insertion/extraction reaction is very high, the graphite electrode is widely used as a negative electrode in lithium ion rechargeable batteries. In addition, as carbon materials are low cost and have small environmental burdens, graphite is a very attractive battery material.

From the viewpoint of capacity, it is also desirable to use lithium metal as a negative electrode material. However, lithium metal has the disadvantages of dendrite formation during the charge–discharge reaction. In order to solve this problem, the use of lithium alloys has been proposed. If the surface of the electrode is not lithium, it is considered that dendrites will not be generated and internal short circuits can be prevented.

Various metals, such as Sn, Pb, Al, Zn, Bi, Ga, In, and Si, have been investigated in alloy systems. In particular, as Li–Si alloys and Li–Sn alloys have high theoretical capacities of 4000 and 1000 mAh g^{-1}, respectively, there has been considerable active research and development of these materials in recent years. The capacities of these alloy systems are much higher than those of graphite-based materials.

A major disadvantage of alloy-based negative electrodes is the phenomenon of electrode pulverization owing to the severe volume change that accompanies occlusion and release of a large amount of lithium. Therefore, research and development toward the practical application of alloy-based negative electrodes includes the fabrication of matrices with an element that does not react with lithium-retaining reactive elements[43] and achieving fine form control to increase the reaction amount.[44] Further development of such alloy-based negative electrode materials are expected owing to the possibility that high capacities can be achieved for systems in which deposition/dissolution reactions of a metal negative electrode are not used.

1.3. Beyond the lithium ion batteries

Recently, lithium ion rechargeable batteries with high energy densities have been expected to be used as power sources for electric storage combined with renewable energy, such as in electric vehicles. However, lithium ion rechargeable batteries have problems associated with energy density, material cost, and safety. When full-scale installation in electric vehicles is considered, it has been estimated that a very high energy density of about 500 Wh kg^{-1} will be necessary to realize cruising distances as high as those of current gasoline powered vehicles. However, the performance of lithium ion rechargeable batteries is insufficient and the, development of innovative rechargeable batteries is required. Therefore, as shown in Figure 1-2, studies of metal–air rechargeable batteries and metal negative electrode batteries have attracted attention as post-lithium ion rechargeable batteries with the aim of achieving high capacities and high energy densities.[45]

1.3.1 Metal-air battery

Metal–air batteries are batteries that use oxygen (air electrode) in air as the positive electrode active material and metal for the negative electrode. In such batteries, it is unnecessary to encapsulate oxygen for the positive electrode active material, as air from the surrounding environment is taken in during discharge. Therefore, the interior of the battery container is mostly occupied by the negative electrode active material, and the theoretical capacity far exceeds that of lithium ion secondary batteries.[46-48] In addition, the oxidizing power of oxygen as the positive electrode active material is strong, the electromotive force is relatively high, and a high theoretical energy density can be realized.

However, reducing the metal oxide generated by reaction with oxygen requires a large overvoltage, which has become a major problem for making rechargeable batteries.[49]

1.3.2 Lithium-sulfur battery

Lithium–sulfur batteries are storage batteries that use a sulfur compound as the positive electrode material. The theoretical capacity per weight is very large at 1672 mAh g^{-1}, and it is expected to be a high capacity positive electrode for the next generation of storage batteries. In addition, since sulfur is an abundant byproduct of petroleum refining as well as a common natural resource, its use is advantageous from the viewpoint of cost. Further, as the compound has a wide range of oxidation numbers from -2 to 6, sulfur is also advantageous for material design. There are also advantages such as the abundance of options. When an organic electrolytic solution is used, lithium polysulfides flow into the electrolytic solution from the negative electrode and an insulating sulfide coating is formed on the positive electrode; therefore, there is concern about capacity deterioration owing to active material loss from the electrode. At present, attempts are being made to prevent such sulfides from flowing out of the electrode by using inorganic solid electrolytes.

1.3.3 Multivalent cation batteries

There have been various reports on metal negative electrode secondary batteries using multivalent ions as carriers, calcium secondary batteries with Ca^{2+} as carriers,[50-53] zinc rechargeable batteries with Zn^{2+} and Y^{3+} as carriers,[53-55] aluminum rechargeable batteries using Al^{3+} as carriers, and magnesium secondary batteries[52,55-59] using Mg^{2+} as carriers. Of these, magnesium rechargeable batteries have attracted the greatest amount of attention for reasons described later. Below is a summary of magnesium rechargeable batteries reported up to now and the current state of development in this research area.

We have focused on metal anode rechargeable batteries as next-generation battery system. Table 1-1 shows a comparison of the characteristics of various negative metal anodes.[60] The theoretical gravimetric and volumetric capacities assume that the following reaction occurred.

$$\mathrm{M}^{x+} + x\mathrm{e}^{-} \Leftrightarrow \mathrm{M} \tag{1-1}$$

A high energy density is an indispensable requirement for post-lithium ion rechargeable batteries. The energy density is expressed by the integral of the battery potential and the capacity during charge and discharge. Thus, it is desirable that the negative anode has a high capacity and a relatively low reduction potential. Rechargeable batteries with a magnesium metal anode are expected to have high energy densities because magnesium metal has high theoretical gravimetric and volumetric capacities with a relatively low reduction potential. In particular, the theoretical volumetric capacity of magnesium metal is about twice that of lithium metal, which is advantageous because it allows packing of a large amount of material in a limited space, such as in rechargeable batteries for electric vehicles. Furthermore, as shown in Table 1-1, the abundance of magnesium reserves makes it possible to solve the problems of resource depletion and cost. Magnesium metal has a melting point of about 650°C, which is much higher than those of lithium metal (180°C) and sodium metal (98°C). The melting point is an index of the stability of a metal, rechargeable batteries using magnesium metal can be expected to have improved safety. The safety of metal anodes is a very important factor for future practical applications. In addition, since lithium metal and sodium metal react violently with moisture in air, handling these metals is difficult. However, magnesium metal is stable in air and easy to handle. Overall, magnesium rechargeable batteries are good candidates for next-generation batteries.

1.4. Magnesium rechargeable battery system

1.4.1 Reported magnesium rechargeable battery cathodes

Initially, oxide cathode materials were reported for magnesium storage batteries. Gregory *et al.* conducted constant current cycles for several oxides.[61] Novak *et al.* reported pentavalent vanadium (V_2O_5) and trivalent molybdenum (MoO_3) as divalent cation insertion hosts.[62-66] Because it was influenced with strong mutual interaction between magnesium ions and oxide ions in the crystal lattice. Since sulfide materials are mainly poled over oxide ions, we focus on the application of cathode materials for magnesium storage batteries.

Sulfides with layered structures, such as TiS_2 and MoS_2, are well-known magnesium ion insertion materials.[67,68] In addition, sulfides have been reported as cathode materials for magnesium batteries.[61,66,69-71] Among sulfide cathode materials, magnesium ions can be reversibly inserted into two Chevrel phases, and the sulfide Chevrel structure (Mo_6S_8) has been reported as a prototype for magnesium storage battery system. The crystal structure of the Chevrel phase of Mo_2S_8 is shown in Figure 1-3. This host structure has 12 magnesium ion insertion sites, which are divided into two different sites called inside and outside sites (Figure 1-3).[72,73] In addition, it is easy to transfer guest cations between these sites.[73] The Chevrel phase has a stable structure for certain contents of guest cations, redistribution occurs. This material shows relatively high rate performance and good cycling ability among the reported cathode materials for magnesium storage batteries. However, the theoretical capacity and the cathode potential are relatively low (about 128.8 mAh g^{-1} and 1.1 V vs. Mg^{2+}/Mg, respectively). Thus, new high capacity and high potential cathode materials are essential to achieve high energy density battery systems.

One candidate material for magnesium storage battery cathodes is V_2O_5.[61,63,69,74] The theoretical capacity of this material is very high (about 589 mAh g^{-1}), and this material has large spaces in the crystal structure. As an insertion host in the cathode of magnesium rechargeable batteries, polycrystalline V_2O_5 has a capacity of about 150 mAh g^{-1} ($Mg_{0.5}V_2O_5$) at 150°C.

Unfortunately, this material shows poor reversibility.

Novak *et al.* showed reversible electrochemical cycling of V_2O_5 in magnesium ion containing electrolytes.[75] In this experiment, the electrolyte contained water and the obtained capacity was correlated with the amount of water in the electrolytic solution. The water molecules solvated the magnesium ions in the electrolyte to shield the charge of the magnesium ions. These solvated magnesium ions could be inserted easily into a large layer of V_2O_5 and a capacity of about 200 mAh g^{-1} was obtained. Imamura *et al.* recently prepared a complex of V_2O_5 xerogel and carbon.[76] This material showed a very large discharge capacity and relatively good cycling performance. The structure of the V_2O_5 xerogel is shown in Figure 1-4.[77] Three holding thin plate structures were constructed by *ab* plane of orthorhombic V_2O_5 sheet. his lamellar structure contains water molecules. Since this structure exhibits a two-step electrochemical reaction, there is a large space between the 11.5 Å layers, as well as two different insertion sites for magnesium ions, called site a and site b. Site a is near the center of site squared oxygen atom and site b is near a vertex oxygen atom.[78]

The V_2O_5 xerogel shows high performance as a cathode material for magnesium rechargeable battery systems. However, as a passivation film is easily formed on magnesium metal in the presence of water, this water-containing material cannot be applied to actual magnesium storage systems.[79] In addition, other materials with large spacing, such as hollandite- type MnO_2, have been studied.[80] The material undergoes a conversion reaction in which a magnesium ion is inserted into the host structure to produce inactive MgO.[81]

Another approach to high capacity cathode materials is the use of nanostructured materials.[82-86] Nanosheet structures show adsorption/desorption of guest cations during charge–discharge reactions. This mechanism does not require intercalation sites in the active materials and does not suffer from the slow diffusivity of magnesium cations. Liang *et al* achieved a voltage of 2.0 V and a capacity of ~150 mAh g^{-1} by using graphene-like MoS_2 as a cathode material.[86] However, for high energy density battery systems, this capacity and voltage are still low.

Recently, other oxide host materials have ben reexamined as a cathode material for magnesium rechargeable batteries. One of these important materials is a spinel-type oxide and the other is a polyanionic compound.[87,88] The spinel-oxide-based material is an excellent positive electrode material in lithium ion rechargeable batteries. The crystal structure of spinel $LiMn_2O_4$ is shown in Figure. 1-5. In lithium ion rechargeable batteries, this structure has a three-dimensional diffusion path,[87] and density functional theory (DFT) calculations indicate that this spinel oxide is a suitable intercalation host from the viewpoint of cation migration in the host structure.[89] Energy densities exceeding those of lithium ion rechargeable batteries can be achieved.[84] The insertion of magnesium ions into a spinel host was first reported by Luis *et al*.[90] They conducted constant current measurements for a mixed manganese–cobalt oxide spinel. This host material showed a relatively high potential (about 2.9 V vs. Li^+/Li) and good reversibility, but the capacity was only 30 mAh g^{-1}. Recently, the Mn_2O_4 spinel oxide host showed a large volume capacity (about 545.6 mAh g^{-1}) in aqueous solution (0.5 mol dm^{-3} $MgCl_2$ in H_2O).[91,92] In addition, magnesium ions were inserted into spinel oxide hosts using several transition metal cations in molten salt electrolytes based on a salt of bis(trifluoromethanesulfonyl) imide.[93]

Polyanionic compounds can also act as oxide host, and this type of material has been applied as a cathode material in lithium ion secondary batteries. Olivine-type $LiFePO_4$ is a commercialized cathode material for lithium ion rechargeable batteries that can be delithiated with high structural stability of the host structure.[94] This material belongs to Pnma space group and Fe^{4+}. The position of the shared octahedron, and Li^+ located in the chain of octahedral sites sharing edges. This stable structure is expected to be maintained during magnesium ion insertion/extraction reactions. In addition, polyanionic units, such as PO_4, have transition metal induction effects, and these types of materials exhibit relatively high potentials. This effect is caused by binding between the transition metal M and the ligand X. As the ionic strength of the M–X bond increases, the energy of the transition metal orbital decreases. The open circuit potential of these materials is then increased relative to that of the nominal transition metal oxide material, and the potential can be adjusted by changing the electronegativity of the polyanionic species.[95] Thus, the application of polyanionic compounds has several advantages in cathode materials. Up to now, several polyanionic materials have been reported for magnesium storage batteries. Makino *et al*. reported $Mg_{0.5}Ti_2(PO_4)_3$ as an insertion host for magnesium ions.[96] This substance is 1.2 magnesium ion (about 160 mAh g^{-1} in 1 mol dm^{-3} magnesium perchlorate ($Mg(ClO_4)_2$)/propylene carbonate (PC)). However, the extraction characteristics have not been reported and the oxidation–reduction potential of Ti is relatively low. Nuli *et al*. reported the application of olivine-type $MgMSiO_4$ (M = Mn, Fe, and Co) in positive electrode materials. They obtained reversible constant current charge–discharge curves with an average voltage of about 1.8 V, which is different from the theoretical value calculated by Ling *et al*. However, it has been clarified that olivine-type $MgMSiO_4$ (M = Mn, Fe, Co) cannot be applied as positive electrode materials for magnesium storage batteries. Finally, Orikasa *et al*. reported $MgFeSiO_4$, which is prepared by an ion exchange method, as a high-performance cathode material. This material shows high capacity and good cycling stability. Therefore, it is feasible to use polyanion compounds as magnesium rechargeable battery cathodes.

1.4.2 Reported magnesium rechargeable battery electrolyte and anode

Magnesium rechargeable battery electrolytes are required to have the following characteristics:

(1) Reversible magnesium metal deposition/dissolution reactions

(2) High ionic conductivity

(3) High thermal electrochemical stability

(4) High safety

Many studies have been conducted to obtain materials that satisfy the above conditions.

For magnesium rechargeable battery electrolytes, combinations of inorganic salts, such as $MgCl_2$ and $Mg(ClO_4)_2$, and organic solvents, such as tetrahydrofuran (THF), *N*,*N*-dimethylformamide, PC, and acetonitrile (AN), were investigated during the initial research and development stage.[98,99] However, the formation of passivation films on the surface of magnesium metal anodes was reported. Inherently, stable electrolytes do not exist in the presence of metals with strong reducing abilities, such as lithium or magnesium. Electrolyte decomposition occurred at the anode, even in lithium ion rechargeable batteries, and SEI was formed. Film formation differs for lithium and magnesium, as Li^+ diffusion is possible through the SEI formed in lithium electrolytes, whereas electrons and magnesium cannot pass through the coatings formed in magnesium electrolytes, which hinders magnesium metal deposition/dissolution reactions.[99] In addition, ether solvents did not form passivation films on the surface of magnesium metal in the open circuit potential state, and the reversibility of magnesium metal electrodeposition was inhibited by the decomposition of inorganic salts (ClO_4^- or $CF_3SO_3^-$) on the surface of the passivation films.[100]

Almost reversible magnesium metal deposition/dissolution reaction has been reported in systems with three kinds of magnesium organic salts: magnesium borides, Grignard reagents, and amide magnesium halides. THF is an aprotic solvent that is stable in the presence of magnesium metal in any system. Liebenow *et al*. examined the magnesium metal deposition reactions of *N*-methylanilylmagnesium bromide, pyrrylmagnesium bromide, and hexamethyldisilazide magnesium chloride ((HMDS)$MgCl_2$), which promotes delocalization of electron pairs by Si–N–Si bonds and improves oxidation resistance, in THF (Figure 1-6).[101] The N–Mg bonds in amide magnesium halide systems have higher polarizability than the R–Mg bonds in Grignard reagent systems, and thus amide magnesium halide systems exhibit different behavior than Grignard systems. Among the three amide magnesium salts, a reversible magnesium metal deposition/dissolution reaction was confirmed for pyrrylmagnesium bromide and $HMDSMgCl_2$. In particular, when $HMDSMgCl_2$ was used as the magnesium salt, the potential window for oxidation was widened by about 200 mV compared with that for ethyl magnesium bromide (EtMgBr, Et: ethyl) owing to the delocalization of the electron pair on N by the Si–N–Si bond. However, this system demonstrated inferior cycling characteristics for precipitation and dissolution, with only about 90% of coulombic efficiency obtained for each cycle.[100] In addition, it has been reported that each of these compounds has low ionic conductivity on the order of 10^{-1} mS cm^{-1}.

Many groups have reported that magnesium metal deposition/dissolution reactions proceed reversibly in electrolytes prepared by dissolving Grignard reagents (RMgX, where R = ethyl, butyl and X = Cl, Br) in THF.[100,102] Since no coating is formed in RMgX/THF, *in situ* Fourier transform infrared spectroscopy (FTIR) observations clarified that the magnesium metal deposition/dissolution reactions occur later.[103] However, these electrolytes have the disadvantage that the R–Mg bond in R–Mg–X is easily oxidized and decomposes at a low potential of about 1.7 V vs. Mg^{2+}/Mg.[81] In addition, as the ionic conductivity is one order of magnitude lower than that of the electrolyte for lithium ion rechargeable batteries, it is not appropriate for practical applications. In 2000, Aurbach *et al.* reported electrolytes represented by $R_xMgCl_{2-x} + R'_yAlCl_{3-y}$ (R, R′ = *n*-butyl and/or ethyl, x = 0–2, y = 0–3) in THF.[104,105] The electrochemical potential windows of these electrolytes were wider than those of conventional Grignard reagent systems (2.2 V vs. Mg^{2+}/Mg) and the ionic conductivity was similar to that of electrolytes for lithium ion rechargeable batteries. Further, dramatic performance improvement was observed for the magnesium metal dissolution reaction. For this electrolyte, the mechanism by which the characteristics were improved was elucidated by analysis of the dissolved ion species using nuclear magnetic resonance (NMR),[106] X-ray absorption fine spectroscopy (XAFS)[107] and Raman spectroscopy.[108] By ligand exchange reaction proceeds between Lewis acid

MgR_2 with Lewis base $RAlCl_2$, magnesium containing dissolved species in electrolyte $MgCl_2$, $Mg_2Cl_3^+$, changes in $MgCl^+$, while the $R_2AlCl_2^-$ anionic species, such as is produced.[108] In the proposed mechanism, the oxidation-susceptible R–Mg bond disappears owing to this ligand exchange, resulting in improved oxidation resistance. In this case, it is confirmed experimentally that R–Al bond in the R–Al–Cl dissolved species determines the anodic stability, and Highest Occupied Molecular Orbital (HOMO) prediction based on the first principle calculation.[106,107] R–Al bonds are believed to undergo oxidation by β-elimination to further improve the oxidation resistance. Aurbach *et al*. evaluated the characteristics of an electrolyte prepared using phenyl magnesium chloride (PhMgCl, Ph: phenyl), which has no hydrogen beta to the Lewis acid. Changing the Lewis acid from ethyl magnesium chloride (EtMgCl, Et: ethyl) to PhMgCl further improved the oxidation potential of the electrolyte (Et: 2.2 V ⇒ Ph: 3.3 V vs. Mg^{2+}/Mg), as shown Figure 1-7.[109] Among existing electrolytes for magnesium rechargeable batteries, PhMgCl has particularly excellent properties.

Nakayama *et al*. examined the solvation structure around magnesium by extended X-ray absorption fine structure (EXAFS) measurements in solution. The EXAFS analysis was based on the fact that Mg^{2+} adopts a six-coordinate structure in $Mg(ClO_4)_2/H_2O$, and that the Grignard reagent has a tetracoordinated dimer structure. This analysis, together with ^{25}Mg-NMR and ^{27}Al-NMR measurements, as well as first-principles calculations together, allowed the oxidation resistance of the electrolyte and the complex structure during magnesium metal electrodeposition to be determined.[107] See *et al.* reported that free Cl^- is absorbed on the electrode surface to enhance magnesium metal deposition.[110] However, as the Grignard reagent is very unstable under atmospheric conditions, there is a danger of ignition and explosion and there are safety issues with this system.

Recently, it was reported that reversible magnesium metal deposition/dissolution reactions can occur in some electrolytes consisting of inorganic salts and organic solvents.[111-113] Among these electrolytes, magnesium bis(trifluolomethanesulfonyl)amide ($Mg(TFSA)_2$)/triethylene glycol dimethyl ether (triglyme) had high anodic stability, providing a magnesium rechargeable battery with high energy density, without corrosion and safety problems. Doe *et al.* reported that an electrolyte prepared by dissolving magnesium chloride ($MgCl_2$) and aluminum chloride ($AlCl_3$) in 1,2-Dimethoxyethane (glyme) undergoes magnesium metal deposition/dissolution reactions with an oxidation potential limit of 3.1 V (vs. Mg^{2+}/Mg).[114] This electrolyte uses a Lewis acid ($MgCl_2$)–Lewis base ($AlCl_3$) reaction. In addition, it was reported that the precipitate formed was similar to the precipitate electrodeposited from the Grignard reagent based electrolyte, and the presence of Mg was confirmed using EDX analysis, but Al and Cl were also observed. Mohtadi *et al.* reported that magnesium borohydride ($Mg(BH_4)_2$) dissolved in glyme and THF undergoes magnesium metal deposition/dissolution reactions, with better electrochemical characteristics observed when glyme is used as the solvent (Figure 1-8).[112] Furthermore, it has been reported that the addition of lithium borohydride ($LiBH_4$) to $Mg(BH_4)_2$/glyme results in a higher current density than $Mg(BH_4)_2$/glyme alone. Infrared spectroscopy (IR) and NMR measurements of the $Mg(BH_4)_2$ electrolyte revealed the presence of a dissolved $[Mg\{(\mu\text{-}H)_2BH_2\}]_2$ species, which is an ion pair.[112] Shao *et al.* reported that magnesium metal deposition/dissolution reactions were possible in $Mg(BH_4)_2$/diglyme, and that the coulombic efficiency became 100% when 1.5 M of $LiBH_4$ was added, with a conductivity of 3.27 mS cm^{-1}.[111] These results are similar to the characteristics of a lithium ion rechargeable battery electrolyte. The solvation structure was estimated using ^1H-NMR and ^{11}B-NMR measurements, and the magnesium metal deposition/dissolution reactions were reported to be influenced by the coordination environment around magnesium. Ha *et al.* reported magnesium metal deposition/dissolution reactions in an electrolyte of $Mg(TFSA)_2$ dissolved in an equivolume mixture of glyme and diglyme.[113] It has also been reported that magnesium metal deposition/dissolution reaction occur in an electrolyte of $Mg(TFSA)_2$ dissolved in triglyme.[115,116] When glyme is used as a solvent, the electrochemical stability is affected by changing the anion, probably because the ionic liquid to which the lithium salt is added determines the ionic conduction behavior of the anion. Furthermore, it is clear that the solvation structure is affected by the chain length of glyme and the kind of anion.[117] These findings can be considered as important design guidelines for magnesium rechargeable battery electrolytes, as the solvation structure determines whether desolvation occurs during magnesium metal deposition and dissolution in the electrolyte.[118,119]

It has been reported that the ion pair between magnesium ions and bis (trifuluoromethanesulfonyl) amide (TFSA) anion undergoes partial reduction of the magnesium cation (Mg^{2+} to Mg^{+}) at the magnesium metal potential, which can cause the TFSA anion decomposition reaction to compete with magnesium metal deposition reaction .[120] An ionic liquid is essentially a liquid composed only of ions (cations and anions) with excellent characteristics such as nonvolatility, nonflammability, wide electrochemical potential, and high conductivity.[121,122] Thus, ionic liquids would be very attractive for novel magnesium rechargeable battery electrolytes, if electrolytes capable of magnesium metal deposition and dissolution were found. Vardar *et al*. carried out magnesium metal electrodeposition experiments with electrolytes of ionic liquid and magnesium inorganic salts. In the electrolyte of $Mg(BH_4)_2$ dissolved in N,N-diethyl-N-methyl-N-(methoxyethyl)ammonium tetrafluoroborate (DEME-BF_4), peaks were obtained at the cathode and the anode. However, about 1.0 V (vs. Mg^{2+}/Mg) oxidizes BH_4^- which is an anion, and when it is less than about -1.5 V (vs. Mg^{2+}/Mg), the reductive decomposition of DEME-BF_4 takes place and magnesium metal deposition reaction. It was reported that we could not confirm.[123] In addition, Yoshimoto *et al*. attempted magnesium metal electrodeposition in a mixed system of DEMETFSA, which has an aliphatic ammonium group, and LiTFSA. Ammonium cations in this system are known to be resistant to reduction, and it is believed that cathode decomposition does not occur at the magnesium metal electrodeposition potential. Further, it has been reported that magnesium metal deposition/dissolution reactions are impossible with Mg(TFSA)$_2$ alone because the magnesium salt is in an associated state when dissolved in the ionic liquid; as little dissociation occurs, there is almost no free magnesium ions. However, it has been reported that magnesium metal deposition/dissolution reactions are possible through codeposition of magnesium and lithium by adding LiTFSA. Magnesium metal deposition/dissolution reactions have also been reported in an electrolyte obtained by combining Grignard reagents and ionic liquids. However, the coulombic efficiencies of the magnesium deposition/dissolution reactions in these electrolytes were still not sufficient, and further development is needed.

Another method of solving the above problems is to use a magnesium alloy instead of magnesium metal as the anode. Although the theoretical capacities of magnesium alloys are smaller than that of magnesium metal, electrolytes that are not suitable for magnesium metal can be used because the redox potentials of alloys are higher than that of the metal. It has been reported that magnesium alloys with bismuth (Bi), antimony (Sb), tin (Sn), lead (Pb), and indium (In) can be used as negative electrodes.[124-130] Among these alloys, bismuth is an attractive negative electrode because of its theoretical volumetric capacity (1949 mAh $cm^{-3}{}_{Mg3Bi2}$), which is comparable to that of lithium metal (2062 mAh cm^{-3}). Magnesium ion insertion into the bismuth electrode occurs in a $Mg(TFSA)_2$/AN electrolyte, but the magnesium metal deposition reaction does not occur because of decomposition of the electrolyte on the negative electrode.[132] Converting bismuth electrodes into nanotubes improves the cycling stability relative to a micro bismuth electrode because the bismuth nanotube electrode retains a pristine structure after the 1st discharge. Further, the overpotential of the magnesium ion insertion/extraction reaction with the nanotube electrode is smaller than that with the micro electrode. Murgia *et al.* used *operando* X-ray diffraction (XRD) measurements to reveal that bismuth negative electrodes react without forming intermediates or amorphous structures.[131] When the electrodeposited alloy between bismuth and antimony is used, the cycling stability is better than that of the bismuth electrode. However, this reaction mechanism has not been studied in detail.

The tin electrode has a high capacity (903 mAh g^{-1}) at a row late, and the reaction voltage is lower than that of the bismuth electrode. Further, using X-ray photoelectron spectroscopy (XPS) analysis, Nguyen *et al.* showed that the surface of the electrode after electrochemical measurements is composed of mixtures of various inorganic salts of tin and magnesium between tin and PhMgCl.[132] The surface of the tin electrode was formed by decomposition of THF. In the case of a β-SnSb nanoparticle electrode, magnesium ions gradually react and enter the β-SnSb particles, and then the whole particles become alloys of magnesium and β-SnSb. Next, the alloy between magnesium and β-SnSb undergoes lattice expansion and forms cracks. Then, Sb-rich grains and magnesiated Sn nanoparticles were formed. During the demagnesiation reaction, magnesium ions are extracted from the Sn particles, but about 60% remains trapped in alloys with Sn and Sb grains.[127]

Murgia *et al.* reported that an alloying reaction occurs between indium and magnesium. Further, the electrochemical mechanism was confirmed by *operando* X-ray diffraction measurements to involve a biphasic transition reaction without an intermediate amorphization process.[133] Alloying reaction has also been reported to occur between lead and magnesium, but the reaction mechanism has not been clarified. Similar to the magnesium metal deposition reaction, the interfacial reaction between the electrolyte and the negative electrode should be important in magnesium alloying reactions. However, the reaction mechanism at the interface is not yet clearly understood. There are only a few examples of magnesium secondary battery negative reaction mechanisms that have been elucidated experimentally, and the factors that control magnesium metal deposition/dissolution reactions are not clear. By determining these factors, it will be possible to obtain optimum design guidelines for magnesium rechargeable battery electrolytes, which is important for realizing further high capacity magnesium rechargeable battery systems.

1.5. Objective

This research was aimed at developing material design guidelines for anodes and electrolytes in anticipation of practical application of magnesium rechargeable batteries. For this purpose, we attempted to elucidate the reaction mechanism at the anode/electrolyte interface by directly observing magnesium ions during battery operation using *operando* soft X-ray absorption spectroscopy and analyzing the electrons and local structures of magnesium ions.

1.6. Outline of the Present Thesis

In the present thesis consisting of six chapters, we elucidate the mechanisms at the anode or at the interface between the anode and the electrolyte using *operando* soft X-ray absorption spectroscopy.

In chapter 1 (this chapter), the developments in post-lithium ion rechargeable batteries towards higher energy densities, improvement of safety, etc. are summarized to show that magnesium rechargeable batteries are promising candidates. Furthermore, the present state of research on magnesium rechargeable batteries is presented, as well as new electrolytes for realizing the high potentials required for such batteries.

In chapter 2, to understand the mechanism by which magnesium metal deposition/dissolution reactions occur in ether-based electrolytes, we investigated the coordination structure of magnesium ions in the bulk and at the anode surface in three electrolytes. Subsequently, we investigated the electronic and local structures of magnesium ions near the negative electrode surface in each electrolyte under an applied potential via the *operando* X-ray absorption spectroscopy technique, and discussed the relationship between the coordination structure of magnesium ions and the magnesium metal deposition/dissolution reactions.

In chapter 3, to understand the reaction mechanism at the interface between electrolytes and bismuth electrodes, we investigated the coordination structure of magnesium ions at the bismuth electrode surface in two electrolytes. We investigated the electronic and local structures of magnesium ions near the negative electrode surface in each electrolyte during the magnesium insertion process using *operando* soft X-ray absorption spectroscopy and discussed the relationship between the coordination structure of magnesium ions and the magnesium insertion reaction.

In chapter 4, the reaction mechanism of magnesium metal deposition reaction of BH_4 anion based electrolytes was investigated. The different of the coordination structure between magnesium ions and BH_4 anions is investigated by Raman spectroscopy. The electronic structure and local structure at negative electrode/electrolyte interface are investigated by *operando* soft X-ray absorption spectroscopy.

In chapter 5, the effects of electrolyte additives on the interfacial structure between the anode and the electrolyte are investigated. The electronic structures of the anode and the electrolyte containing additives are investigated by Raman spectroscopy and *operando* soft X-ray absorption spectroscopy.

In chapter 6, conclusions obtained from the present studies and prospects for future magnesium rechargeable batteries are presented.

References

(1) Goodenough, J. B.; Park, K. –S. *J. Am. Chem. Soc.* **2013**, 135, 1167.

(2) Armand, M.; Tarascon, J. M. *Nature* **2008**, 451, 652.

(3) Dunn, B.; Kamath, H.; Tarascon, J. M. *Science* **2011**, 334, 928.

(4) Whittingham, M. S. *J. Electrochem. Soc.* **1976**, 123, 315.

(5) Whittingham, M. S. *Science* **1976**, 192, 1126.

(6) Ohzuku, T.; R. J. Brodd, R. J. *J. Power Sources* **2007**, 174, 449.

(7) Lazzari, M.; Scrosati, B. *J. Electrochem. Soc.* **1980**, 127, 773.

(8) Mizushima, K.; Jones, P. C.; Wiseman, P. J.; Goodenough, J. B. *Mat. Res. Bull.* **1980**, 15, 783.

(9) Yazami, R.; P. Touzain, P. *J. Power Sources* **1983**, 9, 365.

(10) Auborn, J. J.; Barberio, Y. L. *J. Electrochem. Soc.* **1987**, 137, 638.

(11) Yoshino, A.; Sanechika, K.; Nakajima, T. Japanese Patent 1989293, **1985**.

(12) Van Noorden, R. *Nature* **2014**, 507, 26.

(13) Ng, S. –H.; La Mantia, F.; Novák, P. *Angew Chem., Int. Ed.* **2009**, 48, 528.

(14) Liu, J.; Kunz, M.; Chen, K.; Tamura, N.; Richardson, T. J. *J. Phys. Chem. Lett.* **2010**, 1, 2120.

(15) Nanda, J.; Remillard, J.; O'Neill, A.; Bernardi, D.; Ro, T.; Nietering, K. E.; Go, J. –Y.; Miller, T. J. *Adv. Funct. Mater.* 2011, **21**, 3282.

(16) Ouvrard, G.; Zerrouki, M.; Soudan, P.; Lestriez, B.; Masquelier, C.; Morcrette, M.; Hamelet, S.; Belin, S.; Flank, A. M.; Baudelet, F. *J. Power Sources* **2013**, 229, 16.

(17) Koksbang, R.; Barker, J.; Shi, H.; Saidi, M. Y. *Solid State Ionics* **1996**, 84, 1.

(18) Gong, Z.; Yang, Y. *Energy Environ. Sci.* **2011**, 4, 3223.

(19) Rousse, G.; and Tarascon, J. M. *Chem. Mater.* **2014**, 26, 394.

(20) Reimers, J. N.; Dahn, J. R. *J. Electrochem. Soc.* **1992**, 139, 2091.

(21) Padhi, A. K.; Nanjundaswamy, K. S.; Goodenough, J. B. *J. Electrochem. Soc.* **1997**, 144, 1188.

(22) Meethong, N.; Huang, H. Y. –S.; Carter, W. C.; Chiang, Y. –M. *Electrochem. Solid-State Lett.* **2007**, 10, A134.

(23) Malik, R.; Burch, D.; Bazant, M.; Ceder, G. *Nano Lett.* **2010**, 10, 4123.

(24) Orikasa, Y.; Maeda, T.; Koyama, Y.; Murayama, H.; Fukuda, K.; Tanida, H.; Arai, H.; Matsubara, E.; Uchimoto, Y.; Ogumi, Z. *J. Am. Chem. Soc.* **2013**, 135, 5497.

(25) Ogumi, Z. *Electrochemistry* **2010**, 78, 319.

(26) Xu, K.; Von Cresce, A. *J. Mater. Chem.* **2011**, 21, 9849.

(27) Ohzuku, T.; Makimura, Y. *Chem. Lett.* **2001**, 30, 744.

(28) Reimers, J. N.; Dahn, J. R. *J Electrochem Soc*, **1992**, 139, 2091.

(29) Thackeray, M. M.; David, W. I. F.; Bruce, P. G.; Goodenough, J. B. *Mater. Res. Bull.* **1983**, 18, 461.

(30) Thackeray, M. M.; Johnson, P. J.; Depicciotto, L. A.; Bruce, P. G.; Goodenough, J. B. *Mater Res Bull.* **1984**, 19, 179.

(31) Berg, H.; Kelder, E. M.; Thomas, J. O. *J. Mater. Chem.* **1998**, 9, 427.

(32) Ohzuku, T.; Sawai, K.; Hirai, T. *J Electrochem Soc*, **1990**, 137, 3004.

(33) Gummow, R. J.; A. Dekock, A.; Thackeray, M. M. *Solid State Ionics* **1994**, 69, 59.

(34) Li, G. H.; Ikuta, H.; Uchida, T.; Wakihara, M. *J. Electrochem. Soc*. **1996**, 143, 178.

(35) Ellis, B. L.; Lee, K. T.; Nazar, L. F. *Chem. Mater.* **2010**, 22, 691.

(36) Morgan, D.; Van der Ven, A.; Ceder, G. *Electrochem. Solid-State Lett.* **2004**, 7, A30.

(37) Islam, M. S.; Driscoll, D. J.; Fisher, C. A. J.; Slater, P. R. *Chem. Mater*. **2005**, 17, 5085.

(38) Huang, H.; Yin, S. C.; Nazar, L. F. *Electrochem. Solid-State Lett.* **2001**, 4, A170.

(39) Klett, M.; Giesecke, M.; Nyman, A.; Hallberg, F.; Lindstrom, R. W.; Lindbergh, G.; Furo, I. *J Am. Chem. Soc*. **2012**, 134, 14654.

(40) Iwamoto, K.; Aotani, N.; Takada, K.; Kondo, S. *Solid State Ionics* **1995**, 79, 288.

(41) Hayashi, A.; Komiya, R.; Tatsumisago, M.; Minami, T. *Solid State*

Ionics **2002**, 152, 285.

(42) Takada, K.; Inada, T.; Kajiyama, A.; Sasaki, H.; Kondo, S.; Watanabe, M.; Murayama, M.; Kanno, R. *Solid State Ionics* **2003**, 158, 269.

(43) Idota, Y.; Kubota, T.; Matsufuji, A.; Maekawa, Y.; Miyasaka, T. *Science* **1997**, 276, 1395.

(44) Prosini, P. P.; Zane, D.; Pasquali, M. *Electrochim. Acta* **2001**, 46, 3517.

(45) Wright, P. V. *Br. Polym. J*, **1975**, 7, 319.

(46) Girishkumar, G.; G.; McCloskey, B.; Luntz, A. C.; Swanson, S.; Wilcke, W. *J Phys Chem. Lett.* **2010**, 1, 2193.

(47) Zu, C. X.; Li, H. *Energy Environ. Sci.* **2011,** 4, 2614.

(48) Girishkumar, G.; McCloskey, B.; Luntz, A. C.; Swanson, S.; Wilcke, W. *J Phys Chem. Lett.* **2010,** 1, 2193.

(49) Hayashi, M.; Arai, H.; Ohtsuka, H.; Sakurai, Y. *J. Power Sources* **2003**, 119, 617.

(50) Hayashi, M.; Arai, H.; Ohtsuka, H.; Sakurai, Y. *Electrochem. Solid-State Lett*. **2004**, **7**, A119.

(51) Aurbach, D.; Skaletsky, R.; Gofer, Y. *J. Electrochem. Soc*. **1991**, 138, 3536.

(52) Amatucci, G. G.; Badway, F.; Singhal, A.; Beaudoin, B.; Skandan, G.; Bowmer, T.; Plitz, I.; Pereira, N.; Chapman, T.; Jaworski, R. *J. Electrochem. Soc*. **2001**, 148, A940.

(53) Le, D. B.; Passerini, S.; Coustier, F.; Guo, J.; Soderstrom, T.; Owens, B. B.; Smyrl, W. H. *Chem. Mater*. **1998**, 10, 682.

(54) Bruce, P. G.; Krok, F.; Lightfoot, P.; Nowinski, J. L. *Solid State Ionics* **1992**, 53, 351.

(55) Balasubramanian, R.; Veluchamy, A.; Venkatakrishnan, N. *J. Power Sources*. **1994**, 52, 305.

(56) Brenner, A. *J. Electrochem. Soc.* **1996**, 143, 3133.

(57) Spahr, M. E.; Novák, P.; Haas, O.; Nesper, R. *J. Power Sources* **1995**, 54, 346.

(58) Koksbang, R.; West, K. *Solid State Ionics* **1988**, 28, 868.

(59) Pereira-Ramos, J. P.; Messina, R.; Perichon, J. *J. Electroanal. Chem.* **1987**, 218, 241.

(60) Besenhard, J. O.; Winter, M. *ChemPhysChem.* **2002**, **3**, 155.

(61) Gregory, T. D.; Hoffman, R. J.; Winterton, R. C. *J. Electrochem. Soc.* **1990**, 137, 775.

(62) Novak, P.; Shklover, V.; Nesper, R. *Zeitschrift Fur Physikalische Chemie-International Journal of Research in Physical Chemistry & Chemical Physics* **1994**, 185, 51.

(63) Novak, P.; Scheifele, W.; Joho, F.; and O. Haas *J. Electrochem. Soc.* **1995**, 142, 2544.

(64) Novak, P.; Scheifele, W.; Haas, O. *J. Power Sources* **1995**, 54, 479.

(65) Novak, P.; Imhof, R.; Haas, O. *Electrochim. Acta* **1999**, 45, 351.

(66) Novak, P.; Desilvestro, J. *J. Electrochem. Soc.* **1993**, 140, 140.

(67) Yamamoto, T.; Kikkawa, S.; Koizumu, M. *J. Electrochem. Soc.* **1984**, 131, 1343.

(68) Whittingham, M. S. *Prog. Solid State Chem.* **1978**, 12, 41.

(69) Bruce, P. G.; Krok, F.; Lightfoot, P.; Nowinski, J. L.; Gibson, V. C. *Solid State Ionics* **1992**, 53, 351.

(70) Li, X. L.; Li, Y. D. *J. Phys. Chem. B* **2004**, 108, 13893.

(71) Tao, Z. L.; Xu, L. N.; Gou, X. L.; Chen, J.; Yuan, H. T. *Chem. Commun.* **2004**, 18, 2080.

(72) Aurbach, D.; Lu, Z.; Schechter, A.; Gofer, Y.; Gizbar, H.; Turgeman, R.; Cohen, Y.; Moshkovich, M.; Levi, E. *Nature* **2000**, 407, 724.

(73) Chevrel, R.; Sergent,, M.; Prigent, J. *Mater. Res. Bull.* **1974**, 9, 1487.

(74) Pereiraramos, J. P.; Messina, R.; Perichon, J. *J. Electroanal. Chem.* **1987**, 218, 241.

(75) Levi, E.; Gofer, Y.; Aurbach, D. *Chem. Mater.* 2010, **22**, 860.

(76) Imamura, D.; Miyayama, M.; Hibino, M.; Kudo, T. *J. Electrochem. Soc.* **2003**, 150, A753.

(77) Hibino, M.; Ugaji, M.; Kishimoto, A.; Kudo, T. *Solid State Ionics* **1995**, 79, 239.

(78) Imamura, D.; Miyayama, M. *Solid State Ionics* **2003**, 161, 173.

(79) Aurbach, D.; Gofer, Y.; Schechter, A.; Chusid, O.; Gizbar, H.; Cohen, Y.; Moshkovich, M.; Turgeman, R. *J. Power Sources* **2001**, 97, 269.

(80) Zhang, R. G.; Yu, X. Q.; Nam, K. W.; Ling, C.; Arthur, T. S.; Song, W.; Knapp, A. M.; Ehrlich, S. N.; Yang, X. Q.; Matsui, M. *Electrochem. Commun.* **2012**, 23, 110.

(81) Arthur, T. S.; Zhang, R. G.; Ling, C.; Glans, P. A.; Fan, X. D.; Guo, J. H.; Mizuno, F. *ACS Appl. Mater. Interfaces* **2014**, 6, 7004.

(82) Liang, Y. L.; Yoo, H. D.; Li, Y. F.; Shuai, J.; Calderon, H. A.; Hernandez, F. C. R.; Grabow, L. C.; Yao, Y. *Nano Lett.* **2015**, 15, 2194.

(83) Liu, Y. C.; Jiao, L. F.; Wu, Q.; Zhao, Y. P.; Cao, K. Z.; Liu, H. Q.; Wang, Y. J.; Yuan, H. T. *Nanoscale* **2013**, 5, 9562.

(84) Liu, Y. C.; Jiao, L. F.; Wu, Q.; Du, J.; Zhao, Y. P.; Si, Y. C.; Wang, Y. J.; Yuan, H. T. *J. Mater. Chem. A* **2013**, 1, 5822.

(85) Yang, S. Q.; Li, D. X.; Zhang, T. R.; Tao, Z. L.; J. Chen, J. *J. Phys. Chem. C* **2012**, 116, 1307.

(86) Liang, Y. L.; Feng, R. J.; Yang, S. Q.; Ma, H.; Liang, J.; Chen, J. *Adv. Mater.* **2011**, 23, 640.

(87) Thackeray, M. M.; Dekock A. *Solid State. Chem.* **1988**, 74, 414.

(88) Thackeray, M. M.; Depicciotto, L. A.; Dekock, A.; Johnson, P. J.; Nicholas, V. A.; Adendorff, K. T. *J. Power Sources* **1987**, 21, 1.

(89) Rong, Z.; Malik, R.; Canepa, P.; Gautam, G. S.; Liu, M.; Jain, A.; Persson, K.; Ceder, G. *Chem. Mater.* **2015**, 27, 6016.

(90) Sanchez, L.; PereiraRamos, P. *J. Mater. Chem.* **1997**, 7, 471.

(91) Yuan, C. L.; Zhang, Y.; Pan, Y.; Liu, X. W.; Wang, G. L.; Cao, D. X.

Electrochim. Acta **2014**, 116, 404.

(92) Kim, C.; Phillips, P. J.; Key, B; Yi, T.; Nordlund, D.; Yu, Y. –S.; Bayliss, R. D.; Han, S. –D.; He, M.; Zhang, Z.; Burrell, A. K.; Klie, R. F.; Cabana, J. *Adv. Mater.* **2015**, 27, 3377.

(93) Okamoto, S.; Ichitsubo, T.; Kawaguchi, T.; Kumagai, Y.; Oba, F.; Yagi, S.; Shimokawa, K.; Goto, N.; Doi, T.; E. Matsubara, E. *Adv. Sci.* **2015**, 2, 1500072.

(94) Yamada, A.; Chung, S. C.; Hinokuma, K. *J. Electrochem. Soc.* **2001**, 148, A224.

(95) Melot, B. C.; Tarascon, J. M. *Accounts of Chemical Research* **2013**, 46, 1226.

(96) Makino, K.; Katayama, Y.; Miura, T.; Kishi, T. *J. Power Sources* **2001**, 99, 66.

(97) Ling, C.; Banerjee, D.; Song, W.; Zhang, M. J.; Matsui, M. *J. Mater. Chem.* **2012**, 22, 13517.

(98) Overcash, D. M.; Mathers, F. C. *Trans. Electrochem.Soc.* **1993**, 64, 305.

(99) Connor, J. H.; Reid, W. E.; Wood, G. B. *J. Electrochem. Soc.* **1957**, 4, 38.

(100) Lu, Z.; Schechter, A.; Moshkovich, M.; Aurbach, D. *J. Electroanal. Chem.* **1999**, 466, 203.

(101) Liebenow, C.; Yang, Z.; Lobitz, P. *Electrochem. Commun.* **2000**, 2, 641.

(102) Gregory, T. D.; Hoffman, R. J.; Winterton, R. C. *J. Electrochem. Soc.* **1990**, 137, 775.

(103) Lu, Z.; Schechter, A.; Moshkovich, M.; Aurbach, D. *J. Electroanal. Chem.* **1999**, 466, 203.

(104) Covington, A. D.; Covington, A. K. *J. Chem. Soc., Faraday Trans. 1* **1975**, 71, 831.

(105) Aurbach, D.; Turgeman, R.; Chusid, O.; Gofer, Y. *Electrochem. Commun.* **2001**, 3, 252.

(106) Aurbach, D.; Gizbar, H.; Schechter, A.; Chusid, O.; Gottlieb, H. E.; Gofer, Y.; Goldberg, I. *J. Electrochem. Soc*. **2002**, 149, A115.

(107) Gizbar, H.; Vestfrid, Y.; Chusid, O.; Gofer, Y.; Gottlieb, H. E.; Marks, V.; Aurbach, D. *Organometallics.* **2004**, 23, 3826.

(108) Nakayama, Y.; Kudo, Y.; Oki, H.; Yamamoto, K.; Kitajima, Y.; Noda, K. *J. Electrochem. Soc.* **2008**, 155, A754.

(109) Vestfried, Y.; Chusid, O.; Goffer, Y.; Aped, P.; Aurbach, D. *Organometallics.* **2007**, 26, 3130.

(110) Mizrahi, O.; Amir, N.; Pollak, E.; Chusid, O.; Marks, V.; Gottlieb, H.; Larush, L.; Zinigrad, E.; Aurbach, D. *J. Electrochem. Soc.* **2008**, 155, A103.

(111) See, K. A.; Chapman, K. W.; Zhu, L.; Wiaderek, K. M.; Borkiewicz, O. J.; Barile, C. J.; Chupas, P. J.; Gewirth, A. A. *J. Am. Chem. Soc.* **2016**, 138, 328.

(112) Shao, Y.; Liu, T.; Li, G.; Gu, M.; Nie, Z.; Engelhard, M.; Xiao, J.; Lv, D.; Wang, C.; Zhang, J.-G.; Liu, J. *Sci. Rep.* **2013**, 3, 3130.

(113) Mohtadi, R.; Matsui, M.; Arthur, T. S.; Hwang, S. –J. *Angew. Chem., Int. Ed.* **2012**, 124, 9918.

(114) Ha, S. –Y.; Lee, Y. –W.; Woo, S. W.; Koo, B.; Kim, J. –S.; Cho, J.; Lee, K. T.; Choi, N. –S. *ACS Appl. Mater. Interfaces* **2014**, 6, 4063.

(115) Doe, R. E.; Han, R.; Hwang, J.; Gmitter, A.; Shterenberg, I.; Yoo, H. D.; Pour, N.; Aurbach, D. *Chem. Commun.* **2014**, 50, 243.

(116) Orikasa, Y.; Masese, T.; Koyama, Y.; Mori, T.; Hattori, M.; Yamamoto, K.; Okado, T.; Huang, Z. –D.; Minato, T.; Tassel, C.; Kim, J.; Kobayashi, Y.; Abe, T.; Kageyama, H.; Uchimoto, Y. *Sci. Rep.* **2014**, 4, 5622.

(117) Fukutsuka, T.; Asaka, K.; Inoo, A.; Yasui, R.; Miyazaki, K.; Abe, T.; Nishio, K.; Uchimoto, Y. *Chem. Lett.* **2014**, 43, 1788.

(118) Watkins, T.; Kumar, A.; Buttry, D. A. *J. Am. Chem. Soc.* 2016, 138, 641.

(119) Henderson, W. A. *J. Phys. Chem. B* **2006**, 110, 13177.

(120) Arthur, T. S.; Glans, P. –A.; Singh, N.; Tutusaus, O.; Nie, K.; Liu, Y. –S.; Mizuno, F.; Guo, J.; Alsem, D. H.; Salmon, N. J.; Mohtadi, R. *Chem. Mater.* **2017**, 29, 7183.

(120) Rajput, N. N.; Qu, X.; Sa, N.; Burrell, A. K.; Persson, K. A. *J. Am. Chem. Soc.* **2015**, 137, 3411.

(121) Hagiwara R.; Lee, J. S. *Electrochemistry.* **2007**, 75, 23.

(122) Armand, M.; Endres, F.; MacFarlane, D. R.; Ohno, H.; B. Scrosati, B. *Nat. Mater.* **2009**, **8**, 621.

(123) Vardar, G. Sleightholme, Alice E. S.; Naruse, J.; Hiramatsu, H.; Siegel, D. J.; Monroe, C. W. *ACS. Appl. Mater. Interfaces* **2014**, 6, 18033.

(124) Arthur; T. S.; Singh, N.; Matsui, M. *Electrochem. Commun.* **2012**, 16, 103.

(125) Singh, N.; Arthur, T. S.; Ling, C.; Matsui, M.; Mizuno, F. *Chem. Commun.* **2013**, 49, 149.

(126) Shao, Y.; Gu, M.; Li, X.; Nie, Z.; Zuo, P.; Li, G.; Liu, T.; Xiao, J.; Cheng, Y.; Wang, C.; Zhang, J. –G.; Liu, J. *Nano Lett.* **2014**, 14, 255.

(127) Parent, L. R.; Cheng, Y.; Sushko, P. V.; Shao, Y.; Liu, J.; Wang, C. –M.; N. D. Browning, N. D. *Nano Lett.* **2015**, 15, 1177.

(128) Benmayaza, A.; Ramanathan, M.; Singh, N.; Mizuno, F.; Prakash, J. *J. Electrochem. Soc.* **2015**, 162, A1630.

(129) DiLeo, R. A.; Zhang, Q.; Marschilok, A. C.; Takeuchi, K. J.; Takeuchi, E. S. *ECS Electrochem. Lett.* **2015**, 4, A10.

(130) Periyapperuma, K.; Tran, T. T.; Purcell, M. I.; Obrovac, N. *Electrochim. Acta* **2015**, 165, 162.

(131) Murgia, F.; Stievano, L.; Monconduit, L.; Berthelot, R. *J. Mater. Chem. A* **2015**, 3, 16478.

(132) Nguyen, D. –T.; Tran, X. M.; Kang, J.; Song, S. –W. *ChemElectroChem* **2016**, 3, 1813.

(133) Murgia, F.; Weldekidan, E. T.; Stievano, L.; Monconduit, L.; Berthelot, R. *Electrochem. Commun.* **2015,** 60, 56.

Table 1-1. The comparison of various metal negative electrodes.

Metal	Atomic weight	Valence change	Theoretical capacity [mAhg^{-1}, mAhcm^{-3}]	Electrode potential [V vs. SHE]	Terrestrial abundance	Melting Point (°C)
Li	6.94	1	3862, 2062	-3.05	0.006	180.5
K	39.1	1	685, 587	-2.925	2.40	63.7
Na	22.99	1	1166, 1132	-2.71	2.64	97.7
Ca	40.08	2	1337, 2073	-2.866	3.39	842.0
Mg	24.31	2	2205, 3837	-2.38	1.94	650.0
Al	26.98	3	2980, 8043	-1.662	7.56	660.3

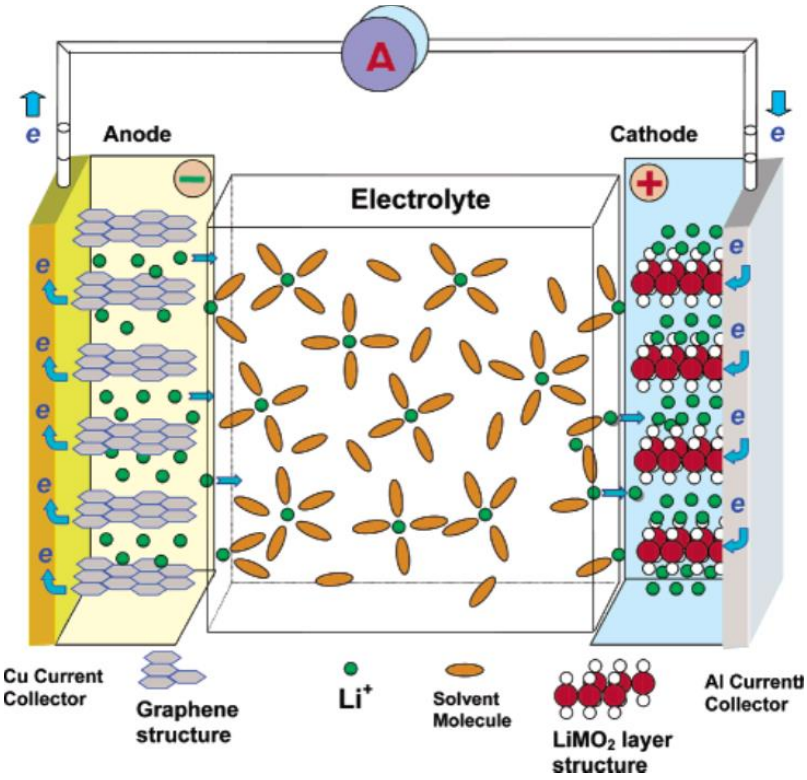

Figure 1-1. Schematic figure of lithium ion rechargeable battery[3].

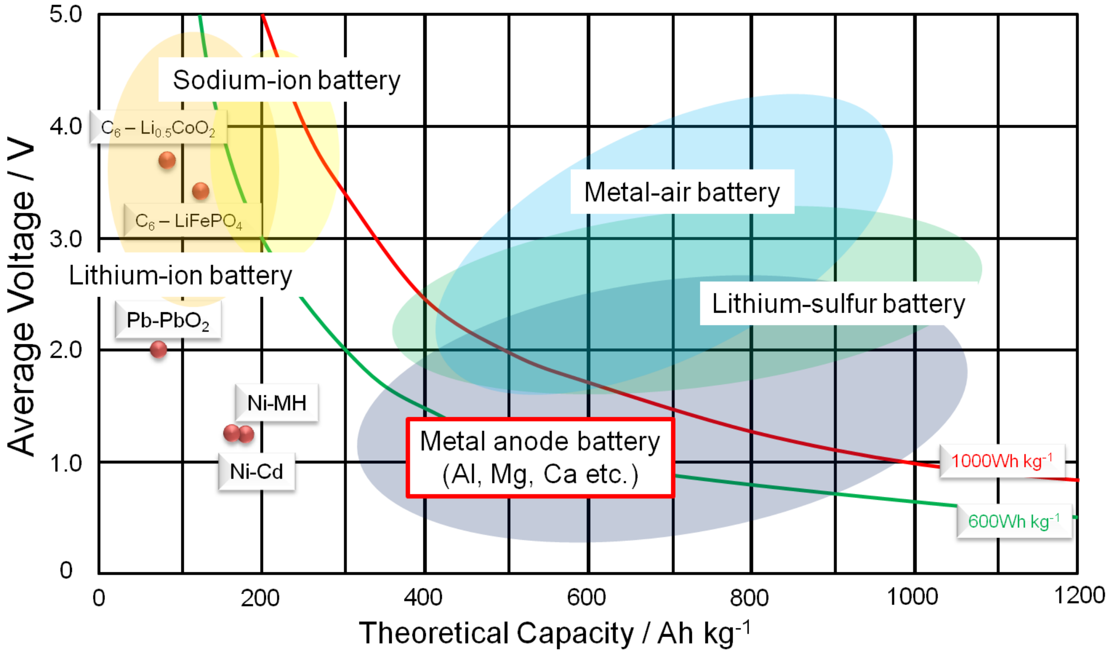

Figure 1-2. Comparison of the different battery technologies of voltage and gravimetric energy density[45].

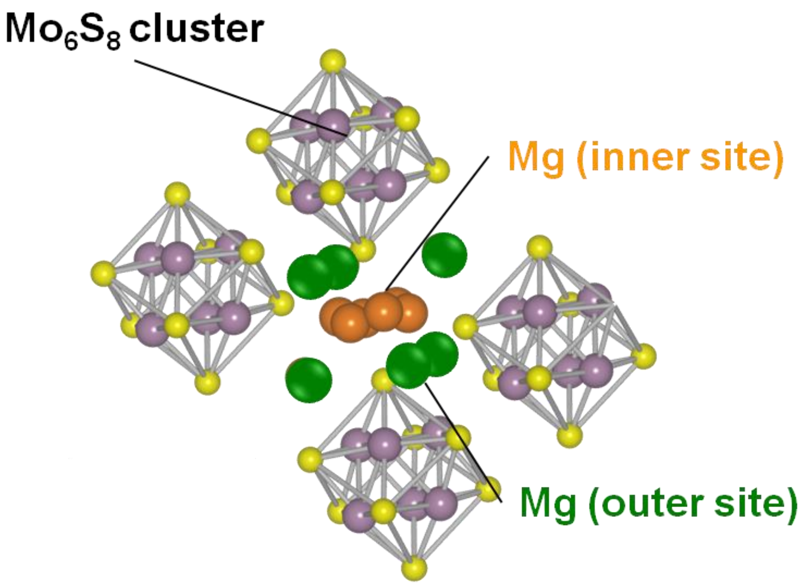

Figure 1-3. Crystal structure of the chevrel $Mg_2Mo_6S_8$ phase. Green, orange, purple, and yellow spheres are indicated Mg (outer site), Mg (inner site), Mo, and S atoms, respectively[72].

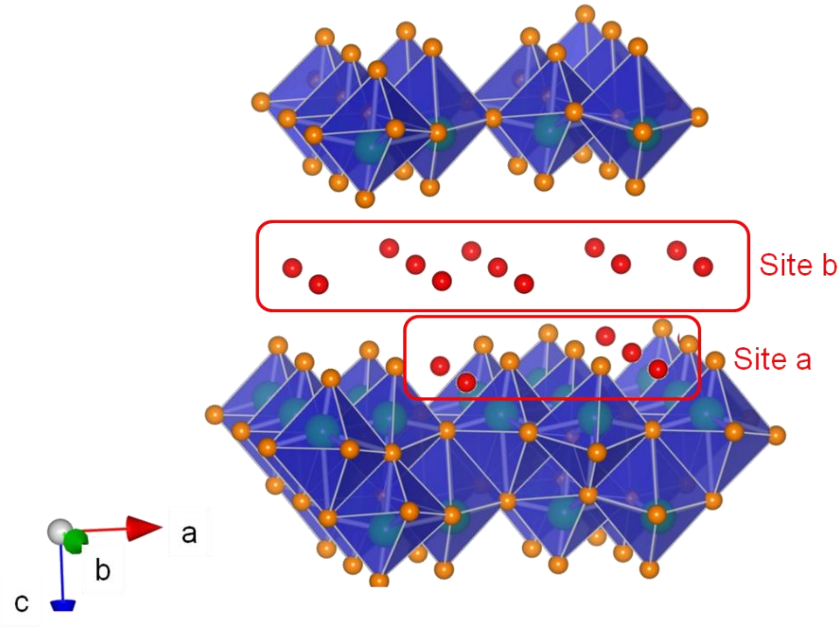

Figure 1-4. Crystal structure of the V_2O_5 aero-gel. Green, orange, and yellow spheres are indicated V, O(1), and O(2) atoms, respectively[77].

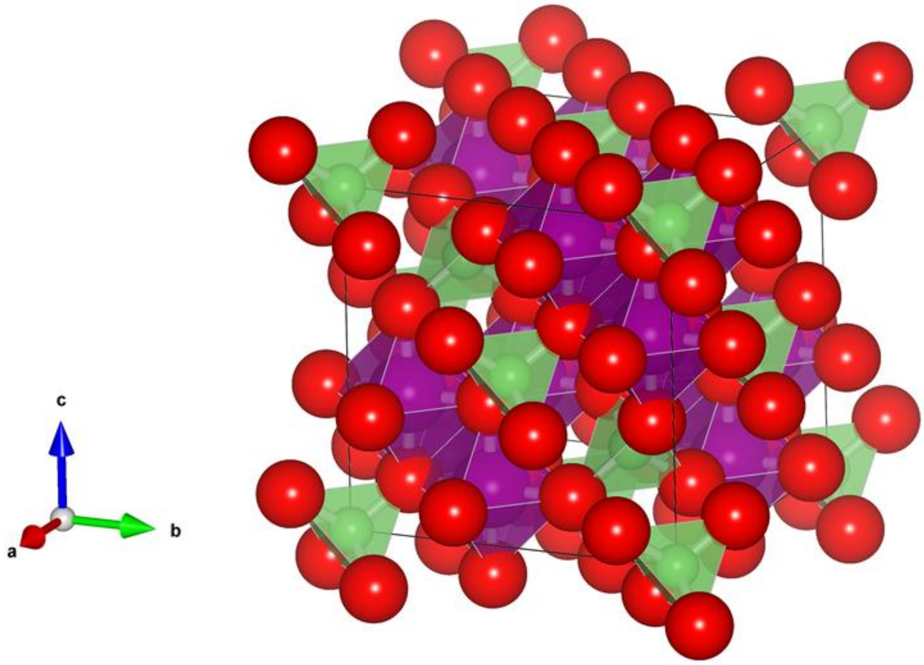

Figure 1-5. Crystal structure of the Spinel-type $LiMn_2O_4$. Green, purple and red spheres are indicated Li, Mn, and O, respectively[87].

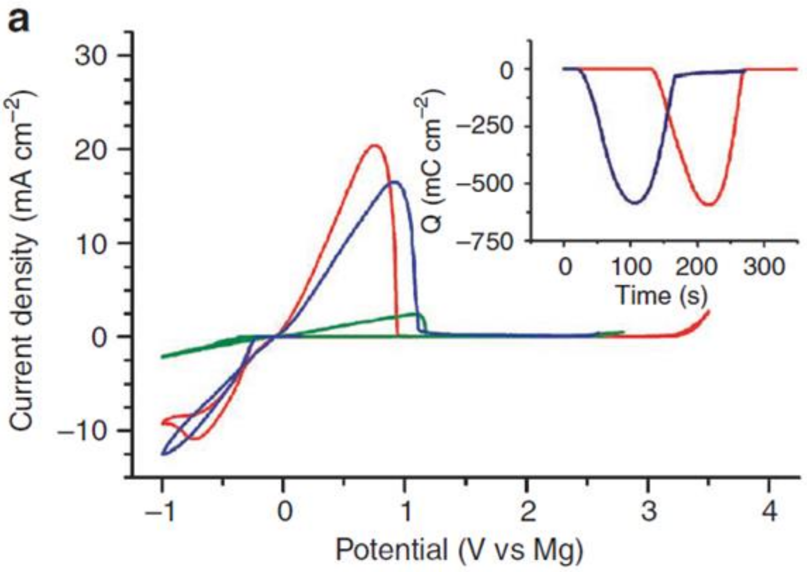

Figure 1-6. Cyclic voltammograms of 3HMDSMgCl-$AlCl_3$/THF (red line)[101].

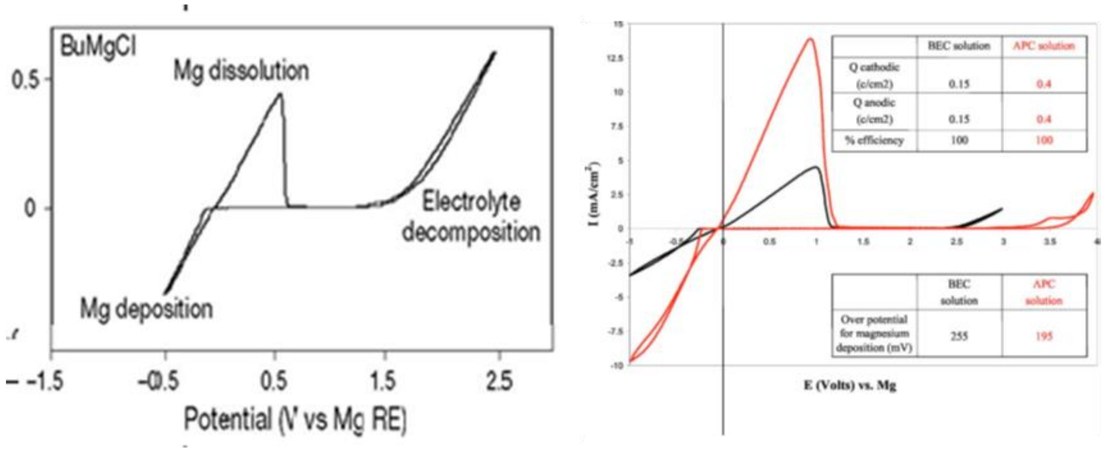

	BEC solution	APC solution
Q cathodic (c/cm2)	0.15	0.4
Q anodic (c/cm2)	0.15	0.4
% efficiency	100	100

	BEC solution	APC solution
Over potential for magnesium deposition (mV)	255	195

Figure 1-7. Cyclic Voltammograms of BuMgCl/THF(left) and $Mg(AlCl_2EtBu)_2$/THF(black line), $(PhMgCl)_2$-$AlCl_3$/THF(red line) (right)[109].

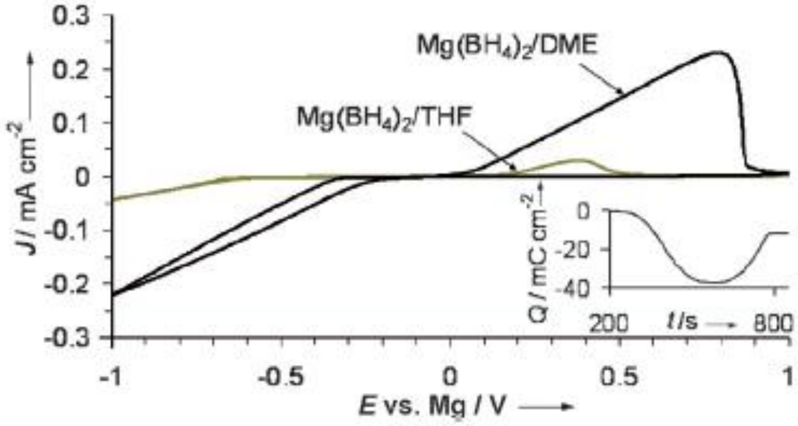

Figure 1-8. Cyclic voltammograms of Mg(BH$_4$)$_2$/glyme and Mg(BH$_4$)$_2$/THF electrolyte[113].

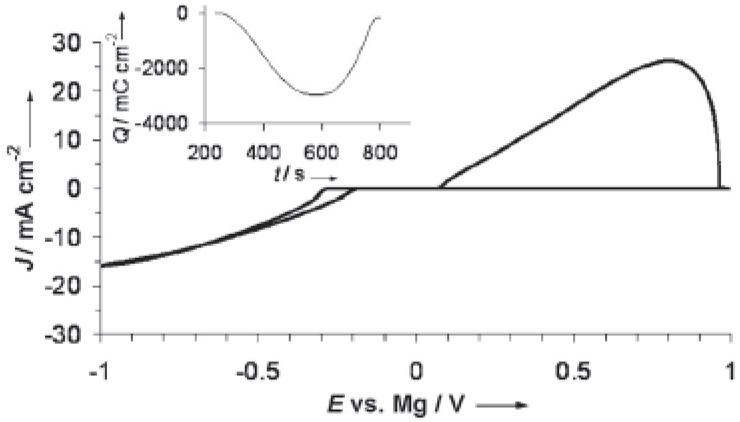

Figure 1-9. Cyclic voltammogram of LiBH$_4$/Mg(BH$_4$)$_2$ in glyme[113].

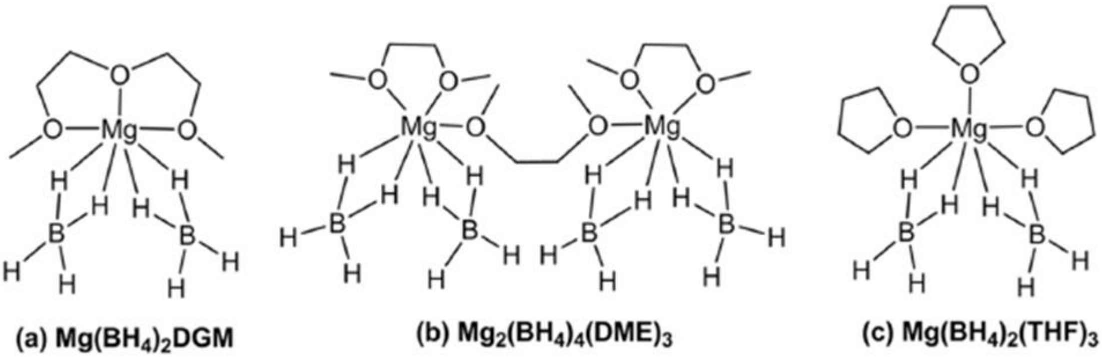

Figure 1-10. Coordination structures of $Mg(BH_4)_2$ in diglyme, glyme and THF[112].

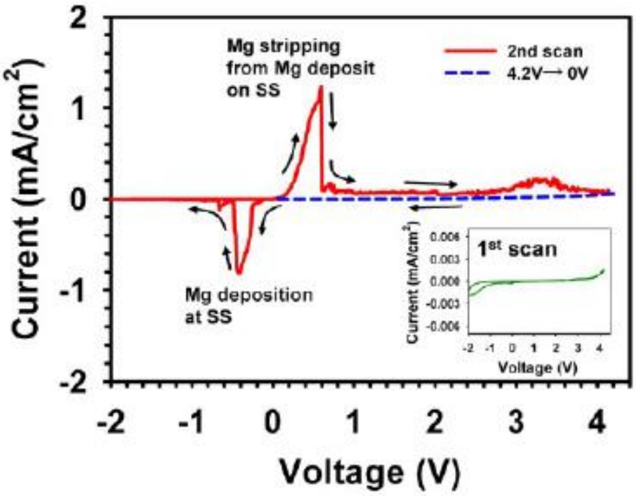

Figure 1-11. Cyclic voltammogram for 0.3 M $Mg(TFSA)_2$ in glyme / diglyme (1/1, v/v) on a SS electrode at a scan rate of 0.2 mV/s[114].

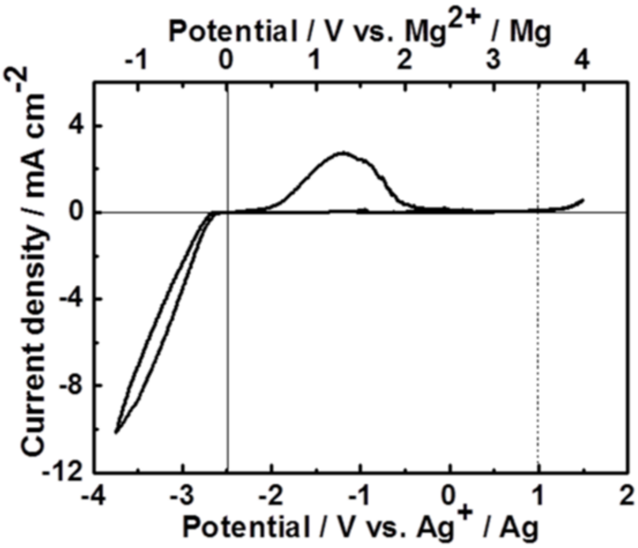

Figure 1-12. Cyclic voltammogram for 0.5 M $Mg(TFSA)_2$ in triglyme on a Pt electrode at a scan rate of 5 mV/s[116].

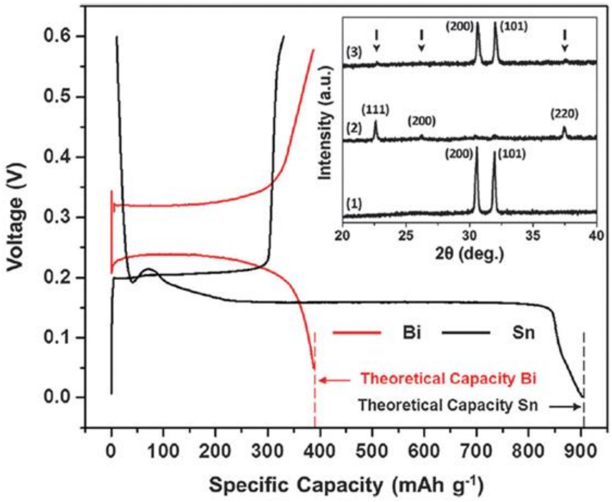

Figure 1-13. 1st cycle galvanostatic magnesiation/de-magnesiation curves for Sn/Mg (black) and Bi/Mg (red) half-cells (using organohaloaluminate electrolyte) highlighting, their achievable theoretical capacities. Inset‑XRD spectra for as-fabricated Sn, (2) magnesiated Sn (or Mg_2Sn‑peak positions marked with arrows) and (3) de-magnesiated Mg_2Sn[123].

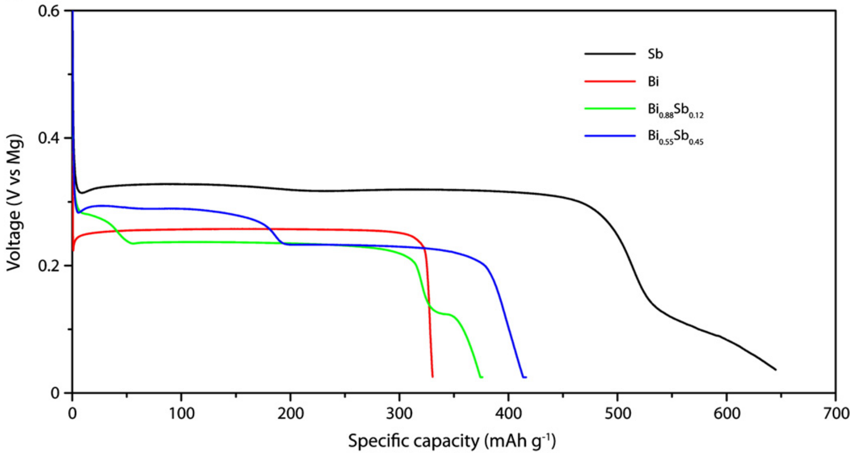

Figure 1-14. Galvanostatic discharge of Bi, Sb, $Bi_{0.88}Sb_{0.12}$, and $Bi_{0.55}Sb_{0.45}$ anodes at a 0.01 C rate[124].

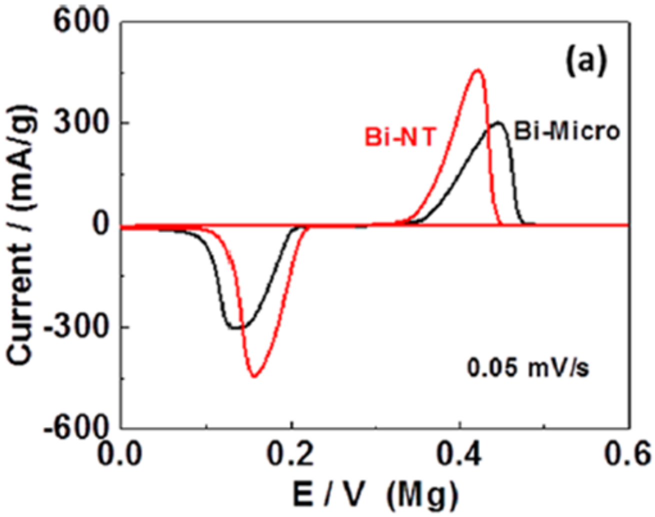

Figure 1-15. Cyclic voltammograms of Mg insertion/deinsertion in bismuth at scanning speed at 1 mV/sec[126].

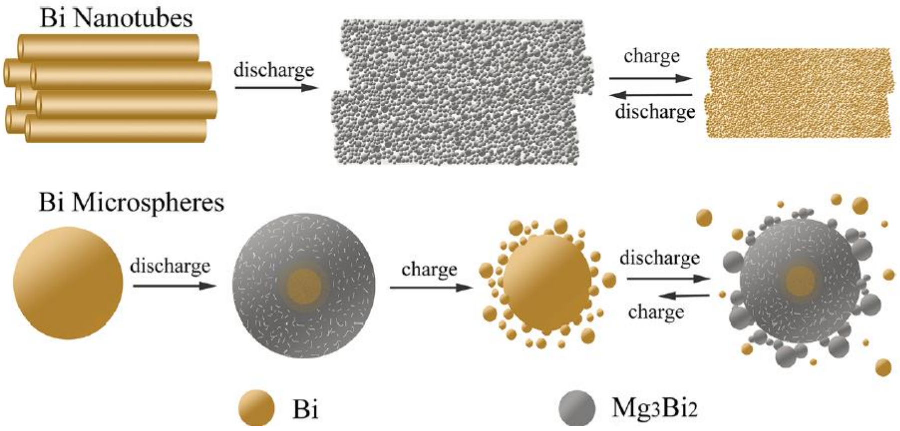

Figure 1-16. Structural transformation of bismuth during the discharge/charge process[126].

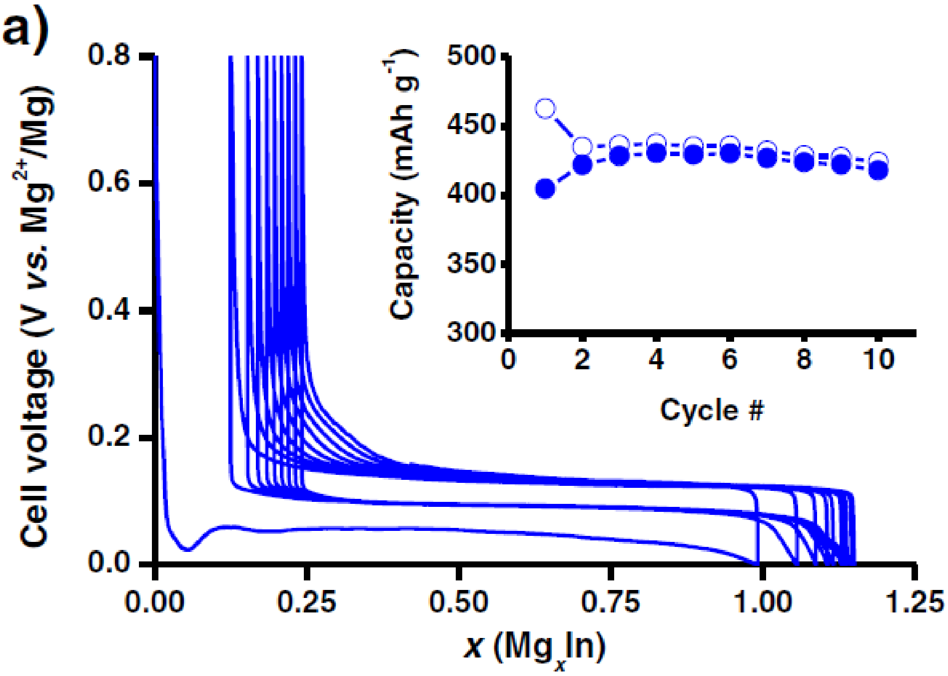

Figure 1-17. Galvanostatic cycling at C/50 and corresponding capacities evolution[132].

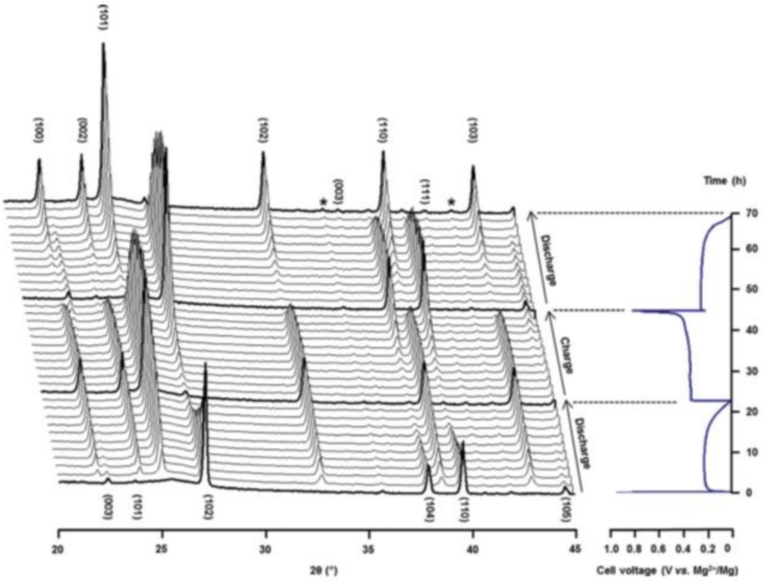

Figure 1-18. *operando* XRD characterization of the first discharge, charge and second discharge of a Bi/Mg battery[133].

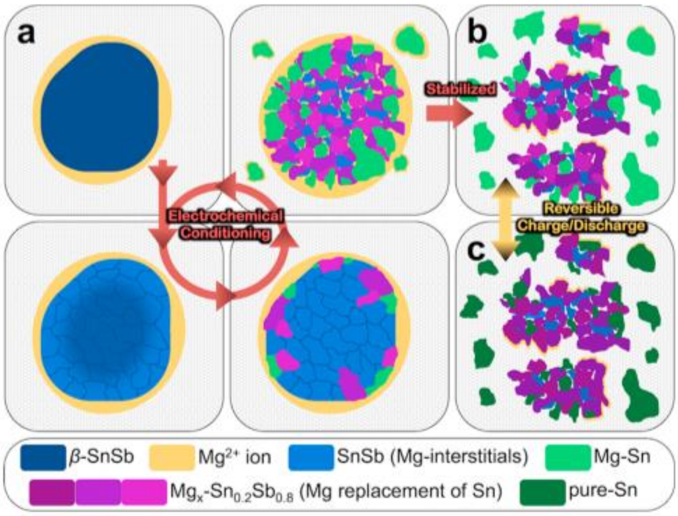

Figure 1-19. Diagram of the electrochemical Mg^{2+} insertion and extraction processes for a β-SnSb nanoparticle based on the TEM and DFT results[134].

Chapter 2: The Coordination Structure Change of Magnesium Ions at Anode/Electrolyte Interface during Magnesium Deposition Reaction

2.1 Introduction

Due to current environmental and energy issues, there is a growing need for high-performance rechargeable batteries used for applications such as renewable energy storage and electric vehicles.[1,2] Magnesium rechargeable batteries, which use magnesium metal as a negative electrode, are considered as a next-generation rechargeable battery.[3] Magnesium metal has a high theoretical volumetric capacity (3834 mAh/cm^3) and a relatively low reduction potential (-2.356 V vs. the standard hydrogen electrode), which results in a high energy density. In addition, the elemental abundance and stability of magnesium are superior to lithium,[4-6] making it to a cost-effective and safe alternative battery system.

Although the magnesium rechargeable battery has theoretical advantages, its performance is inferior to that of the lithium ion battery.[7] One major problem is that the reversible magnesium deposition/dissolution reactions do not occur in most of the conventional electrolytes that are commonly used in the lithium battery system. This is because these electrolytes are known to form a passivation layer on the surface of magnesium metal which inhibits the reversible magnesium deposition/dissolution reactions.[8] Hence, many researchers have focused on highly active magnesium organohaloaluminate-based electrolytes, which support the reversible magnesium deposition/dissolution reactions.[9-15] However, these electrolytes have some disadvantages such as their low anodic stability, corrosion, and safety, thus a breakthrough in the development of suitable electrolytes is necessary.

Recently, it was reported that the reversible magnesium deposition/dissolution reactions can occur in some electrolytes.[16-23] Among them, magnesium bis(trifluoromethanesulfonyl)amide ($Mg(TFSA)_2$)/triglyme has a high anodic stability and can provide rechargeable magnesium batteries with a high energy density, without corrosion and safety issues.[20] However, it is not clearly understood why the reversible magnesium deposition/dissolution reactions occur in $Mg(TFSA)_2$/triglyme. A clear understanding of the reaction mechanism will provide useful information to design new electrolyte materials applicable to practical magnesium rechargeable batteries.

The key factor that predominates the reaction mechanism is considered to be the coordination structures of magnesium ions in the bulk electrolyte solution and at the negative electrode surface. It is necessary to understand the differences between the coordination structures in $Mg(TFSA)_2$/triglyme and those of other electrolytes in which the magnesium deposition/dissolution reactions do not occur. Raman spectroscopy and X-ray absorption spectroscopy

(XAS) are useful techniques to clarify the coordination structures present in the electrolyte. XAS provides the electronic and local structures of a focused atom, which have then been applied to analyze the local structure of magnesium organohaloaluminate-based electrolytes.[24,25] Therefore, operando XAS is a powerful tool for analyzing the dynamic change in the local structure of magnesium ions. Indeed, the interfacial structure of a magnesium organohaloaluminate-based electrolytes during polarization can be detected with this technique.[26,27]

In this study, we examined the coordination structure of magnesium ions in the bulk solution and at the negative electrode surface for three different electrolytes: $Mg(TFSA)_2$/triglyme, $Mg(AlCl_2EtBu)_2$/tetrahydrofuran (THF), and $Mg(TFSA)_2$/2-methyltetrahydrofuran (2-MeTHF). The former two electrolytes allow (quasi-)reversible magnesium deposition/dissolution while the latter is inactive electrochemically. First, we analyzed the coordination structure of the magnesium ions in the bulk solution of each electrolyte by Raman spectroscopy. Subsequently, we examined the dynamic change in electronic and local structures of the magnesium ions near the negative electrode surface in each electrolyte with the operando XAS technique. We then discuss the relationship between the coordination structure of the magnesium ions and the magnesium deposition/dissolution reactions.

2.2 Experimental

2.2.1 Material preparation

The 0.5 M $Mg(TFSA)_2$/triglyme and 0.5 M $Mg(TFSA)_2$/2-MeTHF electrolytes were prepared by mixing $Mg(TFSA)_2$ (KISHIDA CHEMICAL Co., Ltd., 99.9%>) with triglyme (KISHIDA CHEMICAL Co., Ltd. 99%>) or 2-MeTHF (Merck, 98%>) in an Ar-filled glove box. To decrease the water content, the $Mg(TFSA)_2$ salt was dried under vacuum at 180°C for 48 h and the solvents were dried by using molecular sieves 3A for 48 h. The water content of the prepared electrolytes was less than 30 ppm, which was measured by Karl Fischer titration. 0.25 M $Mg(AlCl_2EtBu)_2$/THF was prepared according to a literature procedure.[7] 1.0 M $MgBu_2$ in heptane (Aldrich) and 1.0 M $AlCl_2Et$ in hexane (Aldrich), in a 1:2 ratio by volume were mixed for 48 h. The mixture was dried under vacuum until the solvents were evaporated. The remaining precipitate was dissolved in anhydrous THF (Al-drich, 99.9%>) to yield 0.25 M $Mg(AlCl_2EtBu)_2$/THF electrolyte.

2.2.2 Electrochemical measurements

The magnesium deposition/dissolution reactions in each electrolyte were examined with cyclic voltammetry. A three-electrode cell, which consisted of a platinum plate as a working electrode and a magnesium rod as a counter electrode, was utilized for the measurements. Different reference electrodes were used for the $Mg(TFSA)_2$/triglyme or $Mg(TFSA)_2$/2-MeTHF, and for

$Mg(AlCl_2EtBu)_2$/THF, respectively. For the $Mg(TFSA)_2$/triglyme or $Mg(TFSA)_2$/2-MeTHF electrolytes, a double-junction reference electrode equipped with microporous glass membrane was employed. The inner part contained lithium metal that was inserted into a 0.1 M solution of LiTFSA in propylene carbonate, and the outer part contained the electrolyte being analyzed. For $Mg(AlCl_2EtBu)_2$/THF, a magnesium rod was employed as the reference electrode. The cyclic voltammetry was performed at room temperature with a sweeping potential rate of 5 mV/s. The potential range was 0.2 to 4.2 V vs. Li^+/Li (corresponding to -0.76 to 3.24 V vs. Mg^{2+}/Mg) for $Mg(TFSA)_2$/triglyme or $Mg(TFSA)_2$/2-MeTHF and -1.0 to 2.2 V vs. Mg^{2+}/Mg for $Mg(AlCl_2EtBu)_2$/THF.

2.2.3 XRD measurements

X-ray diffraction (XRD) was performed with an Ultima Ⅳ (Rigaku Co., Inc.) with a CuKα X-ray source. Scanning electron microscopy (SEM) images and energy dispersive X-ray spectroscopy (EDX) spectra were collected with an S-3400 N (Hitachi HighTech Co.). After the potentiostatic deposition of the magnesium metal, the electrochemical cells were disassembled, and the obtained electrodes were washed with THF. These electrodes were then dried in an Ar-filled glove box overnight. All measurements were conducted without air exposure of the samples.

2.2.4 Raman spectroscopy

The Raman spectra of the electrolytes were measured by LabRAM HR-800(HORIBA, Ltd.) at room temperature. The wave length of the laser was 633 nm and the measured range was between 200 and 1600 cm^{-1}. To avoid air exposure, the electrolyte was put into a glass vessel and sealed in it in an Ar-filled glove box.

2.2.5 Soft X-ray absorption spectroscopy

The *operando* XAS spectra of the electrolytes, in the Mg *K*-edge region, were measured by the partial fluorescence yield method at the SPring-8 synchrotron radiation facility (BL27SU) in Hyogo, Japan. A custom-made three-electrode cell, which was previously reported,[28] was used for the *operando* XAS measurements. Ti was pre-deposited as a buffer layer onto a Si_3N_4 window with a 300 nm thickness (Norcada Inc.) by using magnetron sputtering. Then Pt was deposited as a current collector onto the Ti/Si_3N_4 window. The obtained $Pt/Ti/Si_3N_4$ window was employed as a working electrode, which passed ~76% of the incident X-rays to the electrolyte. The fluorescence X-rays that were generated from the electrolyte passed through the window with ~76% transmission to a silicon drift detector (Techno X Co., Ltd.). The *operando* cells were constructed in an Ar-filled glove box and transferred into a chamber for the XAS measurements without exposing the inside of the cells to air. *operando* XAS measurements were performed while keeping the potential of the working electrode at several values prior to magnesium deposition. Then, magnesium was deposited on the working electrode by applying a potential step method, and additional XAS measurements were performed.

2.2.6 Density functional theory (DFT) calculation

Density functional theory (DFT) calculations of free $TFSA^-$ and $Mg(TFSA)_2$ salt in triglyme solvent were carried out using Gaussian16 Revision A.03 code,[29] to investigate the coordination effect on the electronic states. Using the polarized continuum model (PCM) method with the parameters for triglyme bulk solvent (dielectric constant epsilon=7.62), we calculated the optimized geometries and the corresponding HOMO and LUMO energies of the molecular systems in the triglyme solvent. The M06 hybrid functional[30] for the exchange and correlation energy and the 6-311+G(d,p) basis set were used.

2.3 Results and Discussion

2.3.1 Behavior of magnesium metal deposition/dissolution reactions.

Figure 2-1 (a) shows the cyclic voltammograms for each electrolyte and Figure 2-1 (b) shows an enlarged figure of the current density, near the potential that magnesium deposition occurs, during potential sweeping in the negative direction (Figure 2-1 (a)). In the 0.25 M $Mg(AlCl_2EtBu)_2$/THF electrolyte, the cathodic and anodic currents attributable to magnesium deposition and dissolution, were observed as reported previously.[7] XRD and SEM-EDX confirmed the deposits obtained by the cathodic polarization to be magnesium metal (Figures 2-2 (a) and 2-3). In the 0.5 M $Mg(TFSA)_2$/triglyme, the cathodic and anodic currents, which are attributed to magnesium deposition and dissolution, were observed as reported pre-viously.[23] The product was confirmed to be magnesium metal by XRD and SEM-EDX measurements (Supporting Figures 2-2 (b) and 2-4). The coulombic efficiency (38%) of the 0.5 M $Mg(TFSA)_2$/triglyme was lower than that of the 0.25 M $Mg(AlCl_2EtBu)_2$/THF (94%) and a large overpotential was required for magnesium dissolution. In contrast to these electrolytes, the cathodic and anodic currents were not observed in the 0.5 M $Mg(TFSA)_2$/2-MeTHF.

2.3.2 Coordination structure of magnesium ions in bulk solution.

The coordination structure of magnesium ions in the $Mg(TFSA)_2$/triglyme and $Mg(TFSA)_2$/2-MeTHF electrolytes is influenced by the cation-anion interactions. Because the $[TFSA]^-$ competes with the solvents to interact with the magnesium ions, if the interaction between magnesium ion and $[TFSA]^-$, magnesium ions coordinate to $[TFSA]^-$ as well as solvent. To examine the interactions between $[TFSA]^-$ and magnesium ions in the bulk solution of $Mg(TFSA)_2$/triglyme and $Mg(TFSA)_2$/2-MeTHF, Raman spectra of these electrolytes were collected. Figures 2-5 (a) and (b) show the Raman spectra in the region between 730 and 760 cm^{-1} for the $Mg(TFSA)_2$/triglyme and $Mg(TFSA)_2$/2-MeTHF electrolytes with various concentrations. The peak corresponding to the CF_3 bending vibration as well as the C-S and S-N stretching vibrations of $[TFSA]^-$ were observed in Figure 2-5.[31] These peaks susceptibly reflect the interaction of $[TFSA]^-$ with the cation.[31-34] It is well known that the peak observed at 739–742 cm^{-1} is assignable to non-coordinated $[TFSA]^-$ (solvent-separated ion pairs (SSIP)), whereas the peak at

745–755 cm^{-1} signifies the $[TFSA]^-$ directly coordinated to cations thereby forming a contact ion pair (CIP) or an aggregate (AGG).[31-34] Figures 2-5 (c) and (d) shows the estimated ratios of SSIP, CIP and AGG for the $Mg(TFSA)_2$/triglyme and $Mg(TFSA)_2$/2-MeTHF with several concentrations by Gaussian fitting. All of the fitting results are shown in Figures 2-6 and 2-7. In the $Mg(TFSA)_2$/triglyme, most of $[TFSA]^-$ exists as non-coordinated free ions (SSIP) while less than 10% of $[TFSA]^-$ are still intact with magnesium ion. The coordination state of $[TFSA]^-$ was not dependent on the concentration of the $Mg(TFSA)_2$/triglyme electrolyte. These results are almost in agreement with a previous report.[35] In stark contrast to the $Mg(TFSA)_2$/triglyme, more than 90% of $[TFSA]^-$ was AGG state and the rest of $[TFSA]^-$ was CIP state in the $Mg(TFSA)_2$/2-MeTHF. The coordination state of $[TFSA]^-$ was not dependent on the concentration of the $Mg(TFSA)_2$/2-MeTHF electrolyte. The difference in coordination state of $[TFSA]^-$ arises from the solvation ability of solvents. The multiple oxygen atoms in triglyme can chelate magnesium ions, and this strong solvation can inhibit coordination of the magnesium ions from $[TFSA]^-$.[35] On the other hand, the solvation ability of monodentate 2-MeTHF is not so high compared to that of triglyme, why magnesium ions are preferentially coordinated by $[TFSA]^-$ in $Mg(TFSA)_2$/2-MeTHF.

Figure 2-8 (a) shows the Raman spectra in the region between 750 cm^{-1} and 930 cm^{-1} for the $Mg(TFSA)_2$/triglyme electrolyte with various concentrations. The Raman band corresponding to the CH_2 rocking vibration and C-O-C stretching vibration of glyme solvent appear in the region between 800 cm^{-1} and 900 cm^{-1}.[36–38] In this region, a band upon non-coordinating to metal ions appears between 800 cm^{-1} and 865 cm^{-1} while a characteristic band upon complex formation with metal ions appears between 865 cm^{-1} and 890 cm^{-1}.[37, 39, 40] The band intensity between 820 cm^{-1} and 860 cm^{-1} decreased with increasing $Mg(TFSA)_2$ concentration whereas the intensity of the band around 880 cm^{-1} increased with increase of $Mg(TFSA)_2$ concentration. These results indicate that triglyme solvent in the $Mg(TFSA)_2$/triglyme coordinates to magnesium ions, which corresponds to the result that more than 90% of $[TFSA]^-$ exists as SSIP. Figure 2-8 (b) shows the Raman spectra in the region between 850 cm^{-1} and 1000 cm^{-1} for the $Mg(TFSA)_2$/2-MeTHF electrolyte with various concentrations. The peaks assigned to the C-C stretching mode and C-O stretching mode of 2-MeTHF was observed at 920 cm^{-1} for the $Mg(TFSA)_2$/2-MeTHF.[41–43] It has been reported that a peak upon the coordination between the THF and cation appears at lower wavenumber than the C-C stretching and C-O stretching of the non-coordinated THF by 10 cm^{-1}.[41–43] The new peak was not observed in the $Mg(TFSA)_2$/2-MeTHF electrolyte, which indicates that 2-MeTHF in the $Mg(TFSA)_2$/2-MeTHF does not coordinate to magnesium ions. These results corresponds to the result that more than 90% of $[TFSA]^-$ exists as AGG in the $Mg(TFSA)_2$/2-MeTHF electrolyte. In the previous reports,[44] the magnesium ions in 0.4 M $Mg(TFSA)_2$/tetraglyme coordinate to tetraglyme more strongly than $[TFSA]^-$, resulting in formation of SSIP. On the other hand, the magnesium ions in 0.4 M $Mg(TFSA)_2$/THF coordinate to $[TFSA]^-$ more strongly than THF, resulting in formation of AGG state. These reports support our present study. It should be noted that the interaction strength between magnesium ions and $[TFSA]^-$ is comparable to that between magnesium ions and triglyme, resulting in that a little $[TFSA]^-$ forms CIP with magnesium ion.

2.3.3 Coordination structure of magnesium ions under applying potential.

Raman spectroscopy clearly showed that the magnesium ions had a different coordination structure in the bulk solutions of the 0.5 M $Mg(TFSA)_2$/triglyme and 0.5 M $Mg(TFSA)_2$/2-MeTHF. To examine the coordination structure of magnesium ions near the negative electrode surface under applied potential, *operando* XAS measurements were conducted for three electrolyte. The XANES and Fourier-transformed EXAFS spectra of each electrolyte are shown in Figures 2-9 and 2-10, respectively.

For the 0.25 M $Mg(AlCl_2EtBu)_2$/THF electrolyte, the XANES spectrum (Figure 2-9 (a)) remained unchanged from the soak state to -0.3 V which is slightly above the potential where magnesium deposition starts (Figure 2-1 (b)). After the magnesium deposition occurred at -3.0 V, the XANES spectrum changed dramatically. The photon energy at the peak top in the XANES spectrum from the soak state to -0.3 V (Figure 2-11 (a)) was nearly constant, indicating that the valence of the magnesium ions did not change. The Fourier-transformed EXAFS spectra (Figure 2-10 (a)) in the soak state showed a peak at 1.8 Å and an additional peak at 2.8 Å, which agreed with a previous report.[24] Similar to the XANES, the EXAFS spectra also remained unchanged from the soak state to -0.3 V (Figure 2-10 (a)). This then changed considerably after magnesium deposition. These results imply that the coordination structure of magnesium ions near the negative electrode surface in the 0.25 M $Mg(AlCl_2EtBu)_2$/THF do not change before magnesium deposition.

The results for the 0.5 M $Mg(TFSA)_2$/triglyme were different from the 0.25 M $Mg(AlCl_2EtBu)_2$/THF (Figure 2-9 (b) and Figure 2-10 (b)). The intensity of the XANES spectrum decreased gradually from the soak state to -0.4 V wherein magnesium deposition does not occur (Figure 2-1 (b)). Then the XANES spectrum changed considerably after magnesium deposition at -1.2 V.

The photon energy at the peak top of the XANES spectrum from the soak state to -0.4 V was nearly constant (Figure 2-11 (b)), indicating that the valence of the magnesium ions did not change. In the EXAFS spectra in the soak state, although two peaks were observed around 1.6 Å and 2.6 Å. The peak at 1.6 Å is assigned to Mg-O bond between magnesium ion and triglyme or between magnesium ion and $[TFSA]^-$ because the magnesium ions in the electrolyte were coordinated to both of triglyme and $[TFSA]^-$ based on the results from Raman spectroscopy. The peak at 2.6 Å is assigned to the Mg-C bond between magnesium ion and triglyme or the Mg-S bond between magnesium ion and $[TFSA]^-$. The Mg-O bond distance did not change from the soak state to -0.4 V, indicating that the valence of the magnesium ions did not change. These results correspond with XANES results. The intensities of the two peaks in the EXAFS spectra decreased gradually from the soak state to -0.4 V, suggesting that the coordination number decreased and/or the local distortion increased between the magnesium ions and triglyme. Because it has been reported that coordination number of lithium ion in lithium glyme solvate liquid system is constant even at applied potential,[45] the intensity decrease of the two peaks is attributed to the increase of local distortion. Because the exchange rate of solvent strongly increase by applied potential,[45] the local distortion increase. The EXAFS spectra changed after magnesium deposition. Although the spectra of the 0.5 M $Mg(TFSA)_2$/2-MeTHF changed in a similar way to the 0.5 M $Mg(TFSA)_2$/triglyme under applied potential, the change was more noticeable (Figures 2-9 (c) and 2-10 (c)). The XANES spectrum gradually became weak and broad from the soak state to -1.4 V at which the magnesium deposition did not occur (Figure 2-1 (b)). The photon energy at the peak top of the XANES spectrum from the soak state to -1.4 V (Figure 2-11 (c)) was nearly constant, meaning that the valence of the magnesium ions did not change. In the EXAFS spectra in the soak state, two peaks were observed around 1.6 Å and 2.6 Å, corresponding to 0.5 M $Mg(TFSA)_2$/triglyme.

The peak at 1.6 Å is assigned to Mg-O bond between magnesium ion and 2-MeTHF or between magnesium ion and $[TFSA]^-$ because the magnesium ions in the electrolyte were coordinated to both of 2-MeTHF and $[TFSA]^-$ based on the results from Raman spectroscopy. The peak at 2.6 Å is assigned to the Mg-C bond between magnesium ion and 2-MeTHF or the Mg-S bond between magnesium ion and $[TFSA]^-$. The Mg-O bond distance did not change from the soak state to -1.4 V, indicating that the valence of the magnesium ions did not change. These results correspond with XANES results. The intensities of the two peaks in the EXAFS spectrum decreased from the soak state to -1.4 V. These changes for the 0.5 M $Mg(TFSA)_2$/2-MeTHF electrolyte were larger than those of the 0.5 M $Mg(TFSA)_2$/triglyme, indicating that the local coordination structure of the magnesium ions in the 0.5 M $Mg(TFSA)_2$/2-MeTHF was distorted more largely by cathodic polarization. Because all of the $[TFSA]^-$ in the 0.5 M $Mg(TFSA)_2$/2-MeTHF coordinates to magnesium ions, coulombic repulsion between the $[TFSA]^-$ coordinating magnesium ion and negatively charged electrode become stronger than 0.5 M $Mg(TFSA)_2$/triglyme, resulting in the larger distortion.

The magnesium deposition/dissolution reactions occurred in the 0.5 M $Mg(TFSA)_2$/triglyme electrolyte, whereas these reactions did not occur in the 0.5 M $Mg(TFSA)_2$/2-MeTHF electrolyte. The valence change of magnesium ions was not observed in the XANES spectra and the expansion of the Mg-O bond was not observed in the EXAFS spectra. The XANES and/or EXAFS results in both electrolyte systems showed intermediate state of Mg^{2+} ion, such as Mg^{+} ion does not formed during under applying potential. These results indicate that the difference of the behavior of magnesium deposition should be affected by the difference of coordinate structure of $[TFSA]^{-}$ ion in both electrolytes. Raman spectroscopy revealed that all of $[TFSA]^{-}$ coordinated to the magnesium ions in the 0.5 M $Mg(TFSA)_2$/2-MeTHF while almost all of the $[TFSA]^{-}$ did not participate in the coordination of magnesium ion in the $Mg(TFSA)_2$/triglyme. Whether reversible magnesium deposition takes place or not, depend on reductive stability of $[TFSA]^{-}$ at the interface. We calculated the LUMO energy levels of $[TFSA]^{-}$ for both coordinated and uncoordinated to magnesium ions, as shown in Figure 2-12. The LUMO energy level of the coordinated $[TFSA]^{-}$ is calculated as -1.38 eV, which is lower than that of the uncoordinated (-0.368 eV). This result indicates that the former $[TFSA]^{-}$ undergoes reduction decomposition more easily than the latter. The calculation result is in good agreement with the preceding work that the $[TFSA]^{-}$ coordinated to magnesium ion undergoes a partial reduction at the reduction potential of the magnesium ions and this reaction competes with magnesium deposition reaction.[44]

2.3.4 Discussion

Figure 2-13 schematically illustrates the behavior of the magnesium ions at the negative electrode/electrolyte. Based on the *operando* XAS measurements and the previous reports,[44] the $[TFSA]^-$ coordinated to magnesium ions in $Mg(TFSA)_2$/2-MeTHF undergoes reduction decomposition and this inhibits magnesium deposition. On the other hand, the 0.5 M $Mg(TFSA)_2$/triglyme electrolyte allows quasi reversible magnesium deposition. This is because most of $[TFSA]^-$ does not coordinate to magnesium ions and such $[TFSA]^-$ is relatively stable for reduction decomposition compared with the coordinated $[TFSA]^-$. It should be noted that some $[TFSA]^-$ still coordinates to magnesium ions even in the highly diluted solution. These coordinated $[TFSA]^-$ should be reduced easily. Indeed, the $[TFSA]^-$ ions in 0.5 M $Mg(TFSA)_2$/BuMeG4 electrolyte react with magnesium metal to form passivation film containing fluorine species.[46] The poor Coulombic efficiency of magnesium deposition/dissolution in $Mg(TFSA)_2$/triglyme is possibly due to the reductive decomposition of $[TFSA]^-$ during magnesium deposition process.

Compared with the $Mg(TFSA)_2$-based electrolytes, the 0.25 M $Mg(AlCl_2EtBu)_2$/THF showed excellent Coulombic efficiency and small polarization for the magnesium deposition/dissolution reactions (Figure 1). The coordination structure of the magnesium ions in the bulk solution of the 0.25 M $Mg(AlCl_2EtBu)_2$/THF electrolyte has a complex structure between the magnesium ions, chlorine, and THF.[24] This structure is completely different from that of the bulk solution of both 0.5 M $Mg(TFSA)_2$/triglyme and $Mg(TFSA)_2$/2-MeTHF electrolytes. *operando* XAS revealed that the coordination structures of the magnesium ions at the interface in the 0.25 M $Mg(AlCl_2EtBu)_2$/THF electrolyte remained unchanged under applied potential because of stability of the complex structure. In the 0.25 M $Mg(AlCl_2EtBu)_2$/THF electrolyte, the passivation film does not form on the negative electrode due to the high reduction stability, resulting in higher coulombic efficiency and smaller polarization than 0.5 M $Mg(TFSA)_2$/triglyme in magnesium deposition/dissolution reactions.

2.4 Conclusions

The coordination structures of the magnesium ions in the bulk solution and at the negative electrode/electrolyte interface of three magnesium electrolytes were analyzed in this study. In the 0.5 M $Mg(TFSA)_2$/triglyme electrolyte, quasi reversible magnesium deposition/dissolution reactions occurred whereas no magnesium deposition reaction occurs in the 0.5 M $Mg(TFSA)_2$/2-MeTHF. *operando* XAS measurements showed that valence of magnesium ions did not change and local structure distortion around magnesium ions increased in both of $Mg(TFSA)_2$/triglyme and $Mg(TFSA)_2$/2-MeTHF electrolytes at the magnesium electrode | electrolyte interface during cathodic polarization. We conclude that controlling the interaction between magnesium ions and $[TFSA]^-$ and suppressing reduction decomposition of $[TFSA]^-$ is crucial to achieve successful magnesium deposition. Indeed, the poor Coulombic efficiency for magnesium deposition/dissolution in $Mg(TFSA)_2$/ether solutions is remarkably improved by incorporating chloride compounds, which facilitate dissociation of MgTFSA.[47–50] The findings in this study will be useful for the future design of new electrolytes for magnesium rechargeable batteries.

References

(1) Armand, M.; Tarascon, J. M., *Nature* **2008**, 451, 652.

(2) Dunn, B.; Kamath, H.; Tarascon, J.-M., *Science* **2011**, 334, 928.

(3) Yoo, H. D.; Shterenberg, I.; Gofer, Y.; Gershinsky, G.; Pour, N.; Aurbach, D., *Energy Environ. Sci.* **2013**, 6, 2265.

(4) Gregory, T. D.; Hoffman, R. J.; Winterton, R. C., *J. Electrochem. Soc.* **1990**, 137, 775.

(5) Novák, P.; Imhof, R.; Haas, O., *Electrochim. Acta* **1999**, 45, 351.

(6) Besenhard, J. O.; Winter, M., *ChemPhysChem* **2002**, 3, 155.

(7) Aurbach, D.; Lu, Z.; Schechter, A.; Gofer, Y.; Gizbar, H; Turgeman, R.; Cohen, Y.; Moshkovich, M.; Levi, E., *Nature* **2000**, 407, 724.

(8) Lu, Z.; Schechter, A.; Moshkovich, M.; Aurbach, D., *J. Electroanal. Chem.* **1999**, 466, 203.

(9) Aurbach, D.; Schechter, A.; Moshkovich, M.; Cohen, Y., *J. Electrochem. Soc.* **2001**, 148, A1004.

(10) Aurbach, D.; Gizbar, H.; Schechter, A.; Chusid, O.; Gottlieb, H. E.; Gofer, Y.; Goldberg, I., *J. Electrochem. Soc.* **2002**, 149, A115.

(11) Mizrahi, O.; Amir, N.; Pollak, E.; Chusid, O.; Marks, V.; Gottlieb, H.; Larush, L.; Zinigrad, E.; Aurbach, D., *J. Electrochem. Soc.* **2008**, 155, A103.

(12) Pour, N.; Gofer, Y.; Major, D. T.; Aurbach, D., *J. Am. Chem. Soc.* **2011**, 133, 6270.

(13) Kim, H. S.; Arthur, T. S.; Allred, G. D.; Zajicek, J.; Newman, J. G.; Rodnyansky, A. E.; Oliver, A. G.; Boggess, W. C.; Muldoon, J., *Nat. Commun.* **2011**, 2, 427.

(14) Barile, C. J.; Spatney, R.; Zavadil, K. R.; Gewirth, A. A., *J. Phys. Chem. C* **2014**, 118, 10694.

(15) Barile, C. J.; Barile, E. C.; Zavadil, K. R.; Nuzzo, R. G.; Gewirth, A. A., *J. Phys. Chem. C* **2014**, 118, 27623.

(16) Mohtadi, R.; Matsui, M.; Arthur, T. S.; Hwang, S.-J., *Angew. Chem. Int. Ed.* **2012**, 51, 9780.

(17) Doe, R. E.; Han, R.; Hwang, J.; Gmitter, A. J.; Shterenberg, I.; Yoo, H. D.; Pour, N.; Aurbach, D., *Chem. Commun.* **2013**, 50, 243.

(18) Shao, Y.; Liu, T.; Li, G.; Gu, M.; Nie, Z.; Engelhard, M.; Xiao, J.; Lv, D.; Wang, C.; Zhang, J.-G.; Liu, J., *Sci. Rep.* **2013**, 3, 3130.

(19) Ha, S.-Y.; Lee, Y.-W.; Woo, S. W.; Koo, B.; Kim, J.-S.; Cho, J.; Lee, K. T.; Choi, N.-S., *ACS Appl. Mater. Interfaces* **2014**, 6, 4063.

(20) Orikasa, Y.; Masese, T.; Koyama, Y.; Mori, T.; Hattori, M.; Yamamoto, K.; Okado, T.; Huang, Z.-D.; Minato, T.; Tassel, C.; Kim, J.; Kobayashi, Y.; Abe, T.; Kageyama, H.; Uchimoto, Y., *Sci. Rep.* **2014**, 4, 5622.

(21) Fukutsuka, T.; Asaka, K.; Inoo, A.; Yasui, R.; Miyazaki, K.; Abe, T.; Nishio, K.; Uchimoto, Y., *Chem. Lett.* **2014**, 43, 1788.

(22) Carter, T. J.; Mohtadi, R.; Arthur, T. S.; Mizuno, F.; Zhang, R.; Shirai, S.; Kampf, J. W., *Angew. Chem. Int. Ed.* **2014**, 53, 3173.

(23) Kim, I.-T.; Yamabuki, K.; Morita, M.; Tsutsumi, H.; Yoshimoto, N., *J. Power Sources* **2015**, 278, 340.

(24) Nakayama, Y.; Kudo, Y.; Oki, H.; Yamamoto, K.; Kitajima, Y.; Noda, K., *J. Electrochem. Soc.* **2008**, 155, A754.

(25) Wan, L. F.; Prendergast, D., *J. Am. Chem. Soc.* **2014**, 136, 14456.

(26) Arthur, T. S.; Glans, P.-A.; Matsui, M.; Zhang, R.; Ma, B.; Guo, J. *Electrochem. Commun.* **2012**, 24, 43.

(27) Benmayza, A.; Ramanathan, M.; Arthur, T. S.; Matsui, M.; Mizuno, F.; Guo, J.; Glans, P.-A.; Prakash, J., *J. Phys. Chem. C* **2013**, 117, 26881.

(28) Nakanishi, K.; Kato, D.; Arai, H.; Tanida, H.; Mori, T.; Orikasa, Y.; Uchimoto, Y.; Ohta, T.; Ogumi, Z., *Review of Scientific Instruments* **2014**, 85, 084103.

(29) Frisch, M. J.; Trucks, G. W.; Schlegel, H. B.; Scuseria, G. E.; Robb, M. A.; Cheeseman, J. R.; Scalmani, G.; Barone, V.; Petersson, G. A.; Nakatsuji, H.; Li, X.; Caricato, M.; Marenich, A. V.; Bloino, J.; Janesko, B. G.; Gomperts, R.; Mennucci, B.; Hratchian, H. P.; Ortiz, J. V.; Izmaylov, A. F.; Sonnenberg, J. L.; Williams-Young, D.; Ding, F.; Lipparini, F.; Egidi, F.; Goings, J.; Peng, B.; Petrone, A.; Henderson, T.; Ranasinghe, D.; Zakrzewski, V. G.; Gao, J.; Rega, N.; Zheng, G.; Liang, W.; Hada, M.; Ehara, M.; Toyota, K.; Fukuda, R.; Hasegawa, J.; Ishida,

M.; Nakajima, T.; Honda, Y.; Kitao, O.; Nakai, H.; Vreven, T.; Throssell, K.; Montgomery, J. J. A.; Peralta, J. E.; Ogliaro, F.; Bearpark, M.; Heyd, J. J.; Brothers, E.; Kudin, K. N.; Staroverov, V. N.; Keith, T. A.; Kobayashi, R.; Normand, J.; Raghavachari, K.; Rendell, A.; Burant, J. C.; Iyengar, S. S.; Tomasi, J.; Cossi, M.; Millam, J. M.; Klene, M.; Adamo, C.; Cammi, R.; Ochterski, J. W.; Martin, R. L.; Morokuma, K.; Farkas, Ö.; Foresman J. B.; Fox, D. J. Gaussian Inc, Wallingford, CT, 2016.

(30) Zhao, Y.; Truhlar, D. G. ,*Theor. Chem. Acc.* **2008**, 120, 215.

(31) Brouillette, D.; Irish, D. E.; Taylor, N. J.; Perron, G.; Odziemkowski, M.; Desnoyers, J. E., *Phys. Chem. Chem. Phys.* **2002**, 4, 6063.

(32) Seo, D. M.; Borodin, O.; Han, S. D.; Boyle, P. D.; Henderson, W. A., *J. Electrochem. Soc.* **2012**, 159, A1489.

(33) Zhang, C.; Ueno, K.; Yamazaki, A.; Yoshida, K.; Moon, H.; Mandai, T.; Umebayashi, Y.; Dokko, K.; Watanabe, M., *J. Phys. Chem. B* **2014**, 118, 5144.

(34) Yamada, Y.; Furukawa, K.; Sodeyama, K.; Kikuchi, K.; Yaegashi, M.; Tateyama, Y.; Yamada, A., *J. Am. Chem. Soc.* **2014**, 136, 5039.

(35) Kimura, T.; Fujii, K.; Sato, Y.; Morita, M.; Yoshimoto, N., *J. Phys. Chem. C* **2015**, 119, 18911.

(36) Yang, X.; Su, Z.; Wu, D.; Hsu, S. L.; Stidham, H. D., *Macromolecules* **1997**, 30, 3796.

(37) Brouillette, D.; Irish, D. E.; Taylor, N. J.; Perron, G.; Odziemkowski, M.; Desnoyers, J. E., *Phys. Chem. Chem. Phys.* **2002**, 4, 6063.

(38) Ducasse, L.; Dussauze, M.; Grondin, J.; Lassegues, J. C.; Naudin, C.; Servant, L., *Phys. Chem. Chem. Phys.* **2003**, 5, 567.

(39) Frech, R.; Huang, W., *Macromolecules* **1995**, 28, 1246.

(40) Grondin, J.; Lassegues, J.-C.; Chami, M.; Servant, L.; Talaga D.; Henderson, W. A., *Phys. Chem. Chem. Phys.* **2004**, 6, 4260.

(41) Ojha, A. K.; Srivastava, S. K.; Peica, N.; Schlücker, S.; Kiefer, W.; Asthana, B. P., *J. Mol. Struct.* **2005**, 735–736, 349.

(42) Benevenuto, R. L.; Alves, W. A., *J. Raman Spectrosc.* **2008**, 39, 490.

(43) Alves, C. C.; Campos, T. B. C.; Alves, W. A., *Spectrochim. Acta, Part A* **2012**, 97, 1085.

(44) Rajput, N. N.; Qu, X.; Sa, N.; Burrell, A. K.; Persson, K. A., *J. Am. Chem. Soc.* **2015**, 137, 3411.

(45) Coles, S. W.; Mishin, M.; Perkin, S.; Fedorov, M. V.; Ivanistsev, V. B., *Phys. Chem. Chem. Phys.* **2017**, 19, 11004.

(46) Kuwata, H.; Matsui, M.; Imanishi, N., *J. Electrochem. Soc.* **2017**, 164, A3229.

(47) Shterenberg, I.; Salama, M.; Yoo, H. D.; Gofer, Y.; Park, J.-B.; Sun Y.-K. Aurbach, D., *J. Electrochem. Soc.* **2015**, 162, A7118.

(48) Salama, M.; Shterenberg, I.; Shimon, L. J. W.; Keinan-Adamsky, K.; Afri, M.; Gofer, Y.; Aurbach, D., *J. Phys. Chem. C* **2017**, 121, 24909

(49) Sa, N.; Pan, B.; Saha-Shah, A.; Hubaud, A. A.; Vaugh-ey, J. T.; Baker, L. A. Liao, C.; Burrell, A. K., *ACS Appl. Mater. Interfaces* **2016**, 8, 16002

(50) Mandai, T.; Akita, Y.; Yagi, S.; Egashira, M.; Munakata H.; Kanamura, K., *J. Mater. Chem. A* **2017**, 5, 3152.

(a)

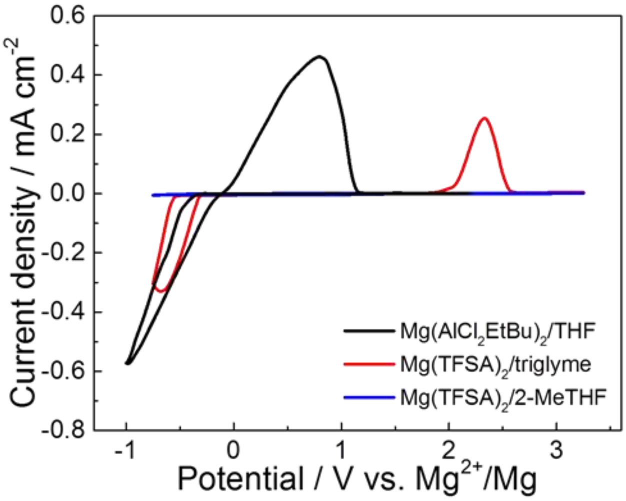

(b)

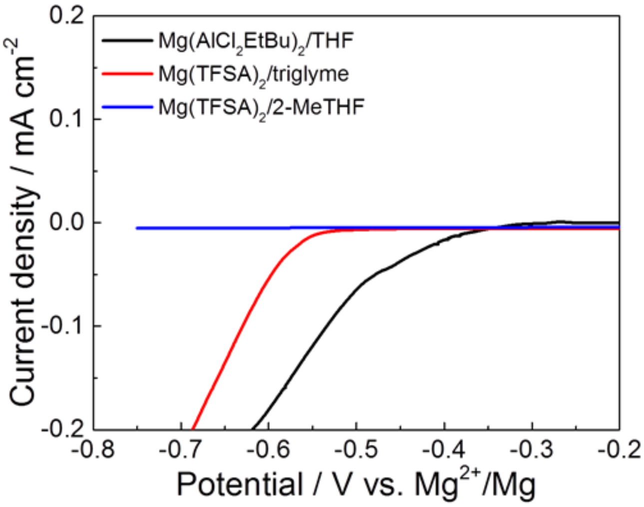

Figure 2-1. (a) Cyclic voltammograms of 0.25 M $Mg(AlCl_2EtBu)_2$/THF, 0.5 M $Mg(TFSA)_2$/triglyme and 0.5 M $Mg(TFSA)_2$/2-MeTHF at a scanning rate of 5 mV/sec. (b) Enlarged figure of (a) between -0.8 V and -0.2 V.

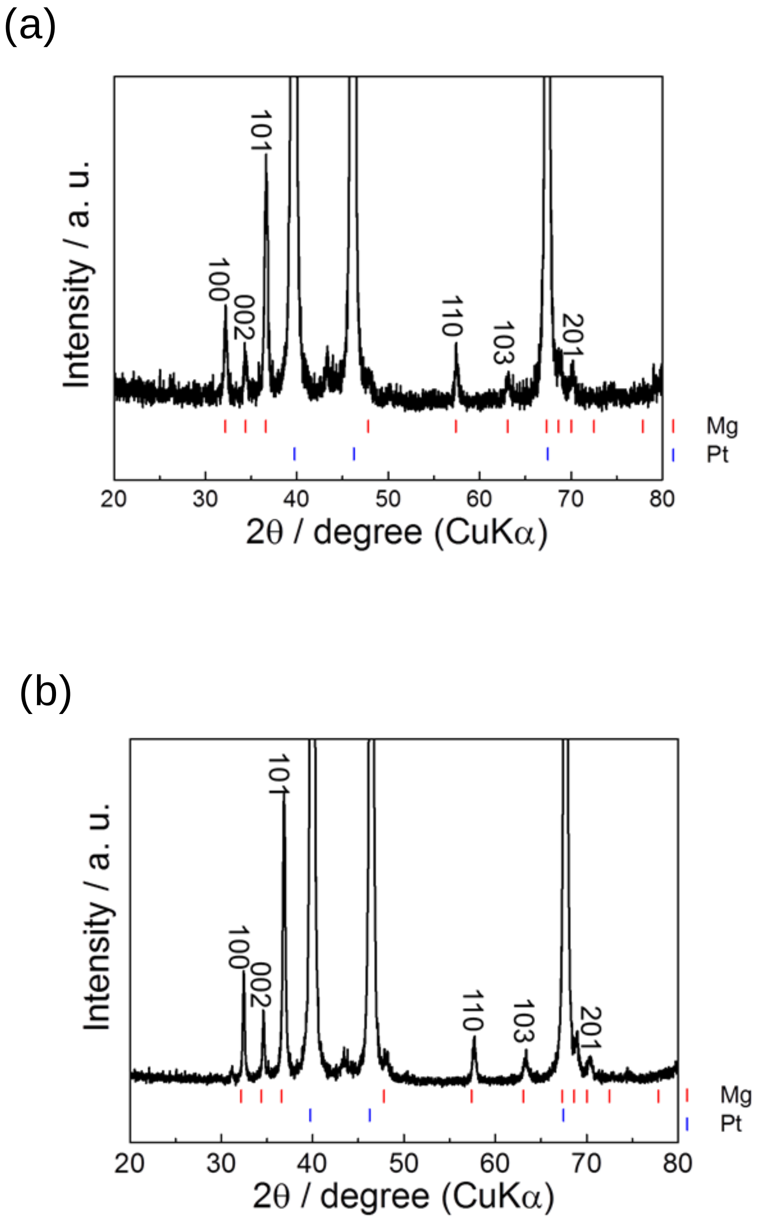

Figure 2-2. XRD patterns of electrodeposited of (a) 0.25 M $Mg(AlCl_2EtBu)_2$/THF and (b) 0.5 M $Mg(TFSA)_2$/triglyme on Pt substrate.

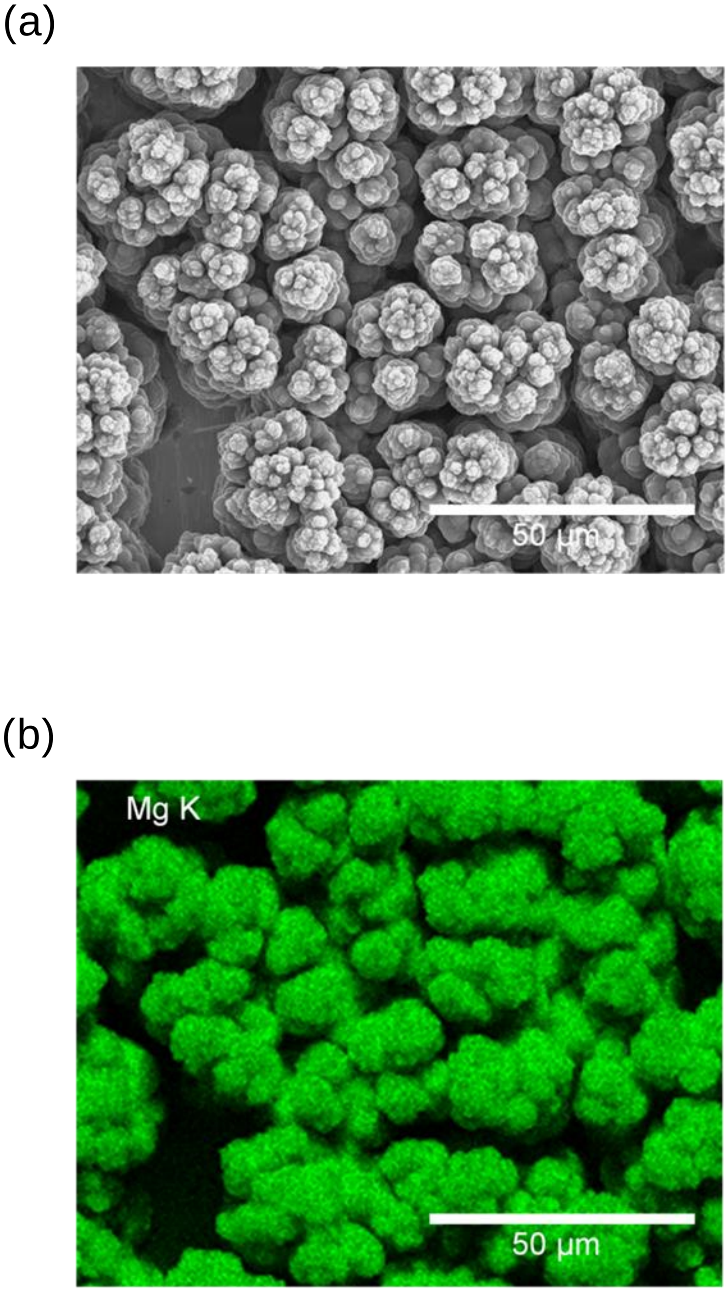

Figure 2-3. (a) SEM image, (b) EDX mapping of Mg *K* for Pt substrate after electrochemical measurements in 0.25 M $Mg(AlCl_2EtBu)_2$/THF.

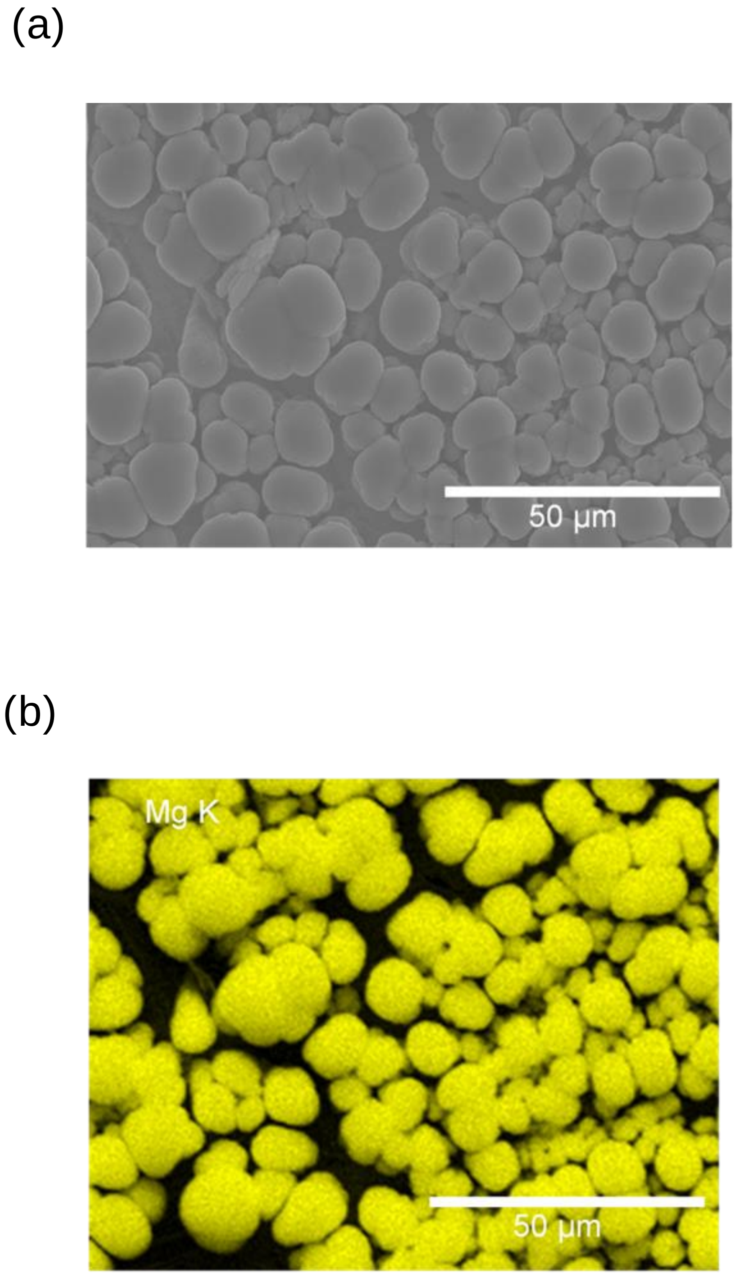

Figure 2-4. (a) SEM image, (b) EDX mapping of Mg *K* for Pt substrate after electrochemical measurements in 0.5 M Mg(TFSA)$_2$/triglyme.

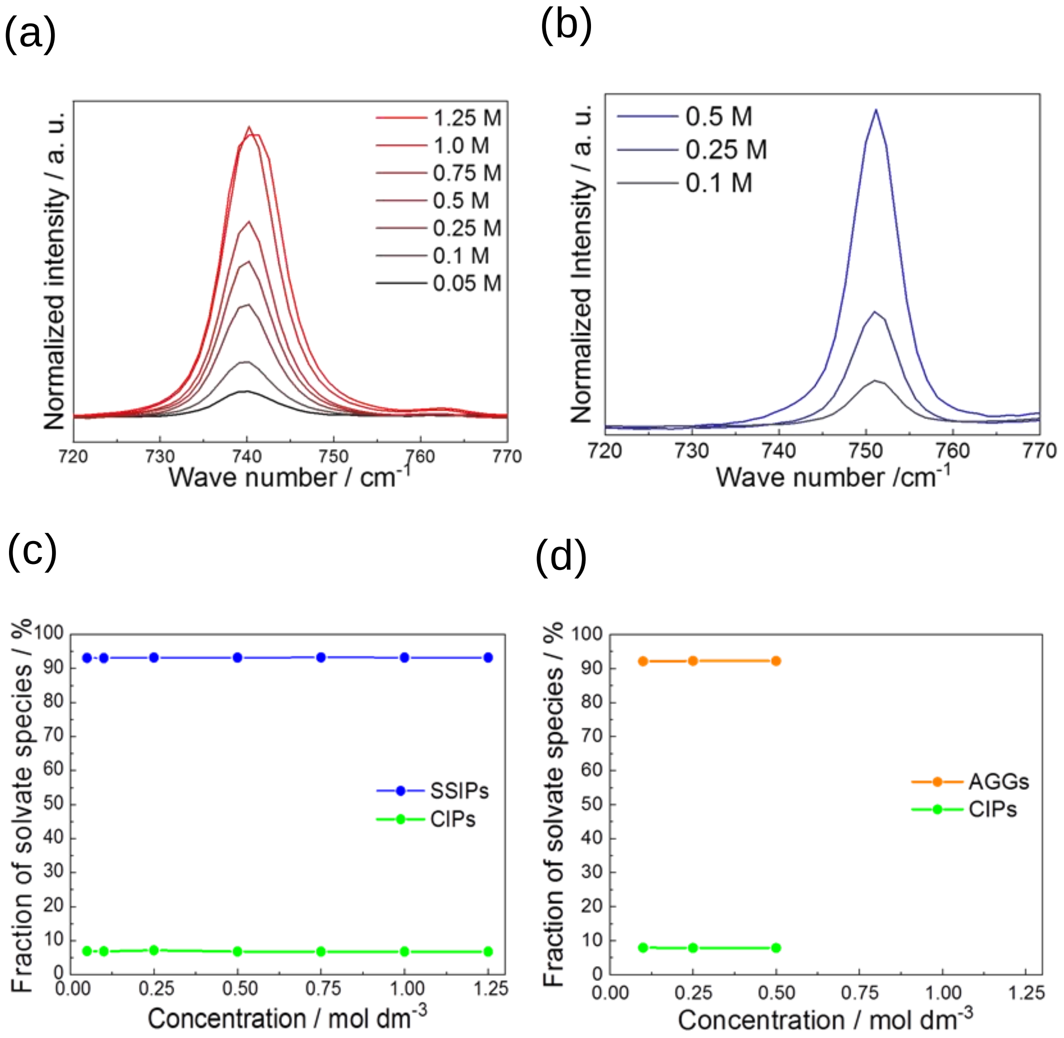

Figure. 2-5. Raman spectra of (a) $Mg(TFSA)_2$/triglyme and of (b) $Mg(TFSA)_2$/2-MeTHF with several concentrations in the wave number between 720 and 770 cm^{-1}. Fraction of solvated species of (c) $Mg(TFSA)_2$/triglyme and of (d) $Mg(TFSA)_2$/2-MeTHF with several concentrations. SSIPs = solvent-separated ion pairs, CIPs = contact ion pairs, and AGGs = aggregate coordinations.”

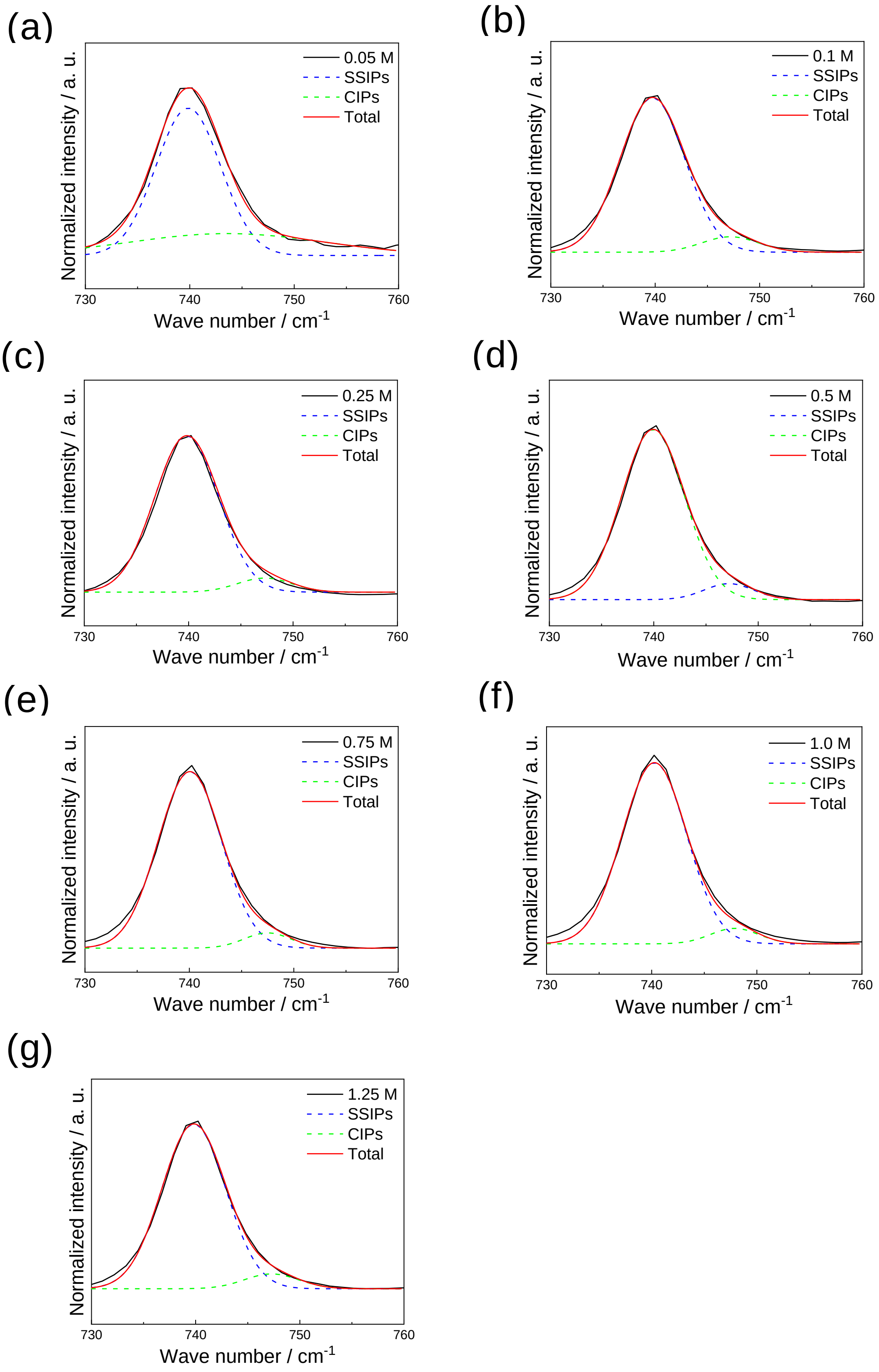

Figure 2-6. Raman spectra and Gaussian fitting results of Mg(TFSA)$_2$/triglyme in several concentration in the wave number between 720 and 760 cm^{-1}.

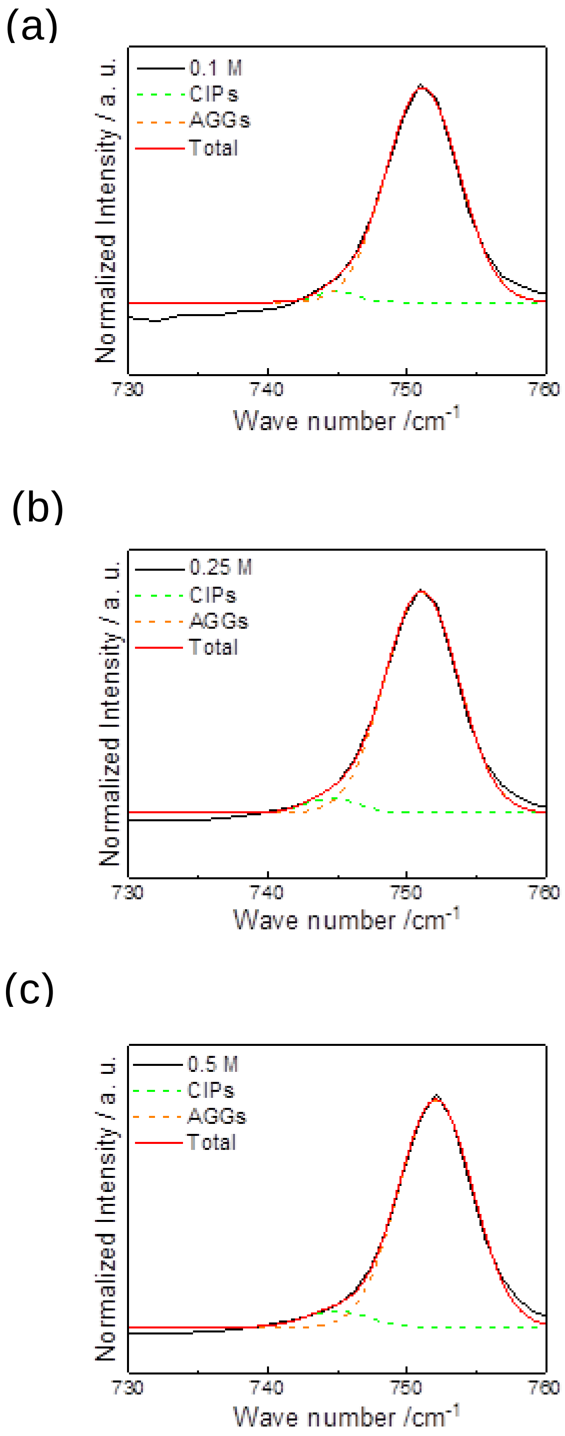

Figure 2-7. Raman spectra and Gaussian fitting results of Mg(TFSA)$_2$/2-MeTHF in several concentration in the wave number between 720 and 760 cm^{-1}.

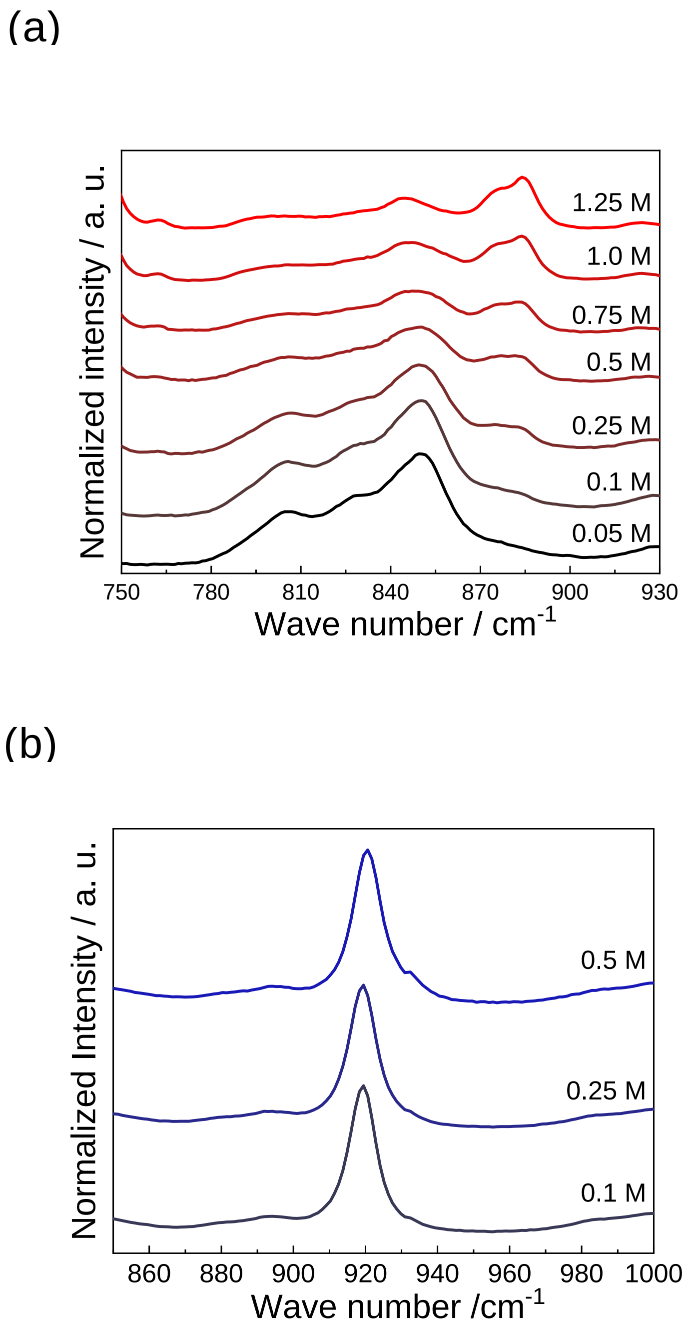

Figure 2-8. Raman spectra of (a) $Mg(TFSA)_2$/triglyme with several concentrations in the wave number between 750 and 930 cm^{-1} and (b) $Mg(TFSA)_2$/2-MeTHF with several concentrations in the wave number between 850 and 1000 cm^{-1}.

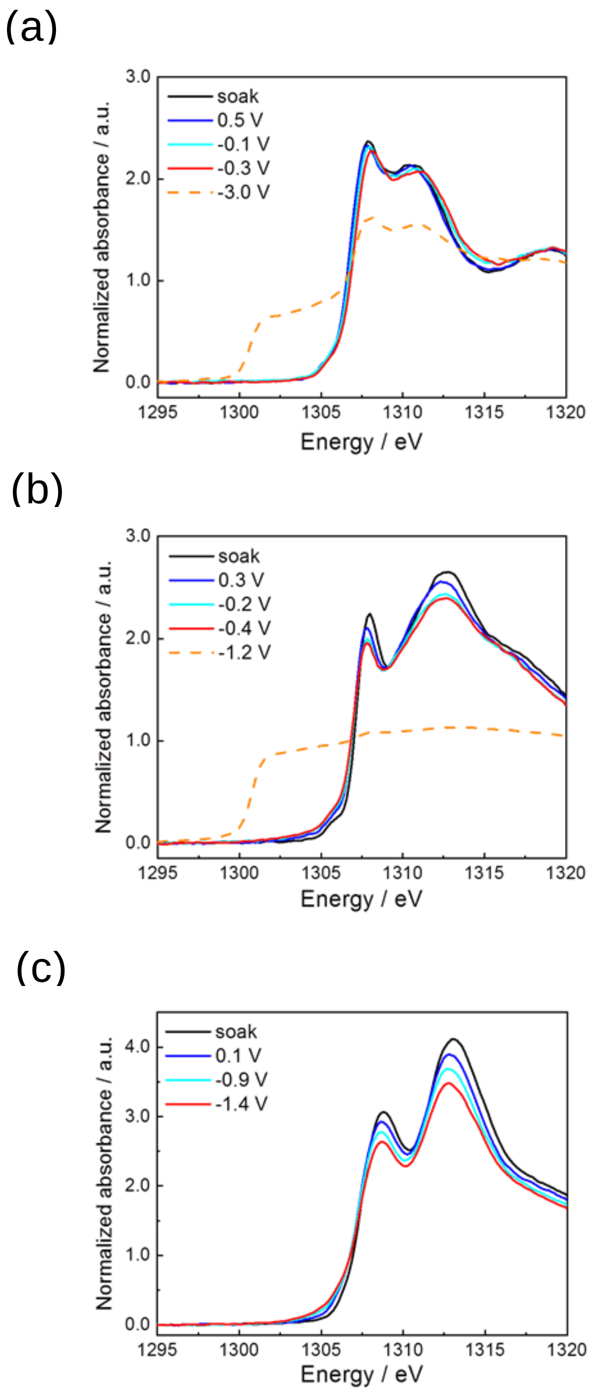

Figure. 2-9. Mg *K*-edge XANES spectra obtained from *operando* XAS measurements for (a) 0.25 M $Mg(AlCl_2EtBu)_2$/THF, (b) 0.5 M $Mg(TFSA)_2$/triglyme, and (c) 0.5 M $Mg(TFSA)_2$/2-MeTHF.

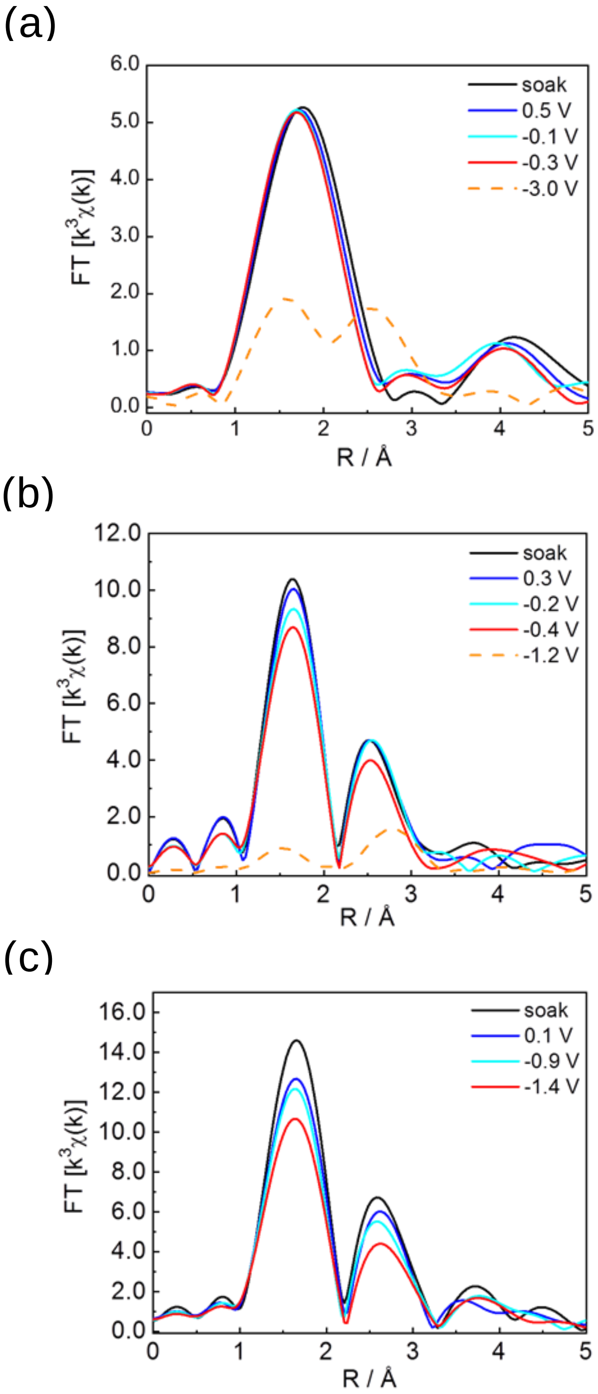

Figure. 2-10. Mg *K*-edge Fourier-transformed EXAFS spectra obtained from *operando* XAS measurements for (a) 0.25 M Mg(AlCl$_2$EtBu)$_2$/THF, (b) 0.5 M Mg(TFSA)$_2$/triglyme, and (c) 0.5 M Mg(TFSA)$_2$/2-MeTHF.

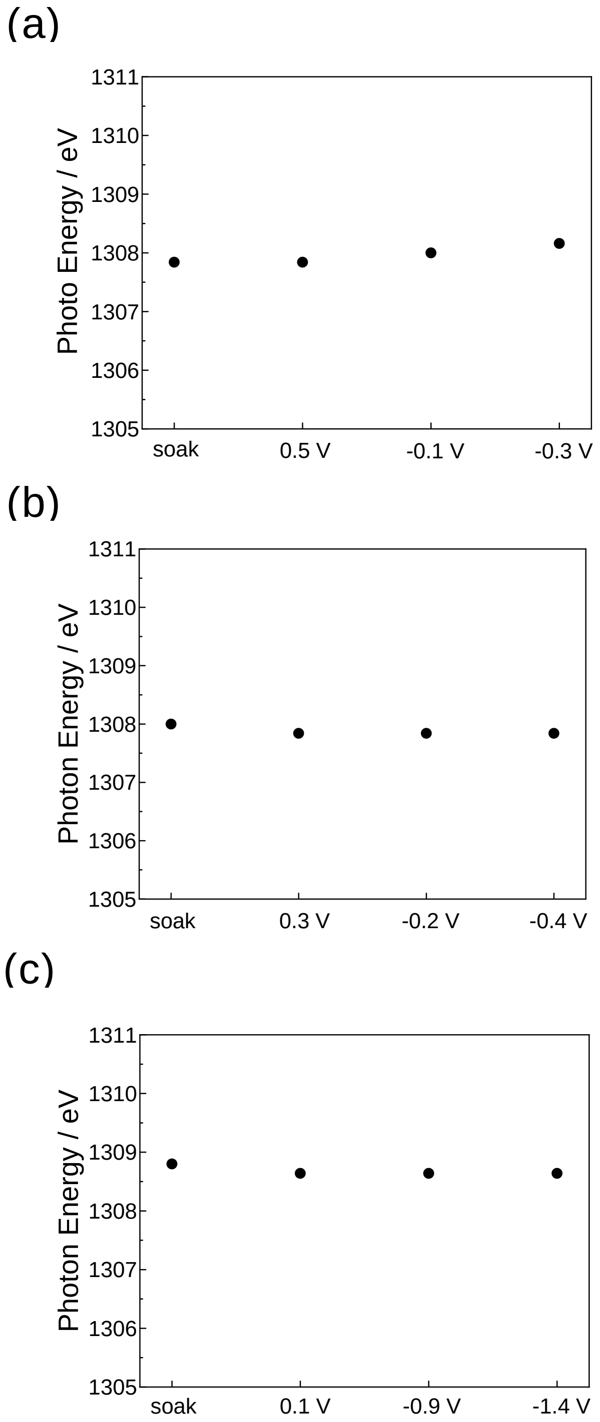

Figure. 2-11. The photon energy at peak top of XANES at soak state and under applying voltage for (a) 0.25 M $Mg(AlCl_2EtBu)_2$,

(b) 0.5 M $Mg(TFSA)_2$/triglyme and (c) 0.5 M $Mg(TFSA)_2$/2-MeTHF using *operando* XAS cell.

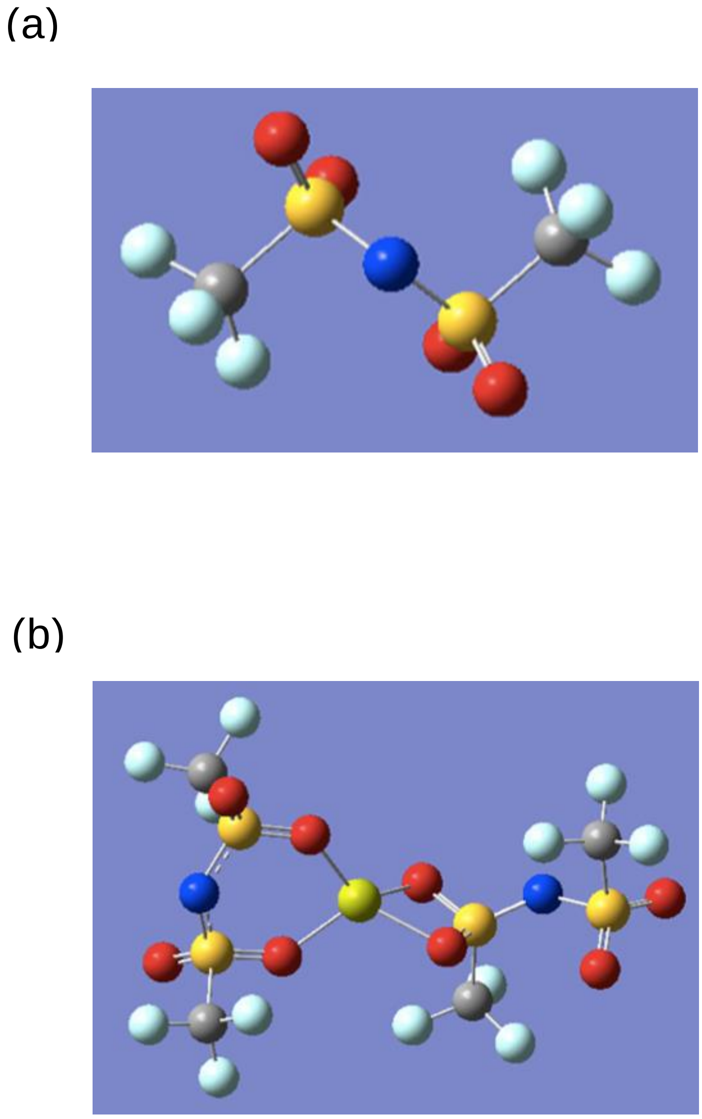

Figure. 2-12. The most stable structure of (a) TFSA in triglyme and (b) Mg(TFSA)$_2$ in triglyme calculated by first principle calculation. Green : Mg, Red : O, Grey : C, Blue : N, Yellow : S, Light blue : F.

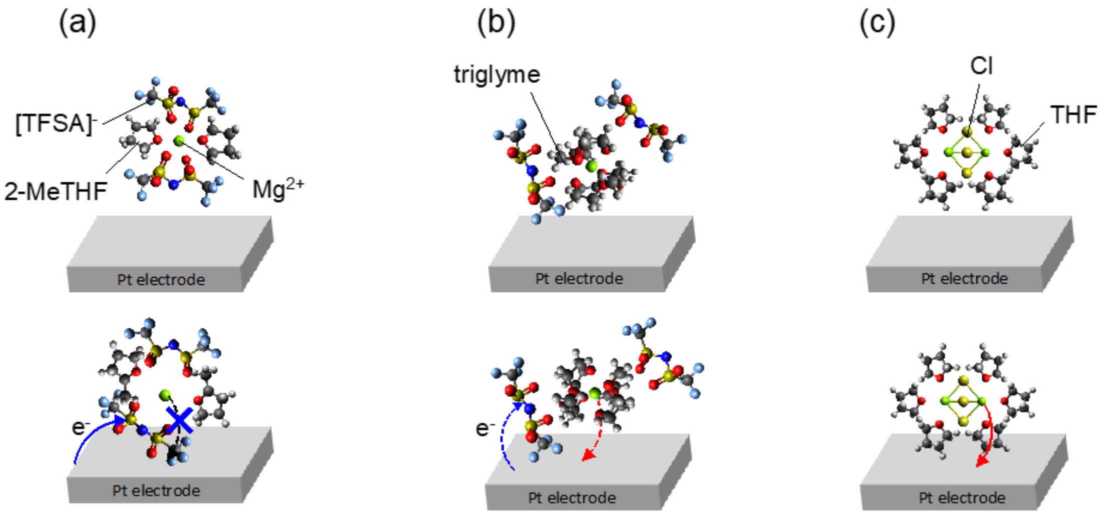

[TFSA]$^-$ coordinating with Mg^{2+} easily decomposes, inhibiting Mg deposition.

[TFSA]$^-$ coordinating with Mg^{2+} decomposes relatively slowly, impeding Mg deposition/dissolution reactions.

Electrolyte is stable during Mg deposition/dissolution.

Figure. 2-13. Schematic illustrations of the behavior of the magnesium ions at the negative electrode/electrolyte interface in the (a) 0.5 M Mg(TFSA)$_2$/2-MeTHF, (b) 0.5 M Mg(TFSA)$_2$/triglyme, and (c) 0.25 M Mg(AlCl$_2$EtBu)$_2$/THF. The top images correspond to the soak state, while the bottom ones correspond to the applied potential condition.

Chapter 3: Bi Anode Reaction Mechanism Investigated by *operando* Soft X-ray Absorption Spectroscopy

3.1 Introduction

The increasing demand for energy storage in electric vehicles and smart grid systems requires battery technologies with energy density beyond current lithium ion batteries. Using a bivalent or trivalent ion instead of lithium ion is a possible route to improve energy density. Magnesium is an especially attractive alternative element due to its small ionic radius and high earth abundance.[1] Although magnesium metal shows high theoretical volumetric capacity (3832 mAh/cm^3), conventional batteries electrolytes made by mixing inorganic magnesium salts with mixed nonaqueous ether/ester solvents, as widely used in lithium ion rechargeable batteries, cannot be used for reversible deposition and dissolution of magnesium metal. This is because a passivation layer is formed at the magnesium metal anode surface that blocks both magnesium ions and electron transport.[2,3] Although Grignard reagents have been widely known as the electrolyte that occur reversible magnesium metal deposition and dissolution reaction,[4-9] the stability of the electrolytes in high potential and their corrosive nature are major problems. One way to resolve these problems is development of new electrolytes. Many electrolytes have developed in recent years, which are magnesium inorganic salts in ether-based solvents[10-17] and ionic liquid.[18, 19] Compared to Grignard reagents, these electrolytes have some advantages, which are higher anodic stability and non-halide. However, the coulombic efficiency of magnesium deposition/dissolution reactions in these electrolytes is still not sufficient.

Another way to solve the above problems is usage for magnesium alloy instead of magnesium metal as the negative electrode. It has been reported that the alloys such as bismuth, antimony, tin, lead and indium are available for magnesium alloying negative electrode.[20-30] Directly prepared magnesium alloys are useful as the negative electrode in order to investigate magnesium-free positive electrode.[31, 32] Among the magnesium alloys, bismuth is an attractive negative electrode because of the theoretical volumetric capacity (1949 mAh/cm$^3{}_{Mg3Bi2}$), which is comparative to lithium metal (2062 mAh/cm^3). Although the theoretical capacity of magnesium alloy is smaller than that of magnesium metal, the electrolytes that is not available for magnesium metal can be used because the redox potential of the alloy is higher than that of the metal. Magnesium alloying reaction into the bismuth electrode occurs in magnesium bis (trifluoromethanesulfonyl) amide (Mg(TFSA)$_2$)/acetonitrile (AN) electrolyte,[20] while magnesium deposition reaction does not occur because of decomposition of AN on magnesium electrode.[33] The interfacial reaction between electrolyte and negative electrode is important in magnesium alloying reaction. However, the reaction mechanism at the interface has not been clarified.

To understand the reaction mechanism at the interface between electrolyte and bismuth electrode, we investigated the coordination structure of magnesium ions at bulk electrolyte and the bismuth electrode surface for $Mg(TFSA)_2$/AN and $Mg(TFSA)_2$)/2-methyltetrahydrofuran (2-MeTHF). We investigated the electronic and local structure of magnesium ions near the negative electrode surface in the each electrolyte during magnesium alloying process using *operando* soft X-ray absorption spectroscopy and discussed the relationship between the coordination structure of magnesium ions and the magnesium alloying reaction.

3.2 Experimental

3.2.1 Material preparation

Bismuth electrode was prepared on Pt substrate by electrodeposition method according to a procedure described in the literature.[34] The electrodeposition was carried out using a three-electrode cell, in which the working and counter electrodes were Pt electrode and the electrolyte was 0.04 M $Bi(NO_3)_3 \cdot 5H_2O$/dimethyl sulfoxide (DMSO). Double-junction reference electrodes equipped with microporous glass membrane were employed for

0.04 M $Bi(NO_3)_3 \cdot 5H_2O$/ DMSO. The inner part of the double-junction reference electrode contains a silver chloride electrode immersed in 3 M NaCl solution, and the outer part contains the electrolyte. The electrodeposited condition was

-0.50 V (vs. Ag/AgCl) for 90 sec.

The as-prepared electrodeposited bismuth was characterized by X-ray diffraction (XRD), scanning electron microscopy (SEM) with energy dispersive X-ray spectroscopy (EDX). After the electrodeposition the cell was disassembled in an argon-filled glove box, and the obtained electrode was washed in DMSO at room temperature. Then, this electrode was dried under vacuum overnight at room temperature.

3.2.2 Electrochemical measurements

We used two different solvent of AN and 2-MeTHF. 0.5 M magnesium bis (trifluoromethanesulfonyl) amide ($Mg(TFSA)_2$)/AN and 0.5 M $Mg(TFSA)_2$/2-MeTHF electrolyte were prepared by stirring $Mg(TFSA)_2$ (KISHIDA CHEMICAL Co., Ltd., >99.9%) with AN (Super dehydrated, Wako Pure Chemical Industries Ltd., >99.8%) or 2-MeTHF (Merck, >98%) in an argon-filled glove box overnight at room temperature, respectively. To decrease the water content, $Mg(TFSA)_2$ salt was dried under vacuum at 180°C for 48 hours and the solvent was dried by using molecular sieves 3A for 48 hours before use. The water content of the prepared electrolytes was confirmed to be less than 30 ppm by Karl Fischer titration.

Electrochemical measurements were carried out using a three-electrode cell. The working electrode was the electrodeposited bismuth on Pt plate. The counter electrode was a magnesium rod. Double-junction reference electrodes equipped with microporous glass membrane were employed for 0.5 M $Mg(TFSA)_2$/AN and 0.5 M $Mg(TFSA)_2$/2-MeTHF. For 0.5 M $Mg(TFSA)_2$/AN, the inner part contains a silver electrode immersed in 0.1 M $AgNO_3$/AN, and the outer part contains the electrolyte. For 0.5 M $Mg(TFSA)_2$/2-MeTHF, the inner part contained lithium metal immersed in 0.1 M LiTFSA/propylene carbonate (PC), and the outer part contained the electrolyte. Cyclic voltammetry was carried out at 25°C with a scanning potential rate of 100 μV/sec. The potential range was set from -2.5 V to -1.5 V vs. Ag^+/Ag (corresponding to 0 to 1.0 V vs. Mg^{2+}/Mg) for 0.5 M $Mg(TFSA)_2$/AN and from 0.8 V to 1.8 V vs. Li^+/Li (corresponding to 0 to 1.0 V vs. Mg^{2+}/Mg) for 0.5 M $Mg(TFSA)_2$/2-MeTHF, respectively.

3.2.3 XRD measurements

X-ray diffraction (XRD), scanning electron microscopy (SEM) and energy dispersive X-ray spectroscopy (EDX) were carried out after the magnesium ion alloying reaction. After the reaction, the cells were disassembled in an argon-filled glovebox, and the electrodes were washed in AN, 2-MeTHF, respectively. Then, these electrodes were dried in an argon-filled glove box overnight at room temperature.

3.2.4 Raman spectroscopy

The Raman spectra of the magnesium electrolytes were measured by

LabRAM HR-800 (HORIBA Ltd.) equipped with He-Ne laser (632 nm) at room temperature. The measurement range was set from 200 to 2400 cm^{-1} for $Mg(TFSA)_2$/AN with several concentration. The electrolyte was put into glass vessel and tightly sealed in it in an argon-filled glove box to avoid it from the air exposure.

3.2.5 *operando* soft X-ray absorption spectroscopy

operando XAS spectra of Mg K-edge for the electrolytes were measured by partial fluorescence yield method at the beam line of the SPring-8 synchrotron radiation facility (BL27SU) in Hyogo, Japan. A custom made three-electrode cell, which was previously reported, [35] was used for *operando* XAS measurements. Titanium was deposited by the thickness of 5 nm on silicon nitride window with the thickness of 300 nm (Norcada Inc.) using magnetron sputtering. Subsequently, platinum was deposited by the thickness of 30 nm on the prepared Ti/Si_3N_4. Then, bismuth was electrodeposited on the prepared $Pt/Ti/Si_3N_4$ by the method as mentioned above. The counter electrode was a magnesium plate. The reference electrode was magnesium bismuthide (Mg_3Bi_2) on platinum plate. The operando cell was assembled in an argon-filled glove box and transferred into a chamber for the XAS measurements in ultrahigh vacuum. *operando* XAS measurements were performed under keeping the potential of the working electrode to several different potentials before the surface of bismuth anode was magnesiated. Then, bismuth anode was magnesiated on the working electrode by applying potential step method, and additional XAS measurements were performed. The analysis of the obtained XAS spectra was performed with REX2000 XAS analysis software (Rigaku Co., Inc.), allowing for alignment and normalization.

3.3 Results and Discussion

3.3.1 Characterization of Bi anode after electrochemical measurements

The electrode prepared was single phase of bismuth and deposited densely and uniformly on Pt substrate, which were characterized by XRD and SEM-EDX measurements (Figure 3-1 and 3-2). Figure 3-3 shows that cyclic voltammograms of bismuth electrode in 0.5 M $Mg(TFSA)_2$/AN and 0.5 M $Mg(TFSA)_2$/2-MeTHF. In 0.5 M $Mg(TFSA)_2$/AN, cathodic and anodic peaks, which are attributed to magnesium ion alloying and dealloying reactions, were observed around 0.4 V vs. Mg^{2+}/Mg as previously reported.[21] The alloying of magnesium ion into the bismuth electrode was confirmed by XRD and SEM-EDX measurements (Figure 3-4 (a) and 3-5. XRD detected magnesium bismuthide (Mg_3Bi_2) and SEM-EDX observed magnesium element from the electrode after magnesium ion alloying reaction. In contrast to 0.5 M $Mg(TFSA)_2$/AN, the cathodic current attributed to magnesium ion alloying reaction did not observed in 0.5 M $Mg(TFSA)_2$/2-MeTHF, and magnesium was not detected in the bismuth electrode after electrochemical measurement by

XRD and SEM-EDX (Supporting Figure 3-4 (b) and 3-6).

3.3.2 Coordination structure of magnesium ions in bulk electrolyte.

To examine coordination state of anion in the electrolytes, Raman spectroscopy was performed. Figure 3-7 (a) and (b) show the Raman spectra ranging from 730 to 760 cm^{-1} in Mg(TFSA)$_2$/AN and Mg(TFSA)$_2$/2-MeTHF in several concentration. The peak emerged in the wavenumber range is assigned to the CF$_3$ bending vibration, the S-N and C-S stretching vibration of [TFSA]$^-$ and it reflects on the interaction between [TFSA]$^-$ and cation.[36-40] The peak at 739 - 742 cm^{-1} reflects that [TFSA]$^-$ exists as solvent-separated ion pairs (SSIPs), while the peak at 745 - 755 cm^{-1} reflects that [TFSA]$^-$ directly coordinates to cation in the form of contact ion pairs (CIPs) and/or aggregates (AGGs).[36-40] The coordination state of [TFSA]$^-$ in the Mg(TFSA)$_2$/AN and Mg(TFSA)$_2$/2-MeTHF was estimated by Gaussian fitting as shown in Figure 3-7 (c) and (d). All fitting results are shown in Figure 3-8 and 3-9. In the Mg(TFSA)$_2$/AN, more than 85% of [TFSA]$^-$ exist in the states of SSIPs while less than 15% of [TFSA]$^-$ still exists as CIPs states. On the other hand, in the Mg(TFSA)$_2$/2-MeTHF, more than 90% of [TFSA]$^-$ exists as AGGs and the rest of [TFSA]$^-$ exists as CIPs.

Figure 3-10 (a) shows the Raman spectra in the region 2200 cm^{-1} and 2350 cm^{-1} for the Mg(TFSA)$_2$/AN in several concentration. The peak assigned to C≡N stretching band of AN was observed in the Mg(TFSA)$_2$/AN. In the

$Mg(TFSA)_2$/AN, three peaks appeared at 2257 cm^{-1}, 2297 cm^{-1} and 2320 cm^{-1}. The peaks at 2257 cm^{-1} is assigned to the C≡N band of acetonitrile molecules that are not coordinated to magnesium ions.[40] The other peaks are assigned to the C≡N band of acetonitrile molecules that are coordinated to magnesium ions, which corresponds to A_{1g} and E_g modes under the O_h symmetry.[40] The peak intensity at 2257 cm^{-1} decrease whereas the peak intensity at 2297 cm^{-1} and 2320 cm^{-1} increase with increasing $Mg(TFSA)_2$ concentration. The concentration dependency of the Raman spectra corresponds to the previous report.[40] These results indicate that AN solvent in the $Mg(TFSA)_2$/AN coordinates to magnesium ions. It has been reported that a magnesium ion in single crystal of $[Mg(AN)_6][TFSA]_2$ coordinates with 6 AN molecules and is separated from $[TFSA]^-$.[40] These results were in good agreement of the results that more than 85% of $[TFSA]^-$ exists as SSIP. Figure 3-10 (b) shows the Raman spectra in the region between 850 cm^{-1} and 1000 cm^{-1} for the $Mg(TFSA)_2$/2-MeTHF electrolyte with various concentrations. The peaks assigned to the C-O stretching mode of the 2-MeTHF was observed at 920 cm^{-1} for the $Mg(TFSA)_2$/2-MeTHF.[41–43] It is known that a peak upon the coordination between the THF and cation appears at lower wavenumber than the C-C stretching and C-O stretching of the non-coordinated THF by 10 cm^{-1}.[41–43] The new peak was not observed in the $Mg(TFSA)_2$/2-MeTHF electrolyte, which indicates that 2-MeTHF in the $Mg(TFSA)_2$/2-MeTHF does not coordinate to magnesium ions. These results corresponds to the result that more than 90% of $[TFSA]^-$ exists as AGG in the $Mg(TFSA)_2$/2-MeTHF electrolyte.

3.3.3 *operando* X-ray Absorption Spectroscopy Measurements

Further coordination structure of magnesium ions on near the surface of the bismuth electrode under applying potential was examined using *operando* soft X-ray absorption spectroscopy. Figure 3-11 and 3-12 show the obtained Mg *K*-edge XANES and Fourier-transformed EXAFS spectra for 0.5 M $Mg(TFSA)_2$/AN and 0.5 M $Mg(TFSA)_2$/2-MeTHF at several voltages, respectively. The EXAFS oscillations for 0.5 M $Mg(TFSA)_2$/AN and 0.5 M $Mg(TFSA)_2$/2-MeTHF at several voltages were shown in Figure 3-13.

For 0.5 M $Mg(TFSA)_2$/AN, the intensity of XANES (Figure 3-11 (a)) gradually changed from the soak state to 0.35 V slightly before the voltage which magnesium alloying starts (Figure. 3-3). However, the photon energy at the peak top of the XANES spectrum from the soak state to 0.35 V was nearly constant, indicating that the valence of the magnesium ions did not change. The XANES drastically changed after magnesium alloying reaction because of the difference of electronic structure of Mg^{2+} ion in the electrolyte and Mg^{2+} ion in bismuth alloy. These results clearly indicate that intermediate state of Mg^{2+} ion, such as Mg^+ ion does not formed during under alloy formation.

Two peaks were observed around 1.7 Å and 2.7 Å in the EXAFS spectra (Figure 3-11 (b)). The peak at 1.7 Å is assigned to the Mg-N bond between magnesium ion and AN or the Mg-O bond between magnesium ion and $[TFSA]^-$ because the magnesium ions in the electrolyte were coordinated to both of AN and $[TFSA]^-$ based on the results from Raman spectroscopy. The peak at 2.7 Å is assigned to the Mg-C bond between magnesium ion and AN or the Mg-S bond between magnesium ion and $[TFSA]^-$. The Mg-N or Mg-O bond distance did not change from the soak state to 0.35 V indicating that the valence of the magnesium ions did not change. These results correspond with XANES results. The intensities of the two peaks in the EXAFS spectrum decreased from the soak state to 0.35 V, suggesting that the coordination number decreased and/or local distortion increased around magnesium ions. Based on the reported DFT calculation, the coordination number of lithium ion in lithium glyme solvate liquid system does not change on negatively charged electrode surface, exchange rate of solvent strongly increase by potential gradient.[44] The intensity decrease of the two peaks should be attributed to the increase of local distortion by applied potential. The EXAFS spectra also changed after alloy formation.

Except drastic change with magnesium ion alloying reaction, the XAS results of 0.5 M $Mg(TFSA)_2$/2-MeTHF were similar to 0.5 M $Mg(TFSA)_2$/AN. The XANES gradually changed from the soak state to -0.6 V (Figure 3-12 (a)). The photon energy at the peak top of the XANES spectrum from the soak state to -0.6 V was nearly constant, meaning that the valence of the magnesium ions did not change. Two peaks were observed around 1.6 Å and 2.6 Å in the EXAFS spectra (Figure 3-12 (b)). The peak at 1.6 Å is assigned to the Mg-O bond between magnesium ion and 2-MeTHF or between magnesium ion and $[TFSA]^-$. The peak at 2.6 Å is assigned to the Mg-C bond between magnesium ion and 2-MeTHF or the Mg-S bond between magnesium ion and $[TFSA]^-$ because the magnesium ions in the electrolyte were coordinated to both of 2-MeTHF and $[TFSA]^-$ based on the results from Raman spectroscopy. The Mg-O bond distance did not change from the soak state to -0.6 V, indicating that the valence of the magnesium ions did not change. These results correspond with XANES results. The intensities of the two peaks in the EXAFS spectrum decreased at -0.6 V, suggesting that the local distortion of magnesium ions increased.

3.3.4 Discussion

The magnesium alloying/dealloying reactions in bismuth electrode occurred in the 0.5 M $Mg(TFSA)_2$/AN electrolyte, whereas these reactions did not occur in the 0.5 M $Mg(TFSA)_2$/2-MeTHF electrolyte. The XANES and/or EXAFS results in both electrolyte systems showed intermediate state of Mg^{2+} ion, such as Mg^+ ion does not formed during under applying potential. These results indicate that the difference of the behavior of alloy formation should be affected by the difference of coordinate structure of $[TFSA]^-$ in both electrolytes. Raman spectroscopy revealed that almost all of the $[TFSA]^-$ did not participate in the coordination of magnesium ion in the $Mg(TFSA)_2$/AN. On the other hand, all of $[TFSA]^-$ coordinated to the magnesium ions in the 0.5 M $Mg(TFSA)_2$/

2-MeTHF. We calculated that the LUMO energy levels of the [TFSA]$^-$ coordinated to magnesium ions in AN and 2-MeTHF solvents as shown in Figure 3-14. The LUMO energy levels of the [TFSA]$^-$ coordinated to magnesium ions (ca. -1.63 eV) in AN is lower than that of the [TFSA]$^-$ uncoordinated (ca. -0.719 eV). The LUMO energy levels of the [TFSA]$^-$ coordinated to magnesium ions (ca. -1.66 eV) in 2-MeTHF is lower than that of the [TFSA]$^-$ uncoordinated (ca. -0.349 eV). These results indicate that the [TFSA]$^-$ coordinated to magnesium ions underdoes reduction decomposition more easily than the [TFSA]$^-$ uncoordinated. The calculated results correspond to the previous report[45] in which the [TFSA]$^-$ coordinated to magnesium ion undergoes a partial reduction at the reductive potential of the magnesium ions and this reaction competes with magnesium deposition reaction.

Based on the *operando* XAS measurements and the previous report,[45] the reductive decomposition of [TFSA]$^-$ should occur at the potential of magnesium alloying/dealloying in the bismuth electrode, which is ca. 0.4 V more positive than the potential of magnesium deposition/dissolution. The behavior of magnesium ions at the bismuth electrode/electrolyte interface is schematically illustrated in Figure 3-15. In the Mg(TFSA)$_2$/2-MeTHF, the [TFSA]$^-$ coordinated to magnesium ions undergoes reduction decomposition, resulting in inhibiting the alloying reaction into the bismuth electrode. On the other hand, the 0.5 M Mg(TFSA)$_2$/AN electrolyte, reduction decomposition of the [TFSA]$^-$ is suppressed because most of [TFSA]$^-$ does not coordinate to magnesium ions and such $[TFSA]^-$ is relatively stable for reduction decomposition, resulting in reversible magnesium ions alloying/dealloying reactions.

We also reported the poor coulombic efficiency of magnesium deposition/dissolution in $Mg(TFSA)_2$/triglyme,[14] which is probably caused by the reductive decomposition of $[TFSA]^-$ during magnesium deposition process. The reduction decomposition occurs relatively slowly because the potential of magnesium ions alloying/dealloying in the bismuth electrode is ca. 0.4 V more positive than that of magnesium deposition/dissolution, resulting in higher coulombic efficiency of bismuth electrode.

3.4 Conclusions

In this work, we examined the coordination structure of magnesium ions in two magnesium electrolytes at the interface between bismuth electrode and electrolyte under applying voltage. In the case of 0.5 M $Mg(TFSA)_2$/AN, the reduction decomposition of $[TFSA]^-$ is suppressed because almost all of $[TFSA]^-$ does not coordinate to magnesium ions, resulting in reversible magnesium ions alloying/dealloying in the bismuth electrode. On the other hand, the alloying reaction cannot occur in 0.5 M $Mg(TFSA)_2$/2-MeTHF because $[TFSA]^-$, which strongly coordinates with magnesium ions, undergoes reduction decomposition, inhibiting the alloying reaction of magnesium ions into the bismuth electrode. Reducing the interaction between magnesium ions and anion is important for achieving magnesium alloying reaction.

References

(1) Yoo, H. D.; Shterenberg, I.; Gofer, Y.; Gershinsky, G.; Pour, N.; Aurbach, D., *Energy Environ. Sci.* **2013**, 6, 2265.

(2) Lu, Z.; Schechter, A.; Moshkovich, M.; Aurbach, D., *J. Electroanal. Chem.* **1999**, 466, 203.

(3) Gregory, T. D.; Hoffman, R. J.; Winterton, R. C., *J. Electrochem. Soc.* **1990**, 137, 775.

(4) Aurbach, D.; Schechter, A.; Moshkovich, M.; Cohen, Y., *J. Electrochem. Soc.* **2001**, 148, A1004

(5) Aurbach, D.; Gizbar, H.; Schechter, A.; Chusid, O.; Gottlieb, H. E.; Gofer, Y.; Goldberg, I., *J. Electrochem. Soc.* **2002**, 149, A115.

(6) Mizrahi, O.; Amir, N.; Pollak, E.; Chusid, O.; Marks, V.; Gottlieb, H.; Larush, L.; Zinigrad, E.; Aurbach, D., *J. Electrochem. Soc.* **2008**, 155, A103.

(7) Pour, N.; Gofer, Y.; Major, D. T.; Aurbach, D., *J. Am. Chem. Soc.* **2011**, 133, 6270.

(8) Kim, H. S.; Arthur, T. S.; Allred, G. D.; Zajicek, J.; Newman, J. G.; Rodnyansky, A. E.; Oliver, A. G.; Boggess, W. C.; Muldoon, J., *Nat. Commun.* **2011**, 2, 427.

(9) Barile, C. J.; Spatney, R.; Zavadil, K. R.; Gewirth, A. A., *J. Phys. Chem. C* **2014**, 118, 10694.

(10) Mohtadi, R.; Matsui, M.; Arthur, T. S.; Hwang, S.-J., *Angew. Chem.*

Int. Ed. **2012**, 51, 9780.

(11) Doe, R. E.; Han, R.; Hwang, J.; Gmitter, A. J.; Shterenberg, I.; Yoo, H. D.; Pour, N.; Aurbach, D., *Chem. Commun.* **2013**, 50, 243.

(12) Shao, Y.; Liu, T.; Li, G.; Gu, M.; Nie, Z.; Engelhard, M.; Xiao, J.; Lv, D.; Wang, C.; Zhang, J.-G.; Liu, J., *Sci. Rep.* **2013**, 3, 3130.

(13) Ha, S.-Y.; Lee, Y.-W.; Woo, S. W.; Koo, B.; Kim, J.-S.; Cho, J.; Lee, K. T.; Choi, N.-S., *ACS Appl. Mater. Interfaces* **2014**, 6, 4063.

(14) Orikasa, Y.; Masese, T.; Koyama, Y.; Mori, T.; Hattori, M.; Yamamoto, K.; Okado, T.; Huang, Z.-D.; Minato, T.; Tassel, C.; Kim, J.; Kobayashi, Y.; Abe, T.; Kageyama, H.; Uchimoto, Y., *Sci. Rep.* **2014**, 4, 5622.

(15) Fukutsuka, T.; Asaka, K.; Inoo, A.; Yasui, R.; Miyazaki, K.; Abe, T.; Nishio, K.; Uchimoto, Y., *Chem. Lett.* **2014**, 43, 1788.

(16) Carter, T. J.; Mohtadi, R.; Arthur, T. S.; Mizuno, F.; Zhang, R.; Shirai, S.; Kampf, J. W., *Angew. Chem. Int. Ed.* **2014**, 53, 3173.

(17) Shterenberg, I; Salama, M.; Yoo, H. D.; Gofer, Y.; Park, J.-B.; Sun, Y. –K.; Aurbach, D., *J. Electrochem. Soc.* **2015**, 162, A7118.

(18) Vardar, G.; Sleightholme, A. E. S.; Naruse, J.; Hiramatsu, H.; Siegel, D. J.; Monroe, C. W., *ACS Appl. Mater. Interfaces* **2014**, 6. 18033.

(19) Watkins, T.; Kumar, A.; Buttry, D. A., *J. Am. Chem. Soc.* **2016**, 138, 641.

(20) Arthur, T. S.; Singh, N.; Matsui, M., *Electrochem. Commun.* **2012**, 16, 103

(21) Singh, N.; Arthur, T. S.; Ling, C.; Matsui, M.; Mizuno, F., *Chem. Commun.* **2013**, 49, 149.

(22) Shao, Y.; Gu, M.; Li, X.; Nie, Z.; Zuo, P.; Li G.; Liu, T.; Xiao, J.; Cheng, Y.; Wang, C.; Zhang. J.-G.; Liu, J. *Nano Lett.* **2014**, 14, 255.

(23) Parent, L. R.; Cheng, Y.; Sushko, P. V.; Shao, Y.; Liu, J.; Wang, C.-M.; Browning, N. D., *Nano Lett.* **2015**, 15, 1177.

(24) Benmayaza, A.; Ramanathan, M.; Singh, N.; Mizuno, F.; Prakash, J., *J. Electrochem. Soc.* **2015**, 162, A1630.

(25) DiLeo, R. A.; Zhang, Q.; Marschilok, A. C.; Takeuchi, K. J.; Takeuchi, E. S., *ECS Electrochem. Lett.* **2015**, 4, A10.

(26) Periyapperuma, K.; Tran, T. T.; Purcell, M. I.; Obrovac, M. N., *Electrochim. Acta* **2015**, 165, 162.

(27) Murgia, F.; Weldekidan, E. T.; Stievano, L.; Monconduit, L.; Berthelot, R., *Electrochem. Commun.* **2015**, 60, 56.

(28) Murgia, F.; Stievano, L.; Monconduit, L.; Berthelot, R., *J. Mater. Chem. A* **2015**, 3, 16478.

(29) Kravchyk, K. V.; Piveteau, L.; Caputo, R.; He, M.; Stadie, N. P.; Bodnarchuk, M. I.; Lechner, R. T.; Kovalenko, M. V., *ACS Nano* **2018**, 12, 8297.

(30) Liu, Z.; Lee, J.; Xiang, G.; Glass, H. F. J. ; Keyzer, E. N.; Dutton, S. E.; Grey, C. P., *Chem. Commun.* **2017**, 53, 743.

(31) Tan, Y.-H.; Yao, W.-T.; Zhang, T.; Ma, T.; Lu, L.-L.; Zhou, F.; Yao, H.-

B.; Yu, S.-H., *ACS Nano* **2018**, 12, 5856.

(32) Asl, H. Y.; Fu, J.; Kumar, H.; Welborn, S. S.; Shenoy, V. B.; Detsi, E., *Chem. Mater*. **2018**, 30, 1815.

(33) Tran, T. T.; Lamanna, W. M.; Obrovac, M. N., *J. Electrochem. Soc.* **2012**, 159, A2005.

(34) Martin-Gonzalez, M.; Prieto, A. L.; Knox, M. S.; Gronsky, R.; Sands, T.; Stacy, A. M., *Chem. Mater.* **2003**, 15, 1676.

(35) Nakanishi, K.; Kato, D.; Arai, H.; Tanida, H.; Mori, T.; Orikasa, Y.; Uchimoto, Y.; Ohta, T.; Ogumi, Z., *Review of Scientific Instruments* **2014**, 85, 084103.

(36) Brouillette, D.; Irish, D. E.; Taylor, N. J.; Perron, G. R.; Odziemkowski, M.; Desnoyers, J. E., *Phys. Chem. Chem. Phys.* **2002**, 4, 6063.

(37) Seo, D. M.; Borodin, O.; Han, S. D.; Boyle, P. D.; Henderson, W. A., *J. Electrochem. Soc.* **2012**, 159, A1489.

(38) Yamada, Y.; Furukawa, K.; Sodeyama, K.; Kikuchi, K.; Yaegashi, M.; Tateyama, Y.; Yamada, A., *J. Am. Chem. Soc.* **2014**, 136, 5039.

(39) Zhang, C.; Ueno, K.; Yamazaki, A.; Yoshida, K.; Moon, H.; Mandai, T.; Umebayashi, Y.; Dokko, K.; Watanabe, M., *J. Phys. Chem. B* **2014**, 118, 5144.

(40) Veryasov, G.; Matsumoto, K.; Hagiwara, R., *Dalton Trans.* **2016**, 45, 2810.

(41) Ojha, A. K.; Srivastava, S. K.; Peica, N.; Schlücker, S.; Kiefer, W.; Asthana, B. P., *J. Mol. Struct.* **2005**, 735.

(42) Benevenuto, R. L.; Alves, W. A., *J. Raman Spectrosc.* **2008**, 39, 490.

(43) Alves, C. C.; Campos, T. B. C.; Alves, W. A., *Spectrochim. Acta, Part A* **2012**, 97, 1085.

(44) Coles, S. W.; Mishin, M.; Perkin, S.; Fedorov, M. V.; Ivanistsev, V. B., *Phys. Chem. Chem. Phys.* **2017**, 19, 11004.

(45) Rajput, N. N.; Qu, X.; Sa, N.; Burrell, A. K.; Persson, K. A., *J. Am. Chem. Soc.* **2015**, 137, 3411.

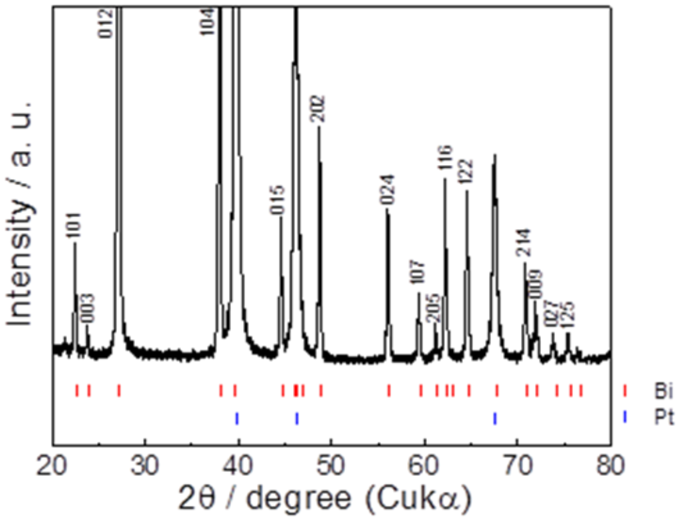

Figure 3-1. XRD patterns of bismuth anode electrodeposited on Pt substrate.

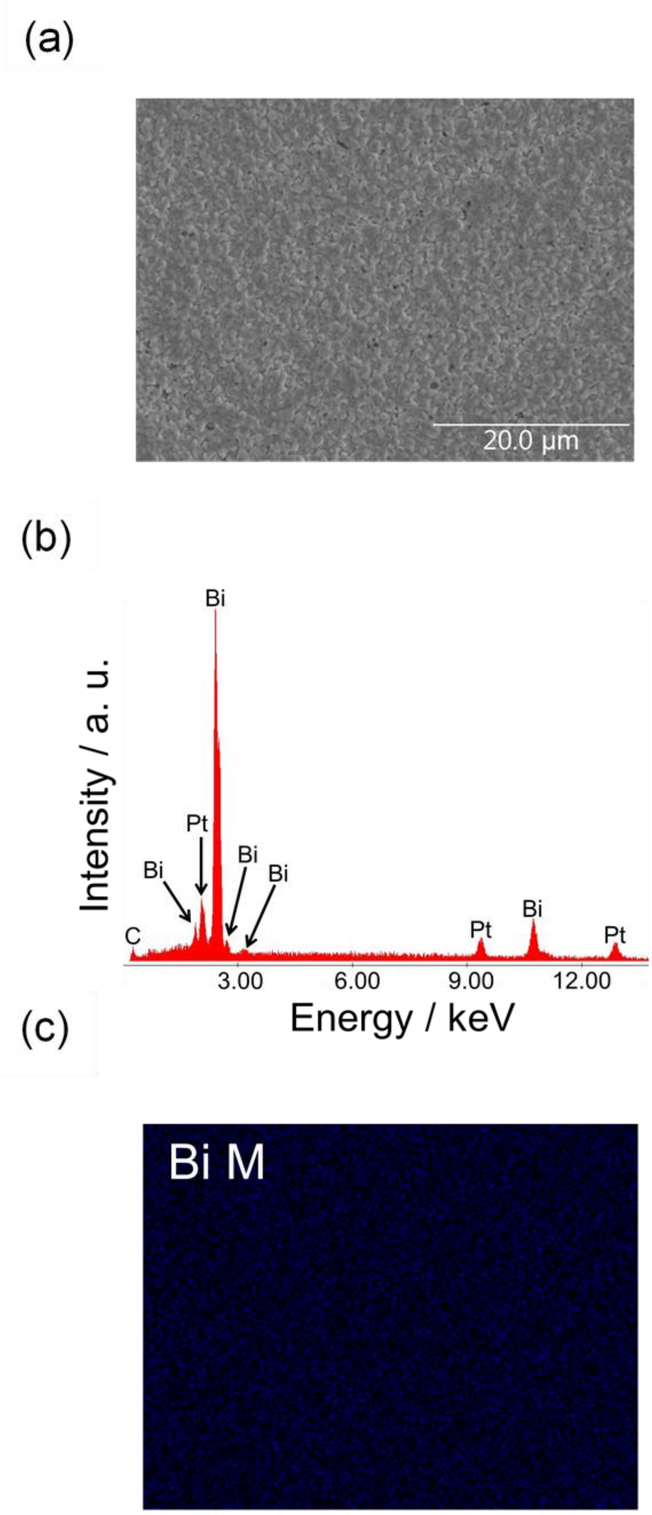

Figure 3-2. (a) SEM image, (b) EDX spectrum and (c) EDX mapping of Bi M for electrodeposited bismuth on Pt substrate.

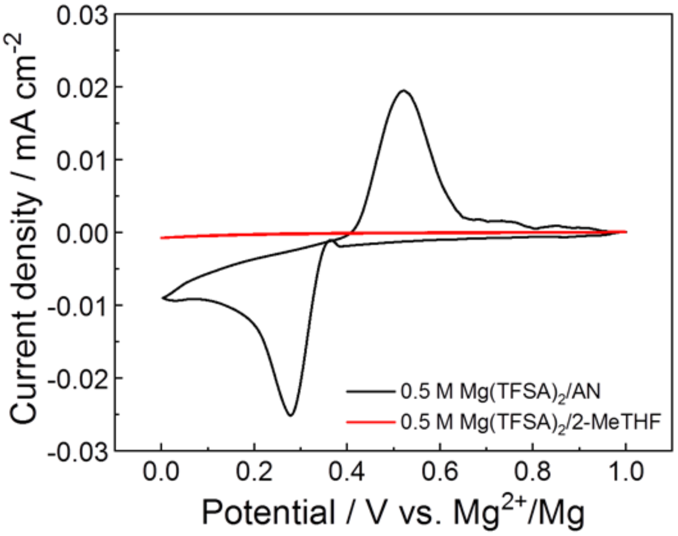

Figure 3-3. Cyclic voltammograms of bismuth electrode in 0.5 M Mg(TFSA)$_2$/AN and 0.5 M Mg(TFSA)$_2$/2-MeTHF at a scanning rate of 0.1 mV/sec.

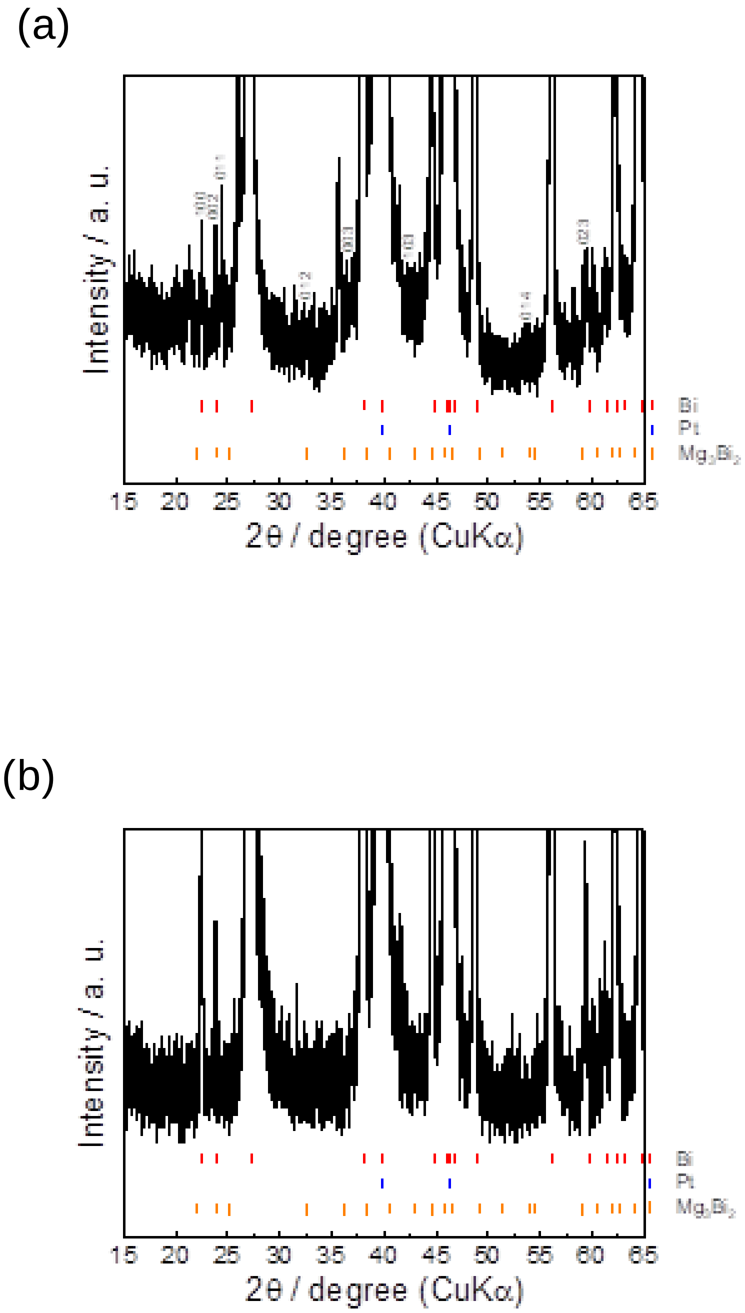

Figure 3-4. XRD patterns of bismuth anode in (a) 0.5 M $Mg(TFSA)_2$/AN (a) and (b) 0.5 M $Mg(TFSA)_2$/2-MeTHF after electrochemical measurements.

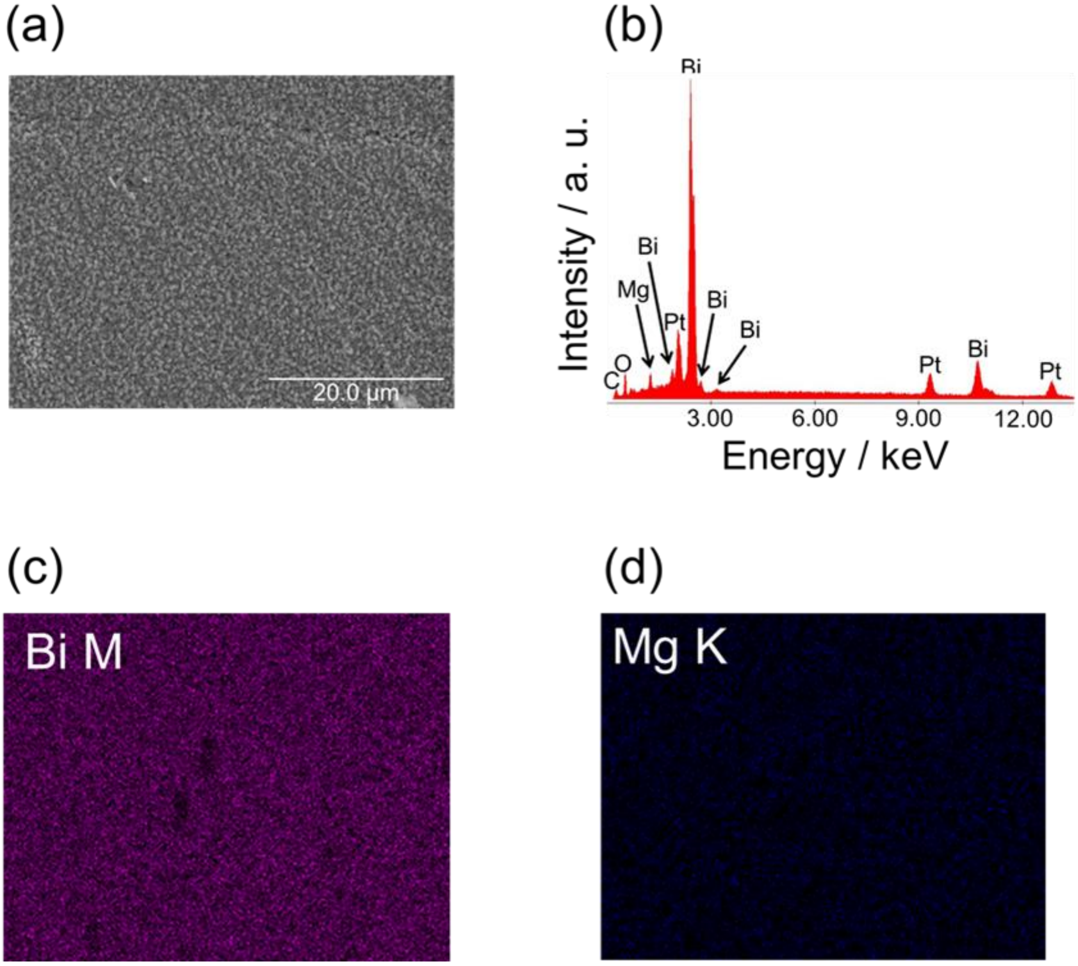

Figure 3-5. (a) SEM image, (b) EDX spectrum, (c) EDX mapping of Bi M and (d) EDX mapping of Mg K for electrodeposited bismuth on Pt substrate after electrochemical measurements in 0.5 M $Mg(TFSA)_2$/AN.

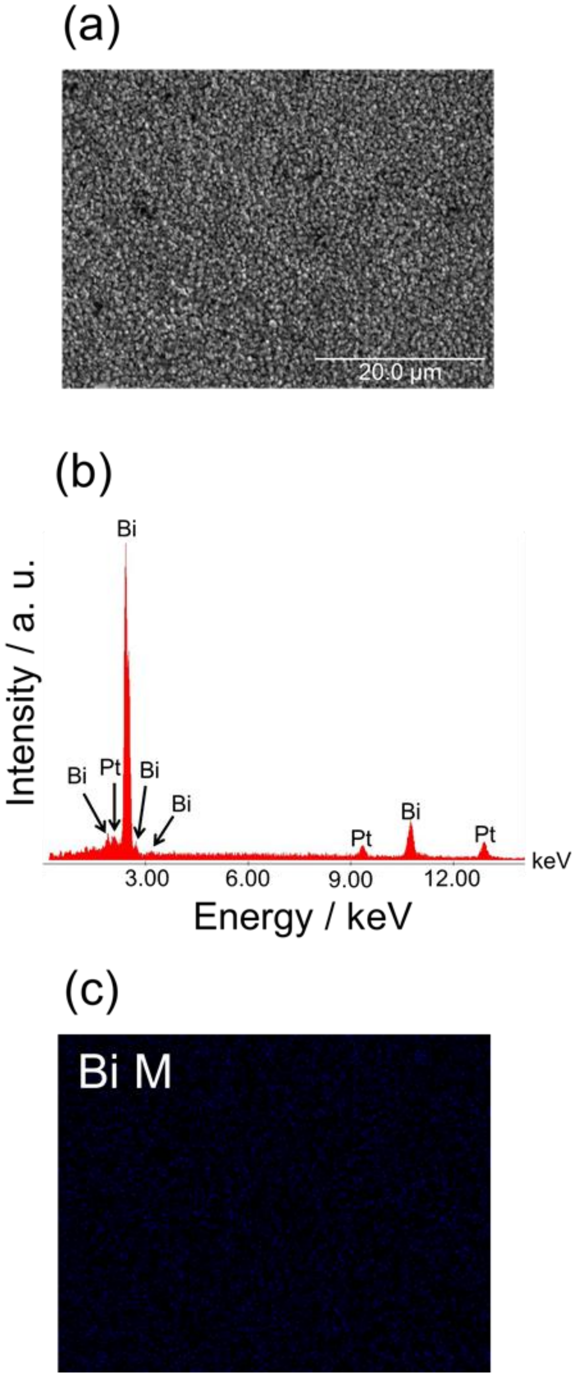

Figure 3-6. (a) SEM image, (b) EDX spectrum and (c) EDX mapping of Bi M for electrodeposited bismuth on Pt substrate after electrochemical measurement in 0.5 M Mg(TFSA)$_2$/2-MeTHF.

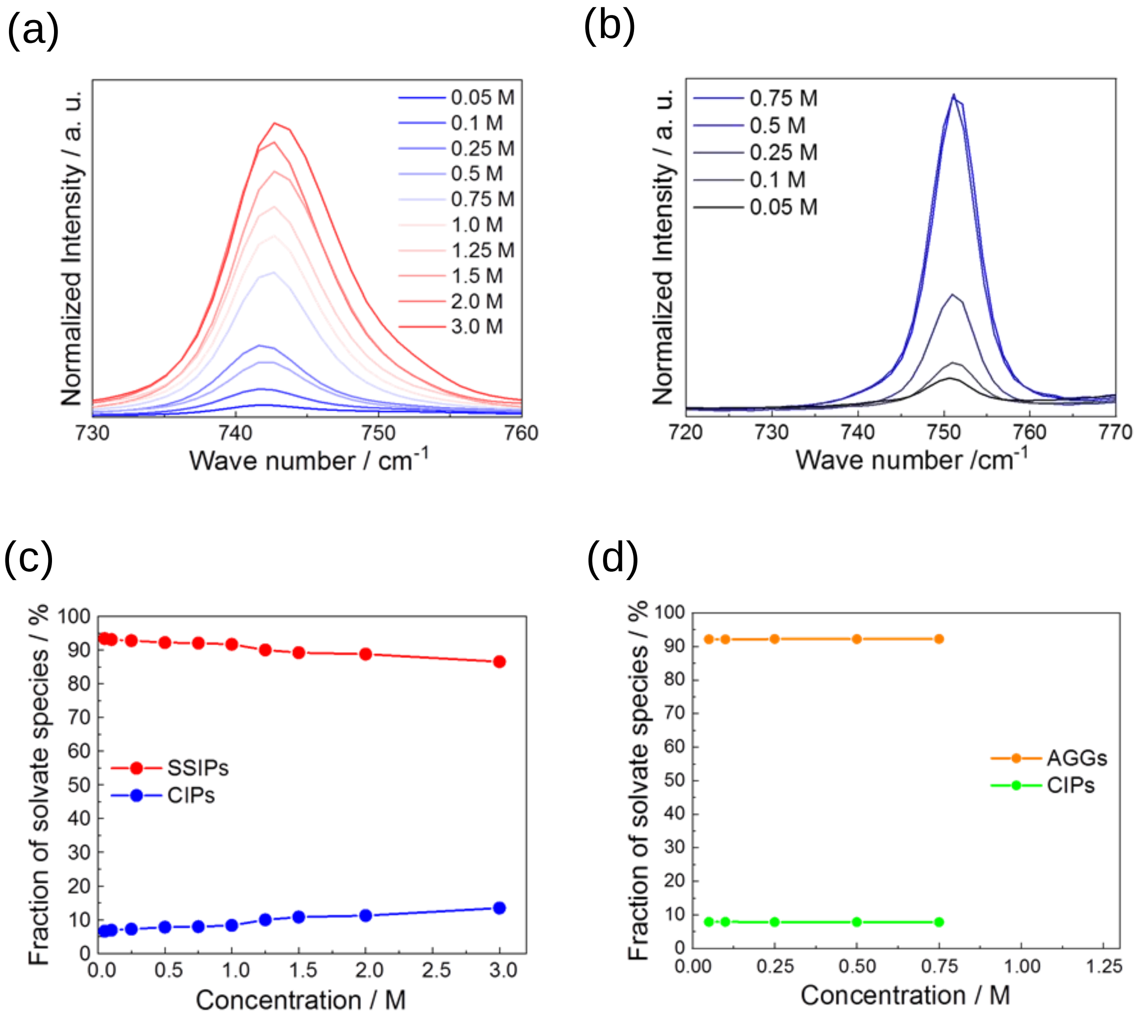

Figure 3-7. Raman spectra of (a) Mg(TFSA)$_2$/AN in several concentration in the region between 730 and 760 cm^{-1}. (b) Fraction of solvate species of (c) Mg(TFSA)$_2$/ AN and of (d) Mg(TFSA)$_2$/2-MeTHF in several concentration. SSIPs : solvent-separated ion pairs. CIPs : contact ion pairs. AGGs : aggregate coordinations.

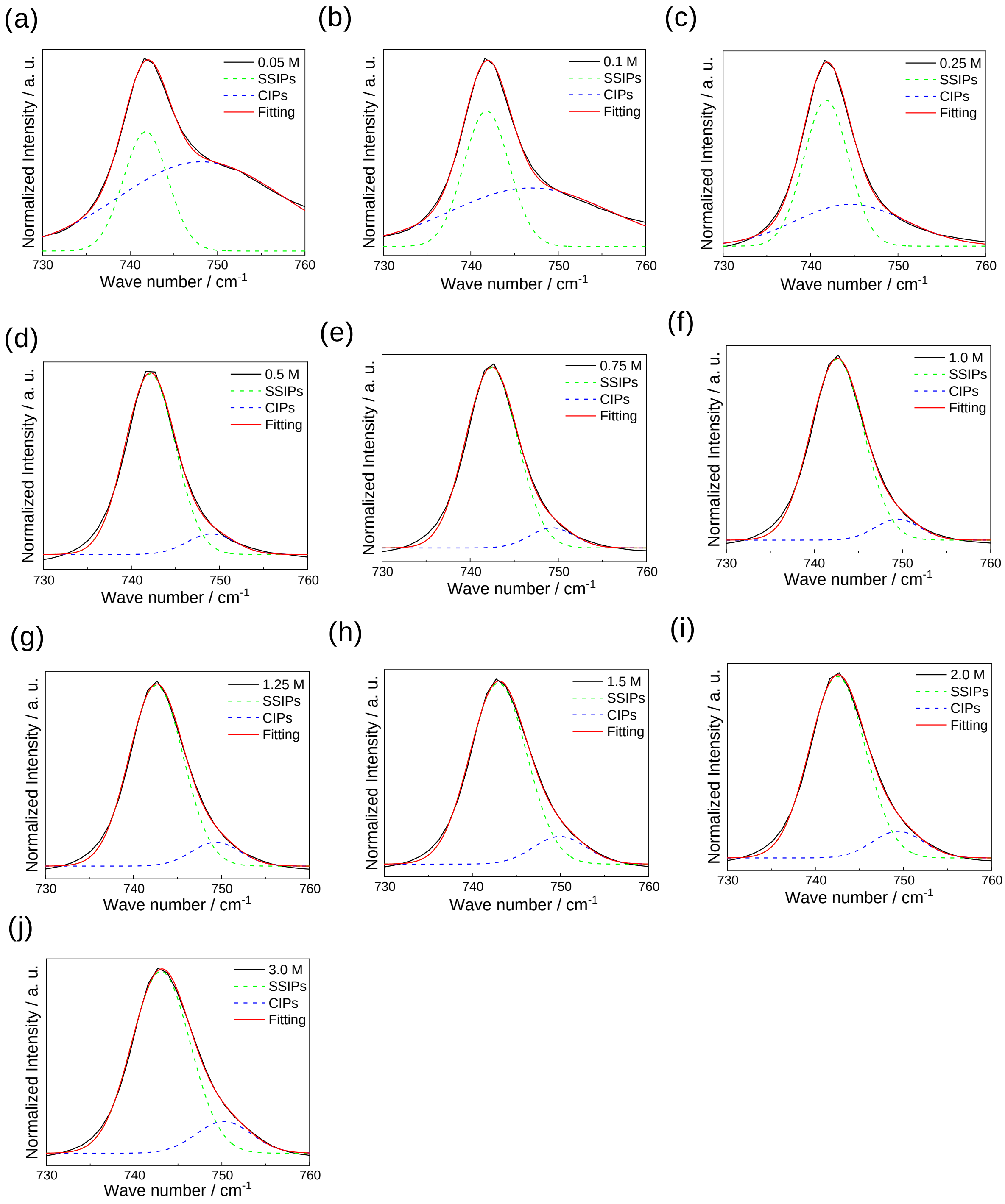

Figure 3-8. Raman spectra and Gaussian fitting results of Mg(TFSA)$_2$/AN in several concentration in the region between 730 and 760 cm^{-1}.

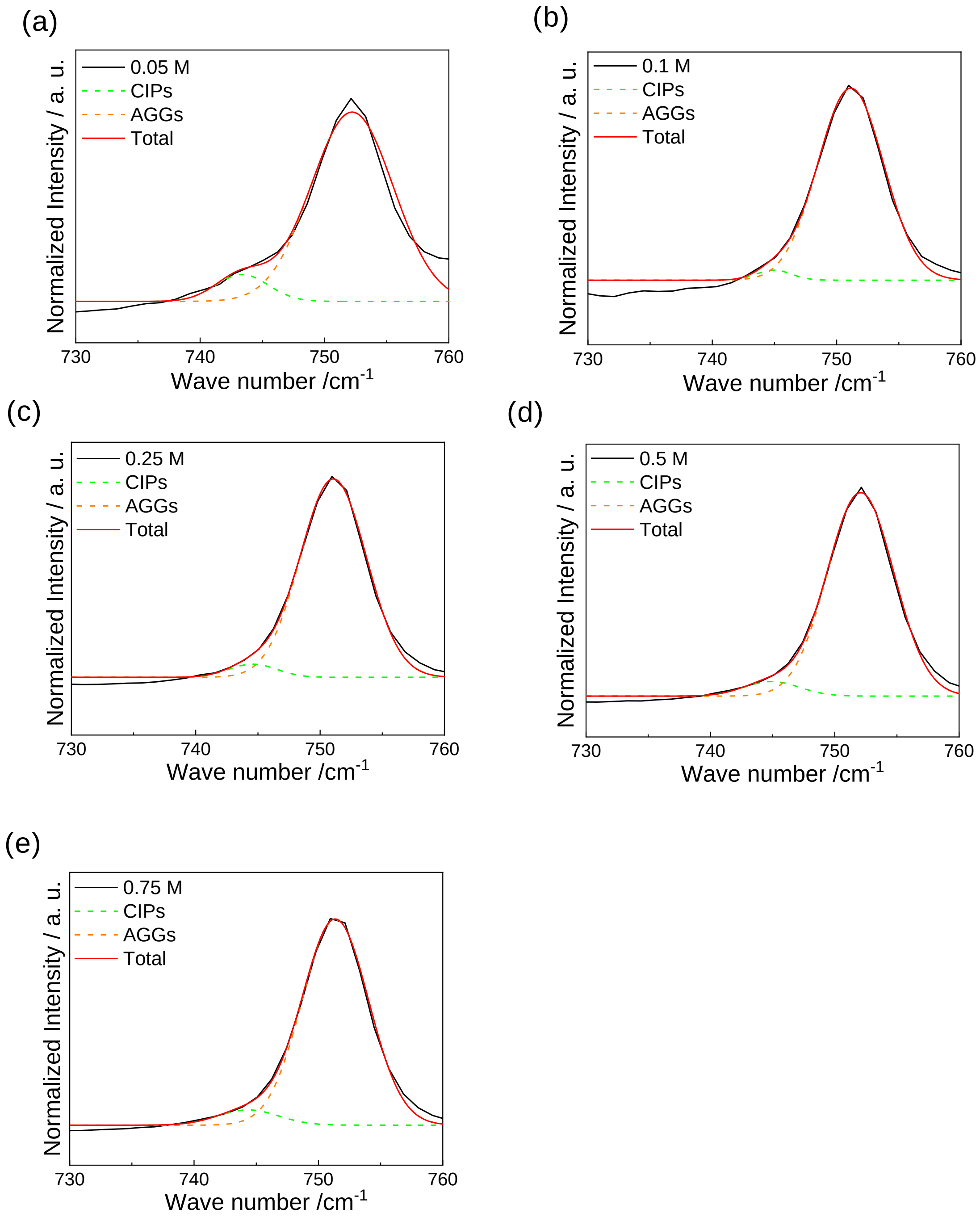

Figure 3-9. Raman spectra and Gaussian fitting results of $Mg(TFSA)_2$/2-MeTHF in several concentration in the wave number between 720 and 760 cm^{-1}.

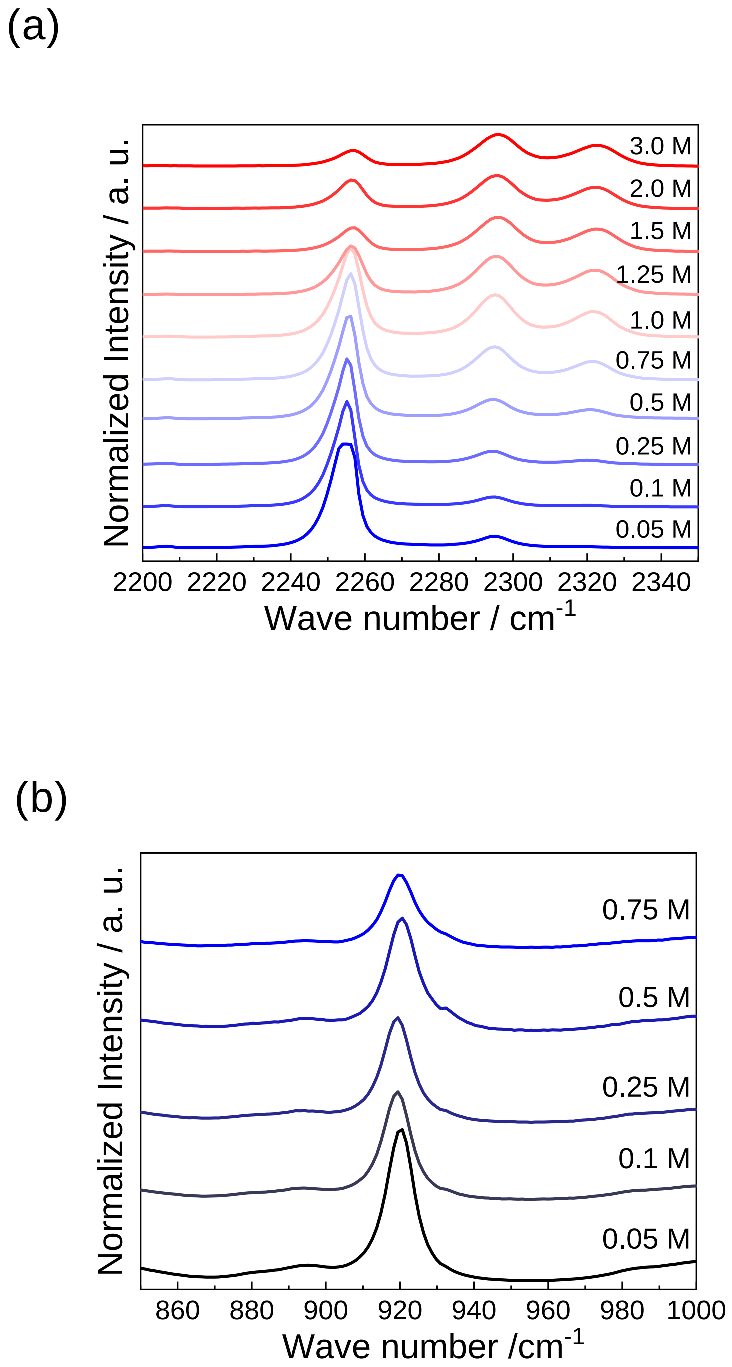

Figure 3-10. Raman spectra of Mg(TFSA)$_2$/AN in several concentration in the region between 2200 and 2310 cm^{-1}.

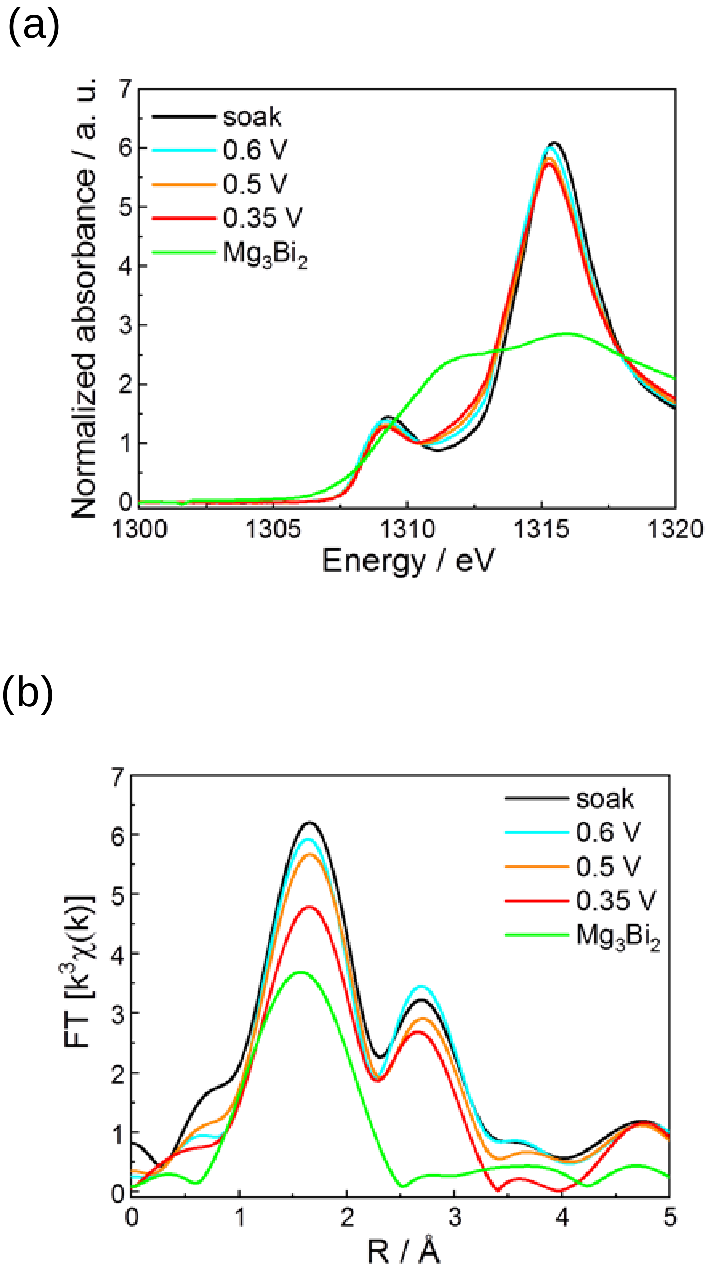

Figure 3-11. Mg *K*-edge (a) XANES and Fourier-transformed EXAFS spectra obtained from *operando* XAS measurements 0.5 M $Mg(TFSA)_2$/AN. The potential is expressed on vs. Mg^{2+}/Mg.

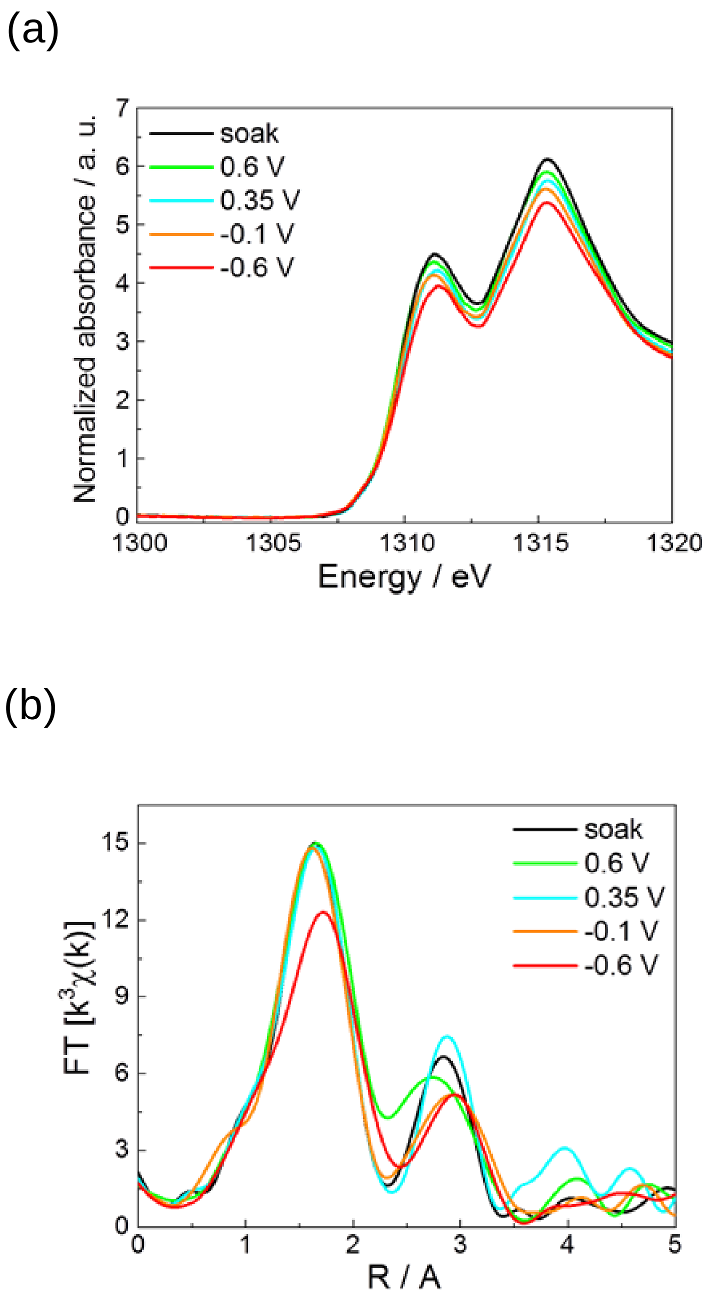

Figure 3-12. Mg *K*-edge (a) XANES and Fourier-transformed EXAFS spectra obtained from *operando* XAS measurements 0.5 M Mg(TFSA)$_2$/2-MeTHF. The potential is expressed on vs. Mg^{2+}/Mg.

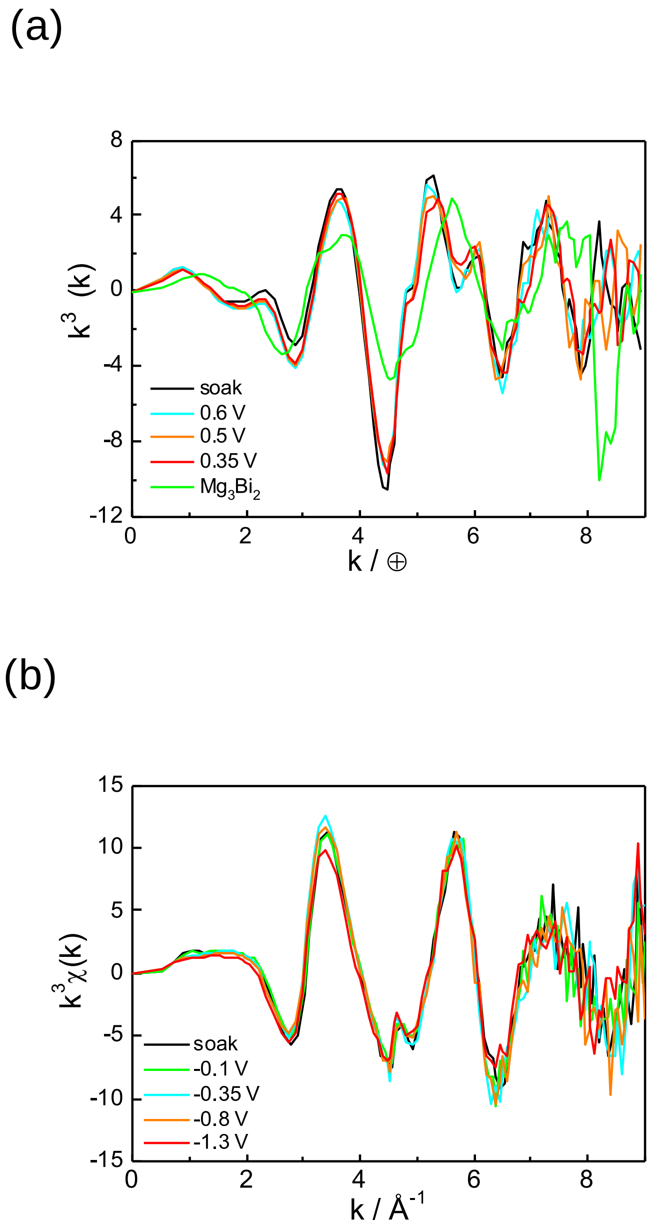

Figure 3-13. The EXAFS oscillations for (a) 0.5 M Mg(TFSA)$_2$/AN and (b) 0.5 M Mg(TFSA)$_2$/2-MeTHF at several voltages

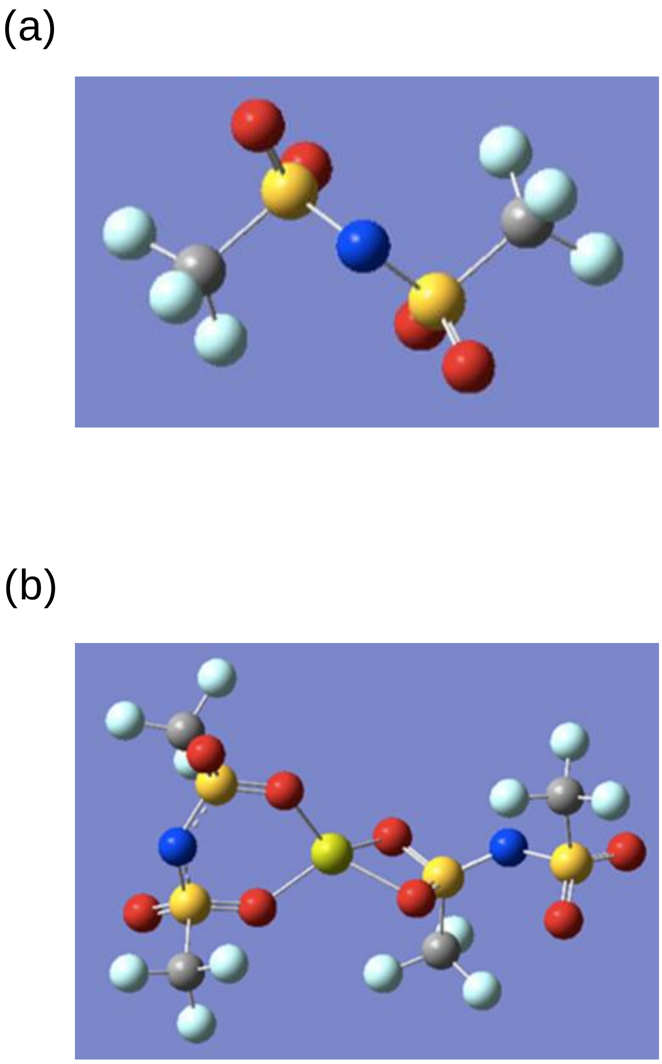

Figure 3-14. The most stable structure of (a) TFSA in AN and/or 2-MeTHF (b) Mg(TFSA)$_2$ in AN and/or 2-MeTHF calculated by first principle calculation. Green : Mg, Red : O, Grey : C, Blue : N, Yellow : S, Light blue : F.

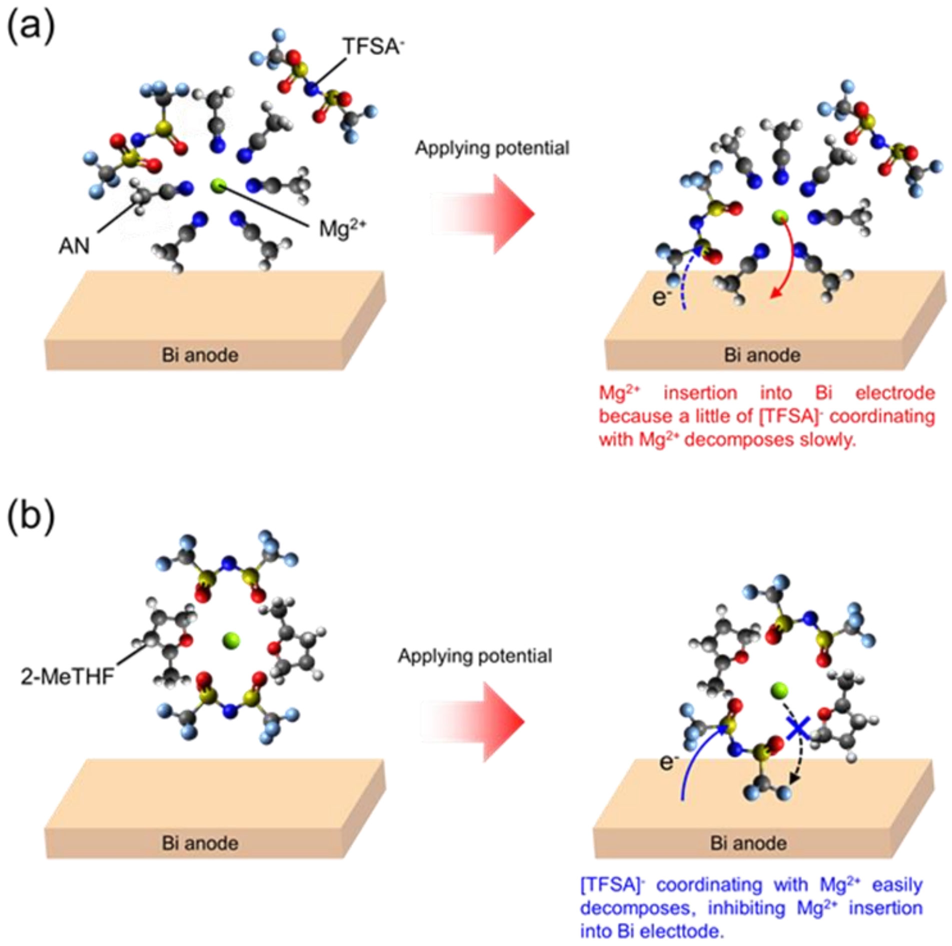

Mg^{2+} insertion into Bi electrode because a little of $[TFSA]^-$ coordinating with Mg^{2+} decomposes slowly.

$[TFSA]^-$ coordinating with Mg^{2+} easily decomposes, inhibiting Mg^{2+} insertion into Bi electtode.

Figure 3-15. Schematic illustrations of the reaction mechanism of magnesium ion alloying to bismuth electrode in the (a) 0.5 M $Mg(TFSA)_2$/AN and (b) 0.5 M $Mg(TFSA)_2$/2-MeTHF. The left part is under soak situation, and right part is under applying voltage.

Chapter 4: Elucidation of the Magnesium Metal Deposition Using BH_4 Anion

4.1 Introduction

Magnesium rechargeable batteries using magnesium metal as negative electrode are candidate for next generation batteries system.[1,2] The magnesium metal has a high theoretical volumetric capacity (3832 mAh/cm^3) and relatively low reduction potential (-2.38 V vs. SHE), producing high energy density. Moreover, the safety and cost of magnesium metal are superior to those of lithium metal.[3-5] These favorable properties of magnesium metal make magnesium rechargeable batteries attractive. However, magnesium rechargeable batteries have many challenges for practical application. One major problem is difficulty of reversible magnesium deposition/dissolution reactions in electrolyte. The electrolyte containing inorganic salt and carbonate solvent, which is normally used for lithium ion batteries, cannot be used for the magnesium metal deposition because passivation film formed on the anode surface inhibits pass of magnesium ions.[6]

Grignard reagent based electrolytes have been studied for the electrolytes, which can realize reversible magnesium metal deposition/dissolution reactions.[7-12] However, these electrolytes have the problems of narrow electrochemical potential window and corrosion reaction because of the halide contained in the electrolytes. Resolving the problems that the Grignard reagent based electrolytes have, many researchers have developed the new halide-free electrolytes that consists of inorganic magnesium salts and ethereal solvents and that realizes reversible magnesium metal deposition/dissolution reaction.[13-21] Among these electrolytes, magnesium borohydride ($Mg(BH_4)_2$) based electrolytes, which has been firstly reported Mohtadi *et al.*,[14] are attractive electrolytes because of high coulombic efficiency for magnesium deposition/dissolution reactions, and thus have been studied by several research groups.[14,16,22] Mohtadi and other groups have suggested that $Mg(BH_4)_2$/ether electrolytes have contact ion pair $Mg[(\mu\text{-}H)_2BH_2]_2$ based on the results of several spectroscopy techniques.[14,16] Rajput *et al.* has reported that ion pair between magnesium ions and BH_4^- does not undergo decomposition reaction during magnesium metal deposition by theoretical calculation.[23] Several groups have reported that the magnesium deposition/dissolution reactions are improved by changing the solvents or adding lithium borohydride in $Mg(BH_4)_2$/ether electrolytes.[14,16,24-26]

However, the reaction mechanism of magnesium metal deposition/dissolution reactions in $Mg(BH_4)_2$ based electrolytes has not been clearly understood because the knowledge about interfacial behavior of magnesium ion between negative electrode and electrolyte during magnesium deposition reaction is insufficient. Recently, a new X-ray absorption spectroscopy technique under magnesium deposition process (*operando* XAS) has been developed and applied to examine the interfacial behavior of magnesium electrolytes.[25] XAS is a powerful technique to examine electronic and local structure for magnesium electrolyte.[27,28] Arthur *et al.* examined the interfacial structure between negative electrode and $Mg(BH_4)_2$/ether electrolyte using *operando* XAS and suggested that solid electrolyte interphase formed, which can pass magnesium ions, on the negative electrode surface after magnesium deposition reaction.[25] However, coordination state of magnesium ions in $Mg(BH_4)_2$ based electrolyte before magnesium deposition reaction occurs, has not been examined. In this study, we examined the coordination structure of magnesium ions in $Mg(BH_4)_2$/ether electrolytes during magnesium metal deposition reaction using *operando* soft X-ray absorption spectroscopy combined with Raman spectroscopy. We observed that BH_4^- desorbs from magnesium ions because of the weak interaction between BH_4^- of soft base and magnesium ion of hard acid, enabling magnesium deposition reaction.

4.2 Experimental

4.2.1. Material preparation

0.5 M magnesium borohydride ($Mg(BH_4)_2$) /tetrahydrofuran (THF) or 0.1 M $Mg(BH_4)_2$/ethylene glycol dimethyl ether (glyme) electrolyte were prepared by stirring $Mg(BH_4)_2$ (Sigma-Aldrich, 95%) with THF (Wako Pure Chemical Industries, Ltd., >99.5%) or glyme (KISHIDA CHEMICAL Co., Ltd., 99.5%) in an argon-filled glove box overnight at room temperature. The solvent was dried by using molecular sieves 3A for 48 hours to decrease the water content before use. After drying, the water content of the prepared electrolytes was less than 30 ppm, which were confirmed by Karl Fischer titration.

4.2.2. Electrochemical measurements

A three-electrode cell was used for cyclic voltammetry. The working electrode was a platinum plate. The counter and the reference electrodes were magnesium rods, which were polished in an argon-filled globe box before assembling cells. Cyclic voltammetry was carried out at 25°C with a sweeping potential rate of 20 mV/sec. The potential range was -2.0 V - 2.0 V (vs. Mg^{2+}/Mg).

4.2.3. XRD measurements

X-ray diffraction was performed by Ultima IV (Rigaku Co., Inc.) with X-ray source of CuKα. Scanning electron microscopy (SEM) images operated at a potential of 15 kV and energy dispersive X-ray spectroscopy (EDX) spectra at electron energy of 25 keV were collected by S-3400 N (Hitachi High-Tech Co.) . After potentiostatic deposition of magnesium metal, the electrochemical measured cells were disassembled, then the obtained electrodes were washed with THF, glyme, respectively. These electrodes were dried in an argon-filled glove box overnight at room temperature. All measurements were conducted without air exposure of the samples.

4.2.4. Raman spectroscopy

The Raman spectra of the magnesium electrolytes were measured by MultiRAM (Bruker Optics Co., Ltd.) equipped with Nd-YAG laser (1064 nm) at room temperature. The measurement range was between 70 and 3600 cm^{-1}. The electrolytes were set into glass vessels and sealed in them in an argon-filled glove box, and measured without air exposure.

4.2.5. Soft X-ray absorption spectroscopy

operando XAS spectra of the electrolytes in the energy region of Mg *K*-edge were collected by partial fluorescence yield method at the beam line of the SPring-8 synchrotron radiation facility (BL27SU) in Hyogo, Japan. A custom made three-electrode cell was used for the *operando* XAS measurements. Chromium layer with the thickness of 5 nm was pre-deposited as a buffer on silicon nitride (Si_3N_4) window with 300 nm thickness (Norcada Inc.), and then platinum layer with the thickness of 30 nm was deposited on the Cr/Si_3N_4 window by using magnetron sputtering on the respectively. The prepared $Pt/Cr/Si_3N_4$ window was employed as a working electrode. Counter and reference electrodes were polished magnesium plate. The *operando* cell was assembled in an argon-filled glove box and transferred into a vacuum chamber for the XAS measurements without air exposure. *operando* XAS measurements were performed under keeping the potentials after decreasing the potential of the working electrode at several different potentials before magnesium metal deposition reaction does not start. Then, magnesium metal was deposited on the working electrode by applying potential step method, and additional XAS measurements were conducted. The analysis of the obtained XAS spectra was performed using ATHENA program.[29]

4.3 Results and Discussion

4.3.1 Cyclic Voltammetry and Characterizations after electrochemical measurements

Magnesium deposition and dissolution reactions were examined for the 0.5 M $Mg(BH_4)_2$/THF and 0.1 M $Mg(BH_4)_2$/glyme by cyclic voltammetry. Figure 4-1. (a) shows the obtained voltammograms. In the both electrolytes, cathodic and anodic currents, which are attributed to magnesium metal deposition and dissolution reactions, were observed. XRD and SEM-EDX confirmed that the deposited product after the cathodic current occurred in the both electrolytes was magnesium metal (Supporting Figure 4-2., 4-3. and 4-4.). The coulombic efficiency was 38 % and 32 % in the 0.5 M $Mg(BH_4)_2$/THF and 0.1 M $Mg(BH_4)_2$/glyme, respectively. The current values of the magnesium deposition and dissolution reactions in the 0.1 M $Mg(BH_4)_2$/glyme were larger than those in the 0.5 M $Mg(BH_4)_2$/THF. Also, the overpotential of magnesium metal deposition reaction of 0.1 M $Mg(BH_4)_2$/glyme is smaller than that of 0.5 M $Mg(BH_4)_2$/THF as shown in Figure 4-1 (b). These results correspond to previous report.[14]

4.3.2 Coordination structure using Raman spectroscopy

The coordination state of anion in $Mg(BH_4)_2$/THF and $Mg(BH_4)_2$/glyme was examined by Raman spectroscopy. Figure 4-5. (a) and (b) show the Raman spectra ranging from 2000 to 2500 cm^{-1} in $Mg(BH_4)_2$/THF and $Mg(BH_4)_2$/glyme for various concentrations, respectively. The spectra in wide region were shown in Figure 4-6. and 4-7. The peak appearing between 2100 and 2500 cm^{-1} is attributed to B-H stretching vibration of BH_4 coordinated to cation.[30-36] For $Mg(BH_4)_2$/THF, peaks were observed at 2200 and 2380 cm^{-1} in 0.1 M $Mg(BH_4)_2$/THF, additional peaks appeared at 2140 cm^{-1} and 2300 cm^{-1} with increase of the concentration. The peaks at 2200 cm^{-1} and 2380 cm^{-1} were assigned to bridging $B\text{-}H_b$ vibration and $B\text{-}H_t$ vibration, respectively. The $Mg(BH_4)_2$ crystal that has $P6_1$ of space group, shows a $B\text{-}H_b$ vibration at 2300 cm^{-1}.[34] Mohtadi *et al.* proposed that $Mg(BH_4)_2$ in $Mg(BH_4)_2$/THF solution is present as the contact ion pair $[Mg\{(\mu\text{-}H)_2BH_2\}]_2$, which partially dissociates into $[Mg\{(\mu\text{-}H)_2BH_2\}]^+$ and BH_4^- as in the following equation;[14]

$$[Mg\{(\mu\text{-}H)_2BH_2\}]_2 \rightleftarrows [Mg\{(\mu\text{-}H)_2BH_2\}]^+ + BH_4^-$$

From these previous reports, we assigned the peak at 2300 cm^{-1} is attributed to B-H vibration of BH_4^- in Mg^{2+} coordinated to multi BH_4^-. The peak at 2140 cm^{-1} also may be attributed to B-H vibration of BH_4^- in Mg^{2+} coordinated to multi BH_4^-. On the other hand, for $Mg(BH_4)_2$/glyme, a peak was observed at 2310 cm^{-1} with 0.02 M $Mg(BH_4)_2$/glyme, the peak intensity decreased and additional peaks appeared at 2200 cm^{-1} and 2380 cm^{-1} with increase of the concentration. The peaks at 2200 cm^{-1} and 2380 cm^{-1} were assigned to bridging $B\text{-}H_b$ vibration and $B\text{-}H_t$ vibration, respectively. We assigned that the peak at 2310 cm^{-1} to be B-H vibration of non-coordinating BH_4^- (free BH_4^-) because the intensity is larger with decrease of the concentration. Although the dielectric constant of glyme (7.2) is slightly lower than that of THF (7.4),[36] glyme wraps Mg^{2+} by two oxygen sites in the molecule, weakening the interaction Mg^{2+} and BH_4^-.[14,37] Watkins *et al.* also reported that the similar tendency appeared in ionic liquid system containing polyethylene glycol chains.[24] Therefore, free BH_4^- exists in the 0.1 M $Mg(BH_4)_2$/glyme due to the weak interaction unlike in the 0.5 M $Mg(BH_4)_2$/THF.

4.3.3 *operando* soft X-ray absorption spectroscopy.

In order to examine the electronic and local structure of Mg^{2+} from cation side under applying volltage in the 0.5 M $Mg(BH_4)_2$/THF and 0.1 M $Mg(BH_4)_2$/glyme, we conducted *operando* XAS measurements. Figure 4-8. and 4-9. show Mg *K*-edge XANES and Fourier-transformed EXAFS spectra of Mg *K*-edge at several potentials for 0.5 M $Mg(BH_4)_2$/THF and 0.1 M $Mg(BH_4)_2$/glyme, respectively. The cyclic voltammograms of each electrolyte using the *operando* cells were shown in Figure 4-10. For 0.5 M $Mg(BH_4)_2$/THF, the peak intensity of XANES (Figure 4-8. (a)) gradually decreased from the soak state to -0.5 V, which is the potential slightly before magnesium metal deposition reaction starts (Figure 4-10. (a)), hen the XANES drastically changed after magnesium metal deposition reaction. These results mean electronic structure of magnesium ions, which is influenced by the coordination state of magnesium ions, changed during magnesium deposition process. In the EXAFS spectra (Figure 4-8. (b)), a peak was observed at 1.54 Å. Although Mg^{2+} coordinates with THF and BH_4^- from results of Raman spectroscopy, the Mg-H bond should not be detected by EXAFS analysis because the back scattering of hydrogen is the smallest of all the elements. Therefore, we assigned the peak to Mg-O bond between Mg^{2+} and THF. The intensity of the peak in the EXAFS spectrum decreased from the soak state to -0.5 V, meaning that the coordination number decreased and/or local distortion increased of magnesium ions. Then, the EXAFS spectra changed after magnesium metal deposition reaction and the peak that is attributed to Mg-Mg bond of magnesium metal appeared at 2.69 Å.

For 0.1 M $Mg(BH_4)_2$/glyme, the peak intensity of XANES (Figure 4-9. (a)) gradually decreased from the soak state to -0.5 V, which is the potential before magnesium metal deposition reaction starts (Figure 4-10. (b)). The decreasing degree of the intensity in the 0.1 M $Mg(BH_4)_2$/glyme was larger than that of the intensity in the 0.5 M $Mg(BH)_2$/THF. These results means that coordination state of magnesium ions changed more largely in the 0.1 M $Mg(BH_4)_2$/glyme than that of magnesium ions in the 0.5 M $Mg(BH)_2$/THF. In the EXAFS spectra (Figure 4-9. (b)), a peak was observed at 1.59 Å. In the 0.1 M $Mg(BH_4)_2$/glyme, although Mg^{2+} coordinates with glyme and BH_4^-, the peak was assigned to Mg-O bond between Mg^{2+} and glyme. However, the Mg-H bond should not be detected by EXAFS analysis, because Mg-H bond between Mg^{2+} and BH_4^- should not be detected due to the small scattering of hydrogen. The peak gradually decreased under applying potential before magnesium metal deposition reaction starts. After magnesium metal deposition reaction occurs, the EXAFS spectra drastically changed and the peak that is attributed to Mg-Mg bond of magnesium metal appeared at 2.76 Å.

4.3.4 Discussion

Magnesium deposition reaction occurs in the both electrolytes, the ligands should desorb from magnesium ions during the deposition process. Based on the results from *operando* XAS measurements, we discuss the correlation between the electrochemical property and the coordination structure of magnesium ions during magnesium deposition process.

For the 0.5 M $Mg(BH_4)_2$/THF, all of the BH_4^- coordinates with magnesium ions. EXAFS spectra change indicates that desolvation of THF from magnesium ion, and XANES change indicates that desorption of THF as well as BH_4^-. Hence, magnesium deposition can occur because THF and BH_4^- can desorb from magnesium ion under applying negative potential as shown in Figure 4-11. (a). For the 0.1 M $Mg(BH_4)_2$/glyme, the free BH_4^- exists in the solution. EXAFS spectra change indicates desolvation of glyme from magnesium ion. Although the change degree of the EXAFS spectra in the 0.1 M $Mg(BH_4)_2$/glyme is similar to that of the EXAFS spectra in the 0.5 M $Mg(BH_4)_2$/THF, the change degree of XANES is larger than that of 0.1 M $Mg(BH_4)_2$/glyme. These mean that BH_4^- coordinating with magnesium ion of the 0.1 M $Mg(BH_4)_2$/glyme desorbs more easily than that of the 0.5 M $Mg(BH_4)_2$/THF. This easy desorption of BH_4^- is favorable for magnesium deposition, leading to the larger cathodic currents shown in Figure 4-11. (b). Several group have reported that the increase of dissociation between BH_4^- and magnesium ion is favorable for magnesium deposition.[14,24] Our group also found that in $Mg(TFSA)_2$/ether electrolyte solution, $TFSA^-$ coordinating with magnesium ions blocks magnesium deposition reaction.[38] However, BH_4^- coordinating with magnesium ions does not block the reaction in the $Mg(BH_4)_2$/ether electrolyte. BH_4^- is softer base than $TFSA^-$ and coordinates more weakly with magnesium ion, which is hard acid.[39-41] Therefore, BH_4^- can desorbs from magnesium ions dislike $TFSA^-$ during magnesium deposition process. The degree of base in anion, which influences the interaction between magnesium ion and anion, is an important factor to design the electrolyte enabling reversible magnesium deposition/dissolution reactions.

4.4 Conclusions

We examined the coordination state of magnesium ions in $Mg(BH_4)_2$/THF and $Mg(BH_4)_2$/glyme during magnesium deposition reaction using *operando* XAS technique. BH_4^- coordinates with magnesium ions in the both electrolytes and it desorbs from magnesium ions during magnesium deposition process. However, BH_4^- in the $Mg(BH_4)_2$/glyme desorbs from magnesium ions more easily than BH_4^- in the $Mg(BH_4)_2$/THF, which leads to larger current in the $Mg(BH_4)_2$/glyme. Weakening the interaction between magnesium ions and anion is important to realize reversible magnesium deposition/dissolution reactions.

References

(1) Armand, M.; Tarascon, J. M., *Nature* **2008**, 451, 652.

(2) Yoo, H. D.; Shterenberg, I.; Gofer, Y.; Gershinsky, G.; Pour, N.; Aurbach, D., *Energy Environ. Sci.* **2013**, 6, 2265.

(3) Gregory, T. D.; Hoffman, R. J.; Winterton, R. C., *J. Electrochem. Soc.* **1990**, 137, 775.

(4) Novák, P.; Imhof, R.; Haas, O., *Electrochim. Acta* **1999**, 45, 351–367.

(5) Besenhard, J. O.; Winter, M., *ChemPhysChem* **2002**, 3, 155

(6) Lu, Z.; Schechter, A.; Moshkovich, M.; Aurbach, D., *J. Electroanal. Chem.* **1999**, 466, 203.

(7) Aurbach, D.; Lu, Z.; Schechter, A.; Gofer, Y.; Gizbar, H; Turgeman, R.;Cohen, Y.; Moshkovich, M.; Levi, E., *Nature* **2000**, 407, 724.

(8) Aurbach, D.; Schechter, A.; Moshkovich, M.; Cohen, Y., *J. Electrochem. Soc.* **2001**, 148, A1004.

(9) Aurbach, D.; Gizbar, H.; Schechter, A.; Chusid, O.; Gottlieb, H. E.; Gofer, Y.; Goldberg, I., *J. Electrochem. Soc.* **2002**, 149, A115.

(10) Mizrahi, O.; Amir, N.; Pollak, E.; Chusid, O.; Marks, V.; Gottlieb, H.; Larush, L.; Zinigrad, E.; Aurbach, D., *J. Electrochem. Soc.* **2008**, 155, A103.

(11) Pour, N.; Gofer, Y.; Major, D. T.; Aurbach, D., *J. Am. Chem. Soc.* **2011**, 133, 6270.

(12) Kim, H. S.; Arthur, T. S.; Allred, G. D.; Zajicek, J.; Newman, J. G.;

Rodnyansky, A. E.; Oliver, A. G.; Boggess, W. C.; Muldoon, J., *Nat. Commun.* **2011**, 2, 427.

(13) Barile, C. J.; Spatney, R.; Zavadil, K. R.; Gewirth, A. A., *J. Phys. Chem. C* **2014**, 118, 10694.

(14) Mohtadi, R.; Matsui, M.; Arthur, T. S.; Hwang, S.-J., *Angew. Chem. Int. Ed.* **2012**, 51, 9780.

(15) Doe, R. E.; Han, R.; Hwang, J.; Gmitter, A. J.; Shterenberg, I.; Yoo, H. D.; Pour, N.; Aurbach, D., *Chem. Commun.* **2013**, 50, 243.

(16) Shao, Y.; Liu, T.; Li, G.; Gu, M.; Nie, Z.; Engelhard, M.; Xiao, J.; Lv, D.; Wang, C.; Zhang, J.-G.; Liu, J., *Sci. Rep.* **2013**, 3, 3130.

(17) Ha, S.-Y.; Lee, Y.-W.; Woo, S. W.; Koo, B.; Kim, J.-S.; Cho, J.; Lee, K. T.; Choi, N.-S., *ACS Appl. Mater. Interfaces* **2014**, 6, 4063.

(18) Orikasa, Y.; Masese, T.; Koyama, Y.; Mori, T.; Hattori, M.; Yamamoto, K.; Okado, T.; Huang, Z.-D.; Minato, T.; Tassel, C.; Kim, J.; Kobayashi, Y.; Abe, T.; Kageyama, H.; Uchimoto, Y., *Sci. Rep.* **2014**, 4, 5622.

(19) Fukutsuka, T.; Asaka, K.; Inoo, A.; Yasui, R.; Miyazaki, K.; Abe, T.; Nishio, K.; Uchimoto, Y., *Chem. Lett.* **2014**, 43, 1788.

(20) Carter, T. J.; Mohtadi, R.; Arthur, T. S.; Mizuno, F.; Zhang, R.; Shirai, S.; Kampf, J., *Angew. Chem. Int. Ed.* **2014**, 53, 3173.

(21) Shterenberg, I; Salama, M.; Yoo, H. D.; Gofer, Y.; Park, J.-B.; Sun, Y. –K.; Aurbach, D., *J. Electrochem. Soc.* **2015**, 162, A7118.

(22) Shao, Y.; Rajput, N. N.; Hu, J.; Hu, M.; Liu, T.; Wei, Z.; Gu, M.; Deng, X.; Xu, S.; Han, K. S.; Wang, J.; Nie, Z.; Li, G.; Zavadil, K. R.; Xiao, J.; Wang, C.; Henderson, W. A.; Zhang, J. –G.; Wang, Y.; Mueller, K. T.; Persson, K.; Liu, J., *Nano Energy.* **2015**, 12, 750.

(23) Rajput, N. N.; Qu, X.; Sa, N.; Burrell, A. K.; Persson, K. A., *J. Am. Chem. Soc.* **2015**, 137, 3411.

(24) Watkins, T.; Kumar, A.; Buttry, D. A., *J. Am. Chem. Soc.* **2016**, 138, 641.

(25) Arthur, T. S.; Glans, P. –A.; Singh, N.; Tutusaus, O.; Nie, K.; Liu, Y. –S.; Mizuno, F.; Guo, J.; Alsem, D. H.; Salmon, N. J.; Mohtadi, R., *Chem. Mater.* **2017**, 29, 7183-.

(26) Chang, J.; Haasch, R. T.; Kim, J. –W.; Spila, T.; Braun, P. V.; Gewirth, A. A.; Nuzzo, R. G., *ACS Appl. Mater. Interfaces* **2015**, 7, 2494.

(27) Nakayama, Y.; Kudo, Y.; Oki, H.; Yamamoto, K.; Kitajima, Y.; Noda, K., *J. Electrochem. Soc.* **2008**, 155, A754.

(28) Wan, L. F.; Prendergast, D., *J. Am. Chem. Soc*. **2014**, 136, 14456.

(29) Ravel, B.; Newville, M., *J. Synchrotron Rad.* **2005**, 12, 537.

(30) Taylor, R. C.; Schultz, D. R.; Emery, A. R., *J. Am. Chem. Soc*. **1958**, 80, 27.

(31) Emery, A. R.; Taylor, R. C., *J. Chem. Phys.* **1958**, 28, 1029.

(32) Shirk, A. E.; Shriver, D. F., *J. Am. Chem. Soc.* **1973**, 95, 5904.

(33) Marks, T. J.; Kolb, J. R. *Chem. Rev.* **1977**, 77, 263.

(34) Cerny, R.; Filinchuk, Y.; Hagemann, H.; Yvon, K., *Angew. Chem. Int., Ed.* **2007**, 46, 5765.

(35) Parker, S. F., *Coordin. Chem. Rev.* **2010**, 254, 215.

(36) Poonia, N. S.; Bajaj, A. V., *Chem. Rev.* **1979**, 79, 389.

(37) Kimura, T.; Fujii, K.; Sato, Y.; Morita, M.; Yoshimoto, N.,*J. Phys. Chem. C* **2015**, 119, 18911.

(38) Hattori, M.; Yamamoto, K.; Nakanishi, K.; Mandai, T.; Choudhary, A.; Tateyama, Y.; Sodeyama, K.; Uchiyama, T.; Matsui, M.; Orikasa, Y.; Tamenori, Y.; Takeguchi, T.; Kanamura, K.; Uchimoto, Y., *ACS Appl. Mater. Interfaces submitted.*

(39) Pearson, R. G., *J. Am. Chem. Soc.* **1963**, 85, 3533.

(40) Pearson, R. G., *J. Chem. Educ.* **1968**, 45, 581.

(41) Pearson, R. G., *J. Chem. Educ.* **1968**, 45, 643.

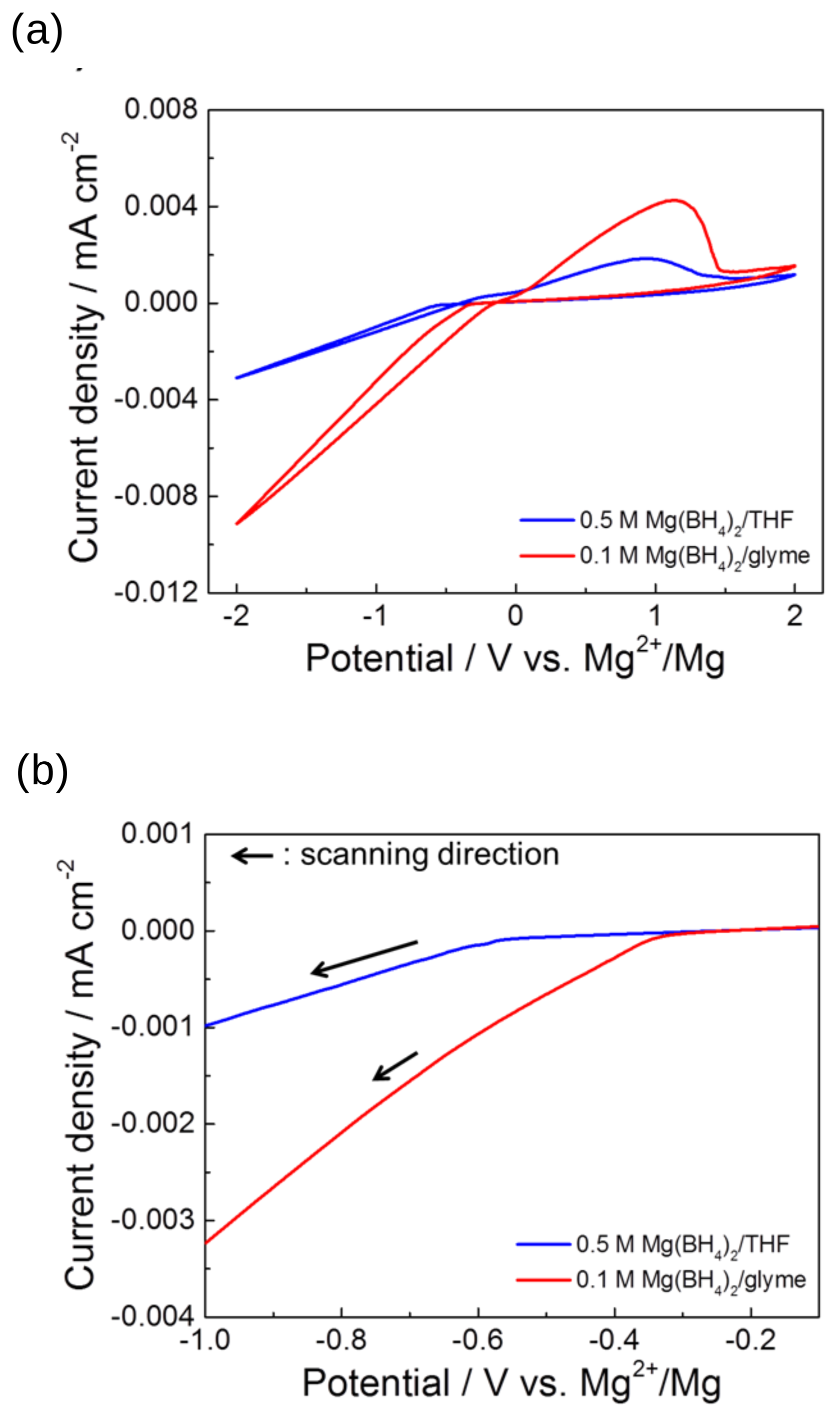

Figure 4-1. (a) Cyclic voltammograms of bismuth electrode in 0.5 M $Mg(BH_4)_2$/THF and 0.1 M $Mg(BH_4)_2$/glyme at a scanning rate of 20 mV/sec. (b) Enlarged figure of (a) between -1.0 V and -0.1 V (vs. Mg^{2+}/Mg).

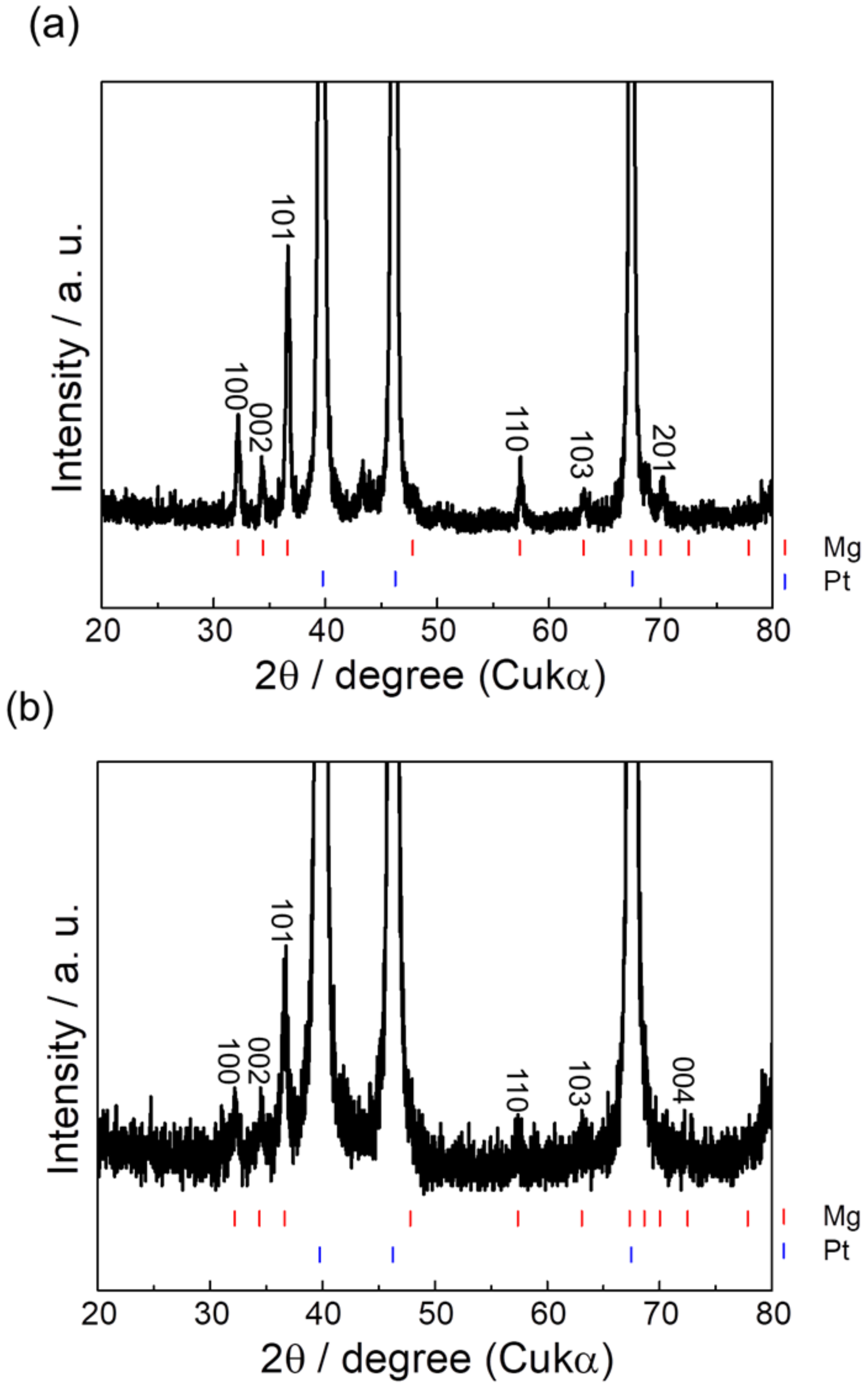

Figure. 4-2. XRD patterns of electrodeposited of (a)0.5 M $Mg(BH_4)_2$/THF and (b)0.1 M $Mg(BH_4)_2$/glyme on Pt substrate after electrochemical measurements.

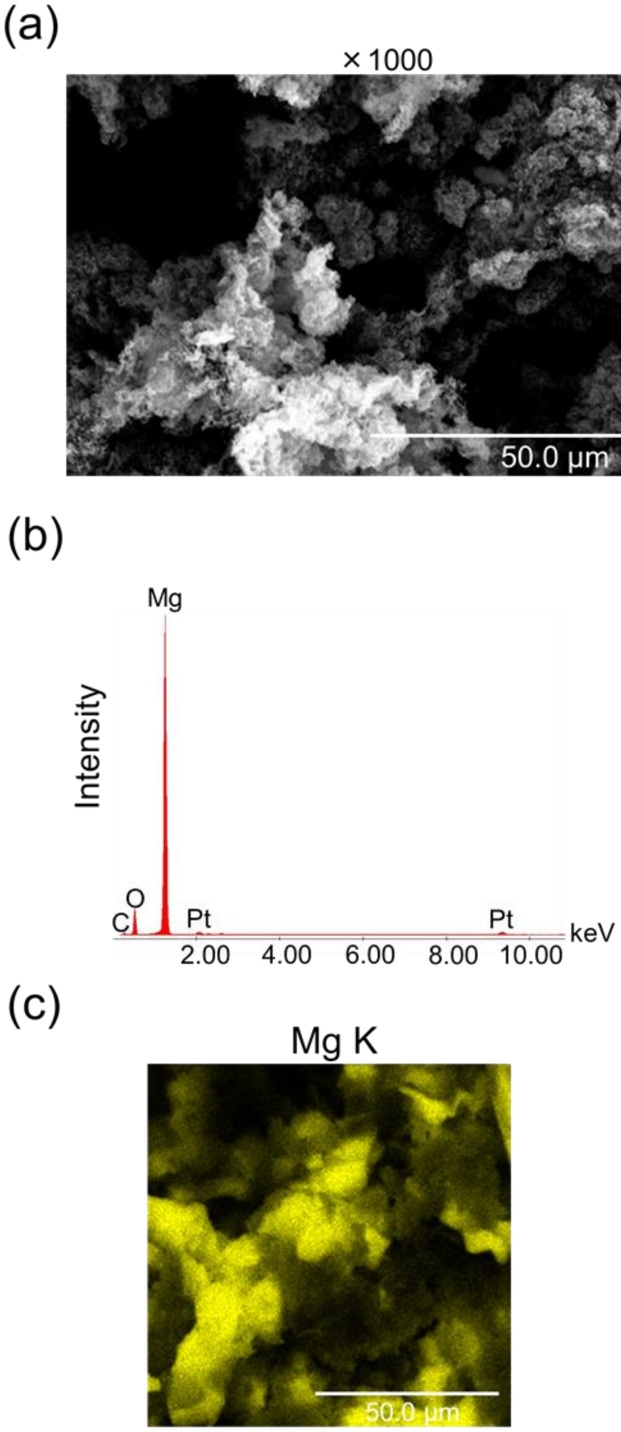

Figure. 4-3. (a) SEM image, (b) EDX spectrum and (c) EDX mapping of Mg K for electrodeposited on Pt substrate after electrochemical measurement in 0.5 M $Mg(BH_4)_2$/THF.

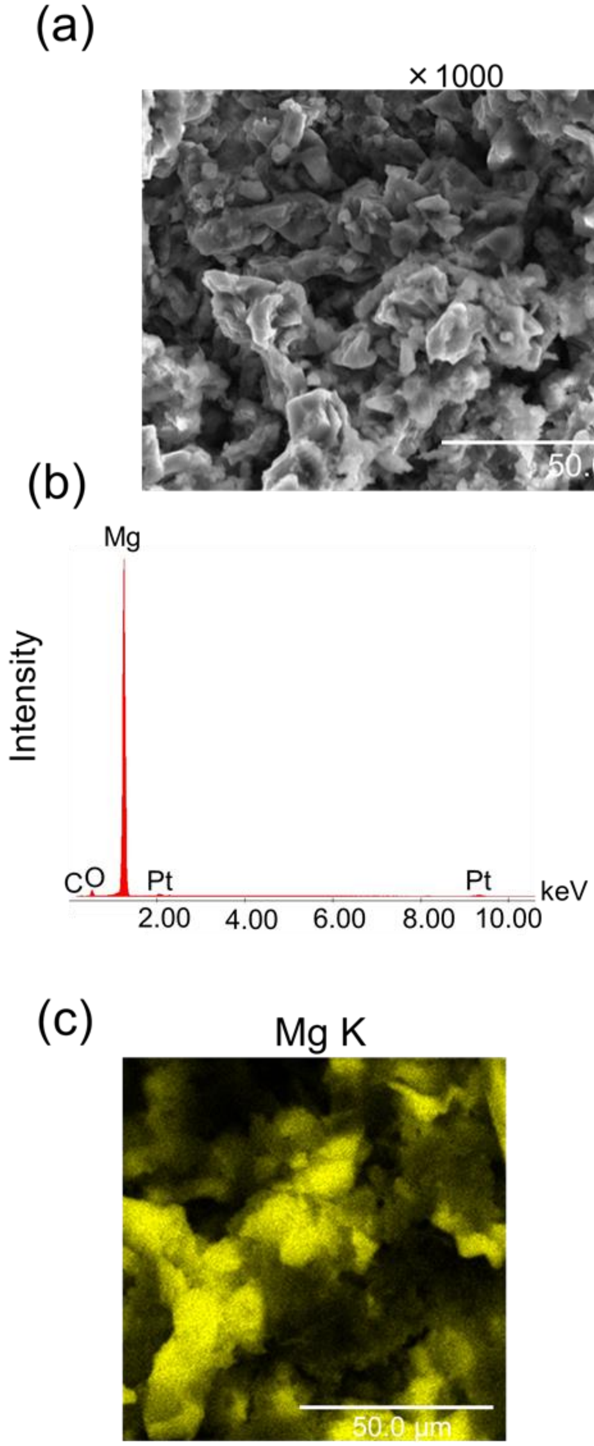

Figure. 4-4. (a) SEM image, (b) EDX spectrum and (c) EDX mapping of Mg K for electrodeposited bismuth on Pt substrate after electrochemical measurement in 0.1 M Mg(BH$_4$)$_2$/glyme.

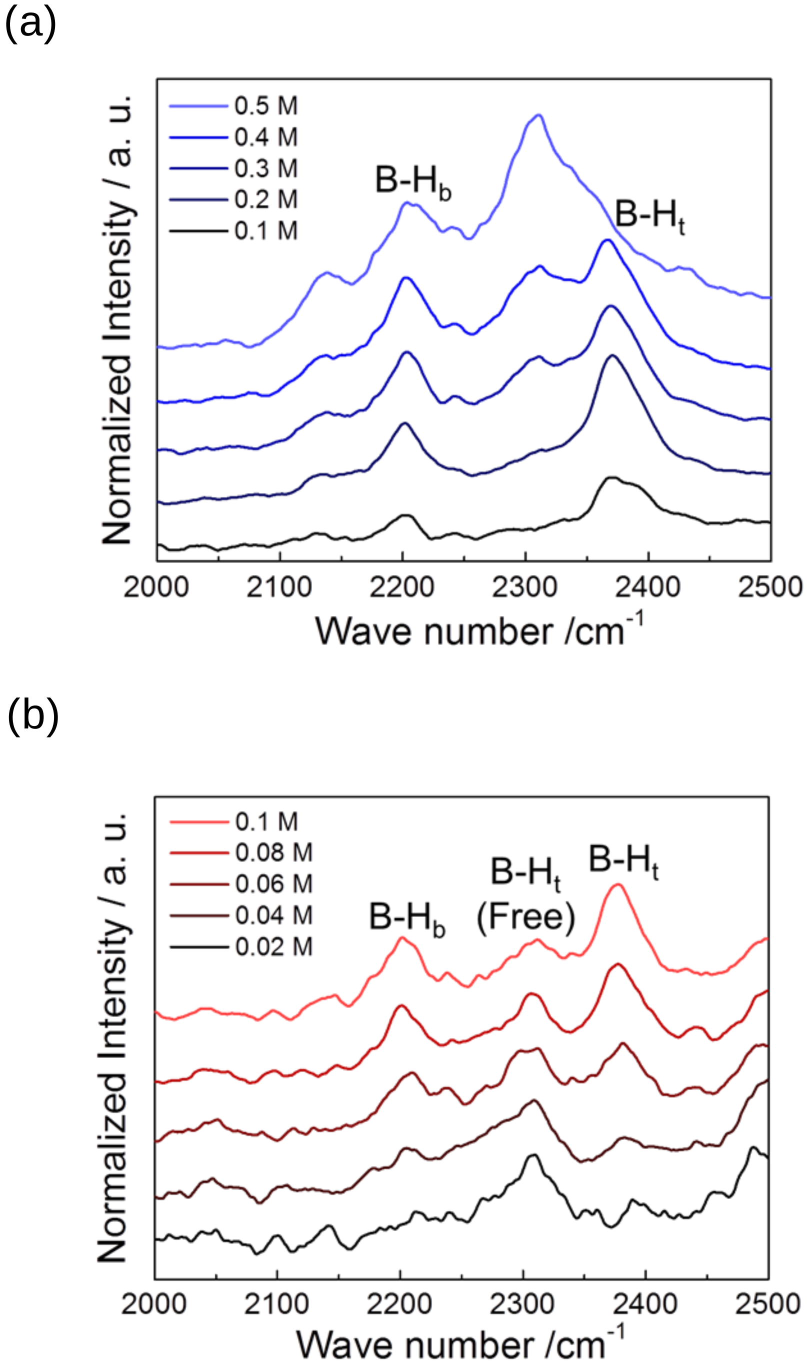

Figure. 4-5. Raman spectra of (a) $Mg(BH_4)_2$/THF and (b) $Mg(BH_4)_2$/glyme in several concentration in the region between 2000 and 2500 cm^{-1}.

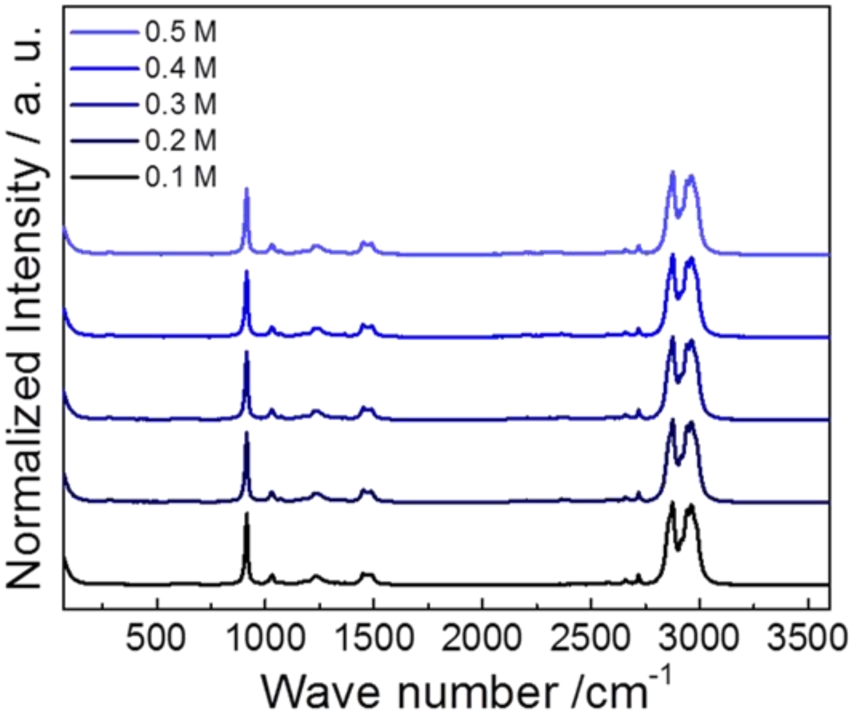

Figure. 4-6. Raman spectra of the several concentration of $Mg(BH_4)_2$/THF for 70 – 3600 cm^{-1}.

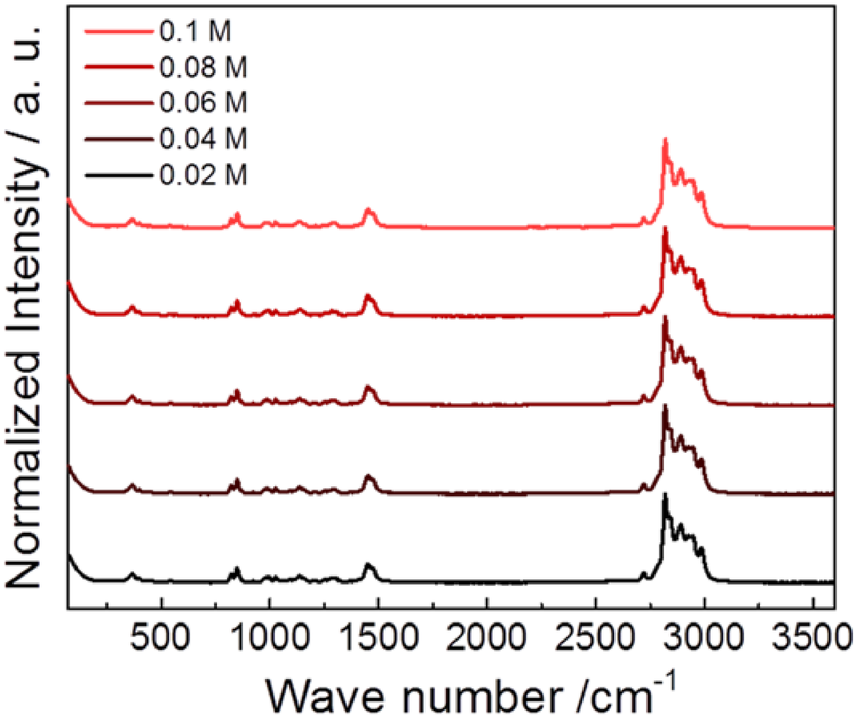

Figure. 4-7. Raman spectra of the $Mg(BH_4)_2$/THF for 70 – 3600 cm^{-1}.

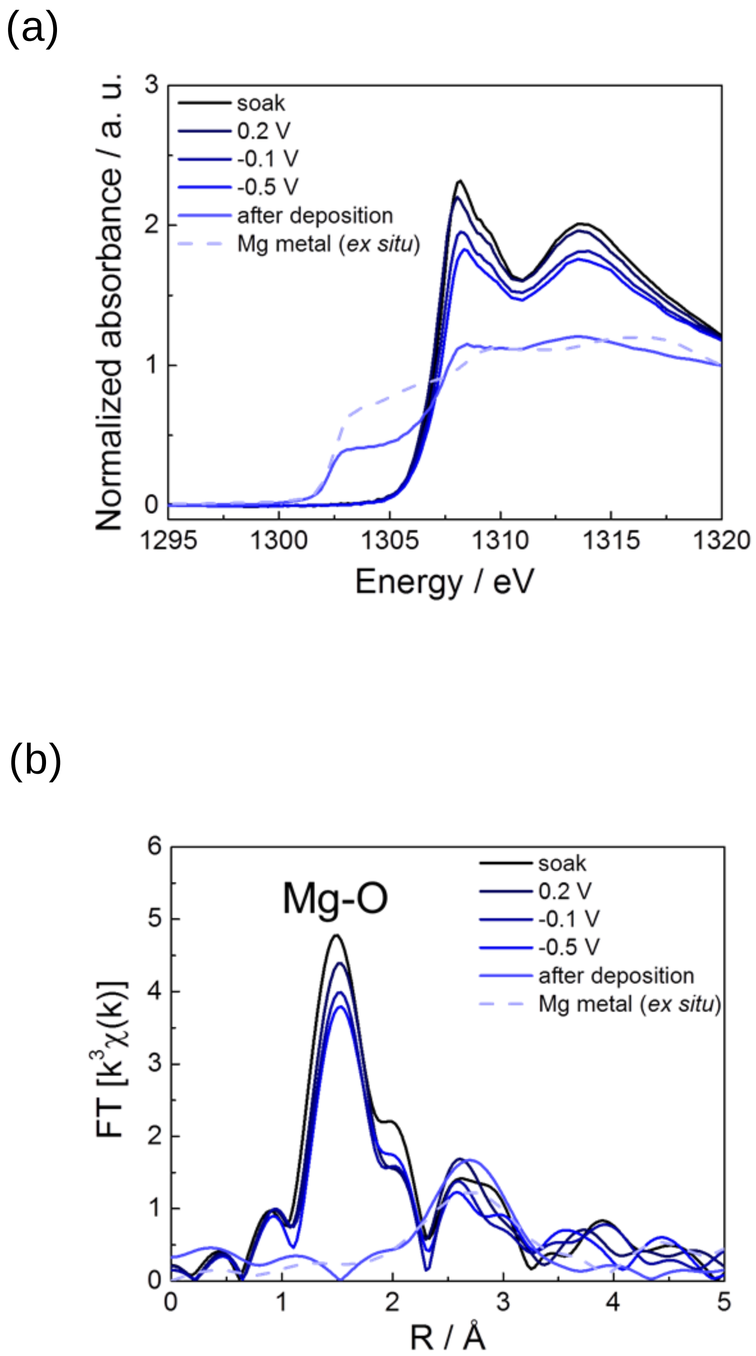

Figure. 4-8. Mg *K*-edge (a) XANES and (b) Fourier-transformed EXAFS spectra obtained from *operando* XAS measurements 0.5 M $Mg(BH_4)_2$/THF. The potential is expressed on vs. Mg^{2+}/Mg.

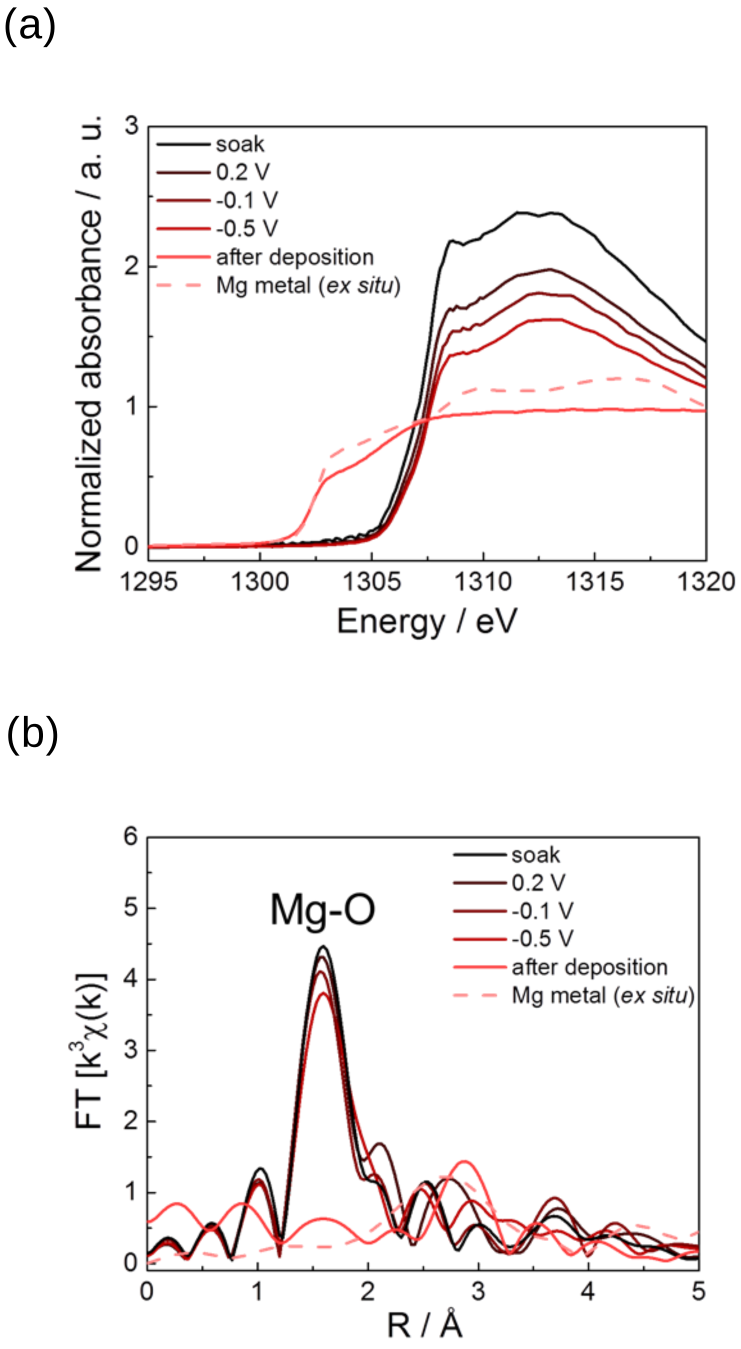

Figure. 4-9. Mg *K*-edge (a) XANES and (b) Fourier-transformed EXAFS spectra obtained from *operando* XAS measurements 0.1 M Mg(BH$_4$)$_2$/glyme. The potential is expressed on vs. Mg^{2+}/Mg.

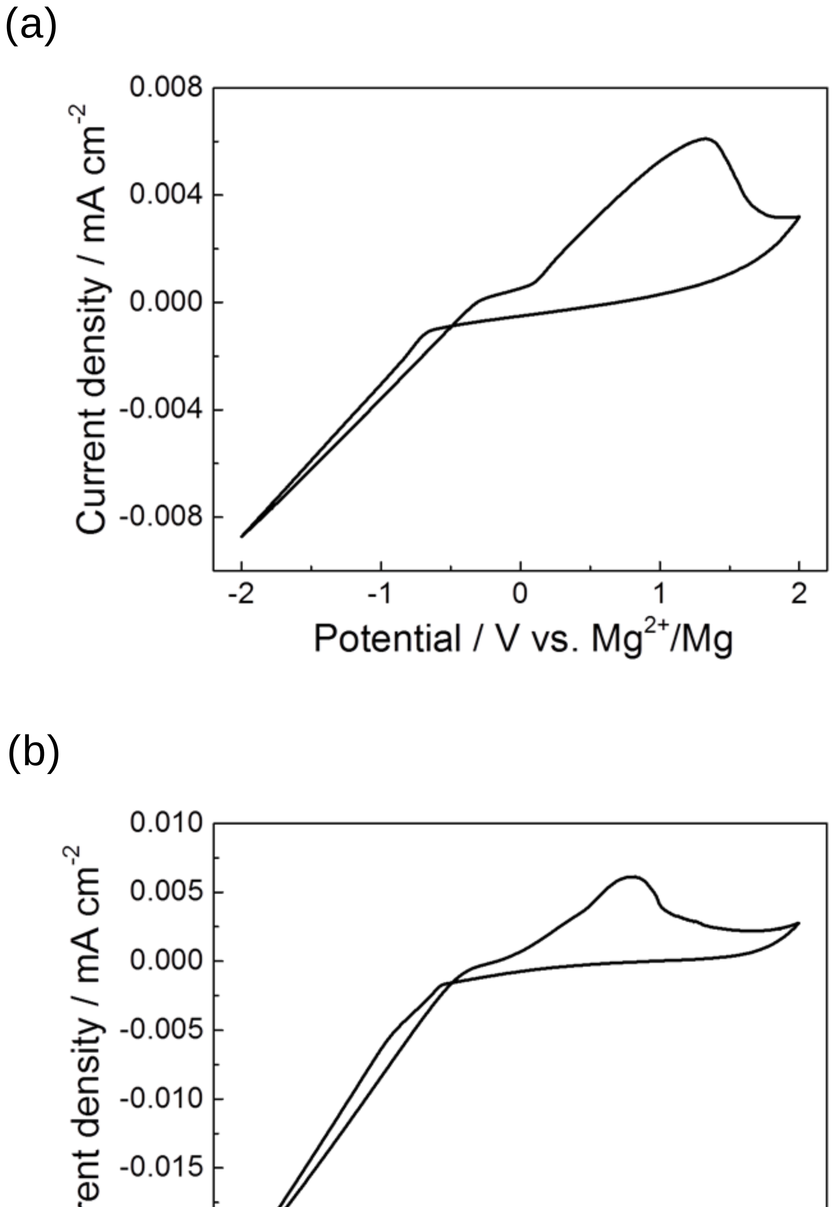

Figure. 4-10. Cyclic voltammograms of (a) 0.5 M $Mg(BH_4)_2$/THF and (b) 0.1 M $Mg(BH_4)_2$/glyme using *operando* XAS cell with sweeping rate of 20 mV/s.

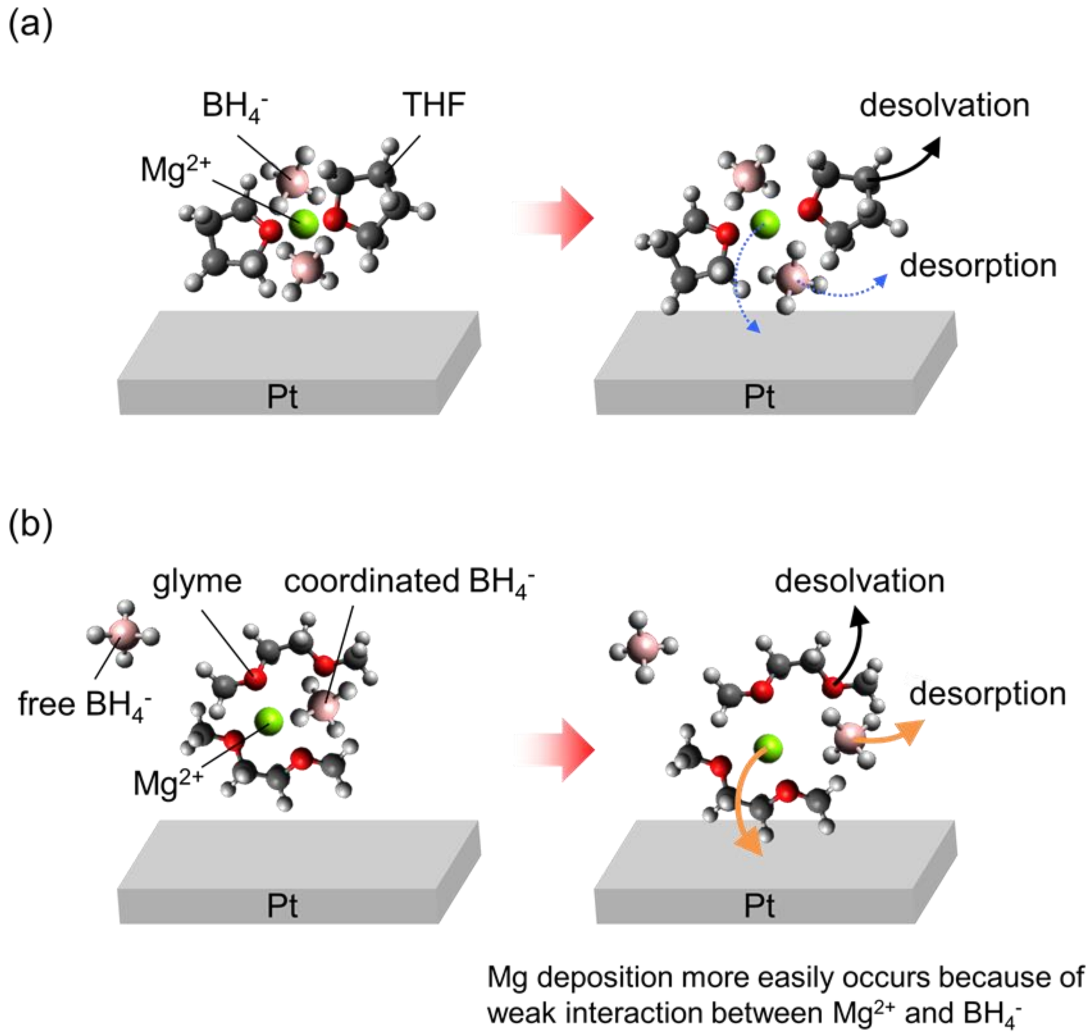

Mg deposition more easily occurs because of weak interaction between Mg^{2+} and BH$_4^-$

Figure. 4-11. Schematic illustrations of the reaction mechanism of magnesium deposition in the (a) 0.5 M $Mg(BH_4)_2$/THF and (b) 0.1 M $Mg(BH_4)_2$/glyme. The left part is under soak situation, and right part is under applying negative potential.

Chapter 5: The Effects of Additive of Magnesium Rechargeable Anode Reaction

5.1 Introduction

Magnesium rechargeable batteries are candidate for next-generation rechargeable batteries, because magnesium metal has high theoretical volumetric capacity (3834 mAh/cm^3) and relatively low reduction potential (-2.356 V *vs.* SHE), expected high energy density.[1,2] Further, the safety and cost of magnesium metal are superior to lithium metal.[3-5] These properties of magnesium metal make magnesium rechargeable batteries attractive. However, conventional batteries containing inorganic salts and carbonate solvents electrolytes cannot be used for reversible deposition and dissolution of magnesium metal, because a passivation layer is formed at the magnesium metal anode surface that blocks both magnesium ions and electron transport[6]. Grignard reagents based electrolytes have been widely known as the electrolyte which occur reversible magnesium metal deposition/dissolution reactions[7-12]. However, these electrolytes have the problems narrow electrochemical potential window and corrosion reactions because of the halide contained in these electrolytes.

Resolving the problems that Grignard reagents based electrolytes have, many researchers have developed the new halide-free electrolytes which consist of inorganic magnesium salts and ethereal solvents or ionic liquid and have realized reversible magnesium metal deposition/dissolution reactions.[13-21] Among these electrolytes, magnesium borohydride ($Mg(BH_4)_2$) based electrolytes, which has been firstly reported Mohtadi *et al.*[14], are attractive electrolytes because of high coulombic efficiency for magnesium metal deposition/dissolution reactions, and have been studied by several research groups.[14,16,22] Mohtadi and other groups have suggested that $Mg(BH_4)_2$/ether electrolytes contain contact ion pair $Mg[(\mu\text{-}H)_2BH_2]_2$ based on the results of several spectroscopy techniques.[14,16] Rajput *et al.* has reported that ion pair between magnesium ions and BH_4^- does not occur decomposition reaction during magnesium metal deposition reaction by theoretical calculation.[23] Several groups have reported that the magnesium metal deposition/dissolution reactions are improved by changing the longer chain length of glyme-based solvents or adding lithium borohydride ($LiBH_4$) in $Mg(BH_4)_2$/ether electrolytes.[14,16,24-26] However, the improved coulombic efficiency of magnesium metal deposition/dissolution reaction in $Mg(BH_4)_2$ based electrolytes with additives has not been understood, because the knowledge about behavior of magnesium ions at the interface between negative electrode and electrolyte during magnesium metal deposition reaction process.

Recently, *operando* X-ray absorption spectroscopy technique under magnesium metal deposition reaction process (*operando* XAS) has been developed and applied to examine the interfacial behavior of magnesium electrolytes.[25] XAS is a powerful technique to examine electronic and local structure around Mg^{2+} for magnesium electrolytes.[27,28] Arthur *et al.* examined the interfacial structure between negative electrode and $Mg(BH_4)_2$/ ethylene glycol dimethyl ether (glyme) electrolytes using the *operando* XAS and suggested that solid electrolyte interphase (SEI) formed, which can pass magnesium ions, on the negative electrode surface after magnesium metal deposition reaction.[25] However, the coordination structure of magnesium ions in $Mg(BH_4)_2$ based electrolyte with additives before magnesium metal deposition reaction occurs, has not been examined. In this study, we examined the coordination structure of Mg^{2+} in $Mg(BH_4)_2$/ether-based electrolytes with additives during magnesium metal deposition reaction using the *operando* soft X-ray absorption spectroscopy combined with Raman spectroscopy.

5.2 Experimental

5.2.1. Material preparation

0.1 M magnesium borohydride ($Mg(BH_4)_2$)/ethylene glycol dimethyl ether (glyme) electrolyte were prepared by stirring $Mg(BH_4)_2$ (SIGMA-ALDRICH, 95%) with glyme (KISHIDA CHEMICAL Co., Ltd., 99.5%) in an argon-filled glove box overnight at room temperature. Lithium borohydride (**(**$LiBH_4$) (SIGMA-ALDRICH, 95%) and potassium borohydride (KBH_4) (SIGMA-ALDRICH, 98%) were further added respectively. The solvent was dried by using molecular sieves 3A for 48 hours to decrease the water content before use. After drying, the water content of the prepared electrolytes was less than 30 ppm, which was confirmed by Karl Fischer titration.

5.2.2. Electrochemical measurements

Electrochemical measurements were carried out using a three-electrode cell. The working electrode was a platinum plate. The counter and the reference electrodes were magnesium rods, which were polished in an argon-filled glove box before assembling cells. Cyclic voltammetry was carried out at 25˚C with a sweeping potential rate of 5 mV/sec. The potential range was -1.5 V - 2.0 V (vs. Mg^{2+}/Mg).

5.2.3. XRD measurements

X-ray diffraction was performed by Ultima IV (Rigaku Co., Inc.) with X-ray source of CuKα. Scanning electron microscopy (SEM) images operated at a potential of 15 kV and energy dispersive X-ray spectroscopy (EDX) spectra at electron energy of 25 keV were collected by S-3400 N (Hitachi High-Tech Co.). After potentiostatic deposition of magnesium metal, the electrochemical measured cells were disassembled, then the obtained electrodes were washed with glyme. These electrodes were dried in an argon-filled glove box overnight at room temperature. All measurements were conducted without air exposure of the samples.

5.2.4. Raman spectroscopy

The Raman spectra of the magnesium electrolytes were measured by MultiRAM (Bruker Optics Co., Ltd.) equipped with Nd-YAG laser (1064 nm) at room temperature. The measurement range was between 70 and 3600 cm^{-1} for 0.1 M $Mg(BH_4)_2$ + x M $LiBH_4$/glyme (x = 0, 0.05, 0.1, 0.2, 0.3) and 0.1 M $Mg(BH_4)_2$ + x M KBH_4/glyme (x = 0, 0.05, 0.1, 0.2, 0.3). The electrolyte was set into glass vessel and sealed in them in an argon-filled glove box, and measured without air exposure.

5.2.5. Soft X-ray absorption spectroscopy

operando XAS spectra of the electrolytes in the energy region of Mg *K*-edge were collected by partial fluorescence yield method at the beam line of the SPring-8 synchrotron radiation facility (BL27SU) in Hyogo, Japan. A custom made three-electrode cell was used for *operando* XAS measurements. Chromium layer with the thickness of 5 nm was pre-deposited as a buffer silicon nitride (Si_3N_4) window with 200 nm thickness (ALLIANCE Biosystems Inc.), and then platinum layer with the thickness of 30 nm was deposited on the Cr/Si_3N_4 window by using magnetron sputtering on the respectively. The prepared Pt/Cr/Si_3N_4 window was employed as a working electrode. The counter and reference electrodes were polished magnesium plate, which were polished in an argon-filled glove box before assembling cells. The *operando* cell was assembled in an argon-filled glove box and transferred into a vacuum chamber for the XAS measurements without air exposure. The *operando* XAS measurements were performed under keeping the potentials after decreasing the potential of the working electrode at several different potentials before magnesium metal deposition reaction does not start. Then, magnesium metal was deposited on the working electrode by applying potential step method, and additional XAS measurements were conducted. The analysis of the obtained XAS spectra was using ATHENA program.[29]

5.3 Results and Discussion

5.3.1 Cyclic voltammetry.

Magnesium metal deposition/dissolution reactions were examined for the 0.1 M $Mg(BH_4)_2$ + 0.3 M $LiBH_4$/glyme and 0.1 M $Mg(BH_4)_2$ + 0.3 M KBH_4/glyme by cyclic voltammetry. Figure 5-1 (a) shows the obtained cyclic voltammograms. In both electrolytes, cathodic and anodic currents, which are attributed to magnesium metal deposition and dissolution reactions, were observed. XRD and SEM-EDX confirmed that the deposited product after the cathodic current occurred in the both electrolytes was magnesium metal (Supplementary Figure 5-2, 5-3 and 5-4). The coulombic efficiency of magnesium metal deposition/dissolutions reactions was 65% and 47% in the 0.1 M $Mg(BH_4)_2$ + 0.3 M $LiBH_4$/glyme and 0.1 M $Mg(BH_4)_2$ + 0.3 M KBH_4/glyme, respectively. These results are improved by that in 0.1M $Mg(BH_4)_2$/glyme. The current values of the magnesium metal deposition/dissolution reactions in the

0.1 M $Mg(BH_4)_2$ + 0.3 M $LiBH_4$/glyme were larger than those in the 0.1 M $Mg(BH_4)_2$ + 0.3 M KBH_4/glyme. Besides, the overpotential of magnesium metal deposition reaction of 0.1 M $Mg(BH_4)_2$ + 0.3 M $LiBH_4$/glyme is smaller than that of 0.1 M $Mg(BH_4)_2$ + 0.3 M KBH_4/glyme. (see Figure 5-1 (b)) These results correspond to the previous report.[14]

5.3.2 Raman spectroscopy.

The coordination structure of BH_4^- in 0.1 M $Mg(BH_4)_2$ + $LiBH_4$/glyme and 0.1 M $Mg(BH_4)_2$ + KBH_4/glyme were examined by Raman spectroscopy. Figure 5-5 (a) and 5-6 (a) present the Raman spectra ranging from 2000 to 2500 cm^{-1} in 0.1 M $Mg(BH_4)_2$ + x M $LiBH_4$/glyme (x = 0, 0.05, 0.1, 0.2, 0.3) and 0.1 M $Mg(BH_4)_2$ + x M KBH_4/glyme (x = 0, 0.05, 0.1, 0.2, 0.3), respectively. The spectra in whole region were shown in Supplementary Figure 5-7 and 5-9. The peak appearing between 2100 and 2500 cm^{-1} are attributed to B-H stretching vibration of BH_4^- coordinated to cation[24, 29-35]. For all electrolytes, the peaks were observed at 2200 cm^{-1}, 2310 cm^{-1} and 2380 cm^{-1}. The peaks at 2200 cm^{-1} and 2380 cm^{-1} were assigned to bridging B-H_b vibration and B-H_t vibration, respectively. Moreover, we assigned that the peak at 2310 cm^{-1} to be B-H vibration of non-coordinating BH_4^- (free BH_4^-). These peaks at 2200 cm^{-1}, 2310 cm^{-1}, and 2380 cm^{-1} were increased with the increasing concentration. According to the peak separation, the ratio of free BH_4^- of 0.1 M $Mg(BH_4)_2$ + x M $LiBH_4$/glyme is larger than that of 0.1 M $Mg(BH_4)_2$/glyme. On the other hand, the ratio of free BH_4^- of 0.1 M $Mg(BH_4)_2$ + x M KBH_4/glyme is same as that of 0.1 M $Mg(BH_4)_2$/glyme. Glyme wraps Mg^{2+} by two oxygen sites in the molecule, weakening the interaction Mg^{2+} and BH_4^-.[16,35] Watkins *et al.* reported that the similar tendency appeared in ionic liquid system containing polyethylene glycol chains[24]. Therefore, free BH_4^- exists in the 0.1 M $Mg(BH_4)_2$ + x M $LiBH_4$/glyme due to the weak interaction unlike in the 0.1 M $Mg(BH_4)_2$ + x M KBH_4/glyme. All fitting results are shown in Figure 5-8 (b) and 5-10 (b). In both electrolytes, the peak at 570 and 923 cm^{-1} were assigned to boron cluster as $[B_{12}H_{12}]^{2-}$. Then, boron cluster as $[B_{12}H_{12}]^{2-}$ is formed in both electrolytes.[36]

5.3.3 Comprehensive model for $LiBH_4$ and KBH_4 additive mechanism.

In order to examine the electronic and local structure of Mg^{2+} from cation side under applying potential in the 0.1 M $Mg(BH_4)_2$ + 0.3 M $LiBH_4$/glyme and 0.1 M $Mg(BH_4)_2$ + 0.3 M KBH_4/glyme, we conducted the *operando* XAS measurements. Figure 5-11. and 5-12. how Mg *K*-edge XANES and Fourier-transformed EXAFS spectra at several potentials for 0.1 M $Mg(BH_4)_2$ + 0.3 M $LiBH_4$/glyme and 0.1 M $Mg(BH_4)_2$ + 0.3 M KBH_4/glyme, respectively. The cyclic voltammograms of each electrolyte using the *operando* cells were shown in Figure 5-13. For 0.1 M $Mg(BH_4)_2$ + 0.3 M $LiBH_4$/glyme, the peak intensity of XANES (Figure 4(a)) gradually decreased from the soak state to -0.1 V, which is the potential slightly before magnesium metal deposition reaction starts (Figure 5-11(a)), then the XANES drastically changed after magnesium metal deposition reaction. These results mean electronic structure of magnesium ions, which is influenced by the coordination structure of magnesium ions, changed during magnesium metal deposition reaction process. In the EXAFS spectra (Figure 5-11(b)). a peak was observed at 1.64 Å. Although Mg^{2+} coordinates with glyme and BH_4^- from results of Raman spectroscopy, the Mg-H bond should not be detected by EXAFS analysis because the back scattering of hydrogen is the smallest of all the elements. Therefore, we assigned the peak to Mg-O bond between Mg^{2+} and glyme. The intensity of the peak in the EXAFS spectrum decreased from the soak state to -0.1 V, meaning that the coordination number decreased and/or local distortion increased of Mg^{2+}. Then, the EXAFS spectra changed after magnesium metal deposition reaction and the peak that is attributed to Mg-Mg bond of magnesium metal appeared at 2.66 Å.

For 0.1 M $Mg(BH_4)_2$ + 0.3 M KBH_4/glyme, the peak intensity of XANES (Figure 5-12 (a)) gradually decreased from the soak state to -0.5 V, which is the potential before magnesium metal deposition reaction starts (Figure 5-13 (b)). The decreasing degree of the intensity in the 0.1 M $Mg(BH_4)_2$ + 0.3 M KBH_4/glyme was smaller than that of the intensity in the 0.1 M $Mg(BH)_2$ + 0.3 M $LiBH_4$/glyme. These results mean that the coordination structure of Mg^{2+} changed smaller in the 0.1 M $Mg(BH_4)_2$ + 0.3 M KBH_4/glyme than that of Mg^{2+} in the 0.1 M $Mg(BH)_2$ + 0.3 M $LiBH_4$/glyme. In the EXAFS spectra (Figure 5-12 (b)), a peak was observed at 1.64 Å.

In the 0.1 M $Mg(BH_4)_2$ + 0.3 M KBH_4/glyme, although Mg^{2+} coordinates with glyme and BH_4^-, the peak was assigned to Mg-O bond between Mg^{2+} and glyme. However, the Mg-H bond should not be detected by EXAFS analysis, because the back scattering of hydrogen is the smallest of all the elements. The peak gradually decreased under applying potential before magnesium metal deposition reaction starts. After magnesium metal deposition reaction occurs, the EXAFS spectra drastically changed and the peak that is attributed to Mg-Mg bond of magnesium metal appeared at 2.74 Å.

5.3.4 Discussion

Magnesium deposition reaction occurs in the both electrolytes, the ligands should desorb from magnesium ions during the deposition process. Based on the results from *operando* XAS measurements, we discuss the correlation between the electrochemical property and the coordination structure of magnesium ions during magnesium deposition process.

The coulombic efficiency of magnesium metal deposition/dissolution reaction of 0.1 M $Mg(BH_4)_2$ + $LiBH_4$/glyme and 0.1 M $Mg(BH_4)_2$ + KBH_4/glyme is improved by that of 0.1 M $Mg(BH_4)_2$/glyme. Based on the results from Raman spectroscopy and *operando* XAS measurements, we discuss the correlation between the electrochemical property and the coordination structure of magnesium ions under applying potential.

For 0.1 M $Mg(BH_4)_2$ + $LiBH_4$/glyme, the ratio of free BH_4^- is higher than that of 0.1 M $Mg(BH_4)_2$ + KBH_4/glyme. EXAFS spectra indicates that the desolvation of glyme from magnesium ions, and XANES indicates that desorption of glyme as well as BH_4^-. The change of the EXAFS spectra in the 0.1 M $Mg(BH_4)_2$ + $LiBH_4$/glyme is larger than that in 0.1 M $Mg(BH_4)_2$ + KBH_4/glyme, because lithium ions are attracted BH_4 anions and glyme. This result is similar of Ohara's group.[37] They reported that the molten salts consisted of $Mg(TFSA)_2$, CsTFSA and LiTFSA occurs the magnesium metal deposition/dissolution reaction, because lithium ions are strongly attracted $[TFSA]^-$ and/or glyme, then the bond length of Mg-N in the molten salts consisted of $Mg(TFSA)_2$, CsTFSA and LiTFSA is longer than that in the molten salts consisted of $Mg(TFSA)_2$ and CsTFSA. Then, adding $LiBH_4$ in $Mg(BH_4)_2$/glyme desorb more easily glyme and/or BH_4^- than adding KBH_4 in in $Mg(BH_4)_2$/glyme.

Figure 5-14 schematically illustrates the behavior of the magnesium ions at the negative electrode/electrolyte. For 0.1 M $Mg(BH_4)_2$ + KBH_4/glyme, the ratio of free BH_4^- is same as that of 0.1 M $Mg(BH_4)_2$/glyme. The change degree of the EXAFS spectra in 0.1 M $Mg(BH_4)_2$ + KBH_4/glyme is same as that in 0.1 M $Mg(BH_4)_2$/glyme. These results indicate that potassium ions are not strongly attracted $[TFSA]^-$ and/or glyme, because the size of potassium ions are large. From these results, additives that strongly attract anion and solvent in the electrolytes lead to improved coulomb efficiency of magnesium metal deposition/dissolution reactions.

5.4 Conclusions

In this work, we examined the coordination structure of magnesium ions in 0.1 M $Mg(BH_4)_2$ + $LiBH_4$/glyme and 0.1 M $Mg(BH_4)_2$ + KBH_4/glyme at the interface between the negative electrode and electrolyte under applying potential. Adding $LiBH_4$ in $Mg(BH_4)_2$/glyme, the currents of magnesium metal deposition/dissolution reactions, the coulombic efficiency of magnesium metal deposition/dissolution reactions and the ratio of free BH_4^- are more increased than that in 0.1 M $Mg(BH_4)_2$/glyme, because lithium ions are attracted BH_4^- and/or glyme. On the other hand, adding KBH_4 in $Mg(BH_4)_2$/glyme, the currents of magnesium metal deposition/dissolution reactions and the coulombic efficiency of magnesium metal deposition/dissolution reactions are a little increasing. The ratio of free BH_4^- is the same as 0.1 M $Mg(BH_4)_2$/glyme, because the potassium ions are not attracted BH_4^- and glyme. The important factor of improved magnesium metal deposition/dissolution is that additives contain cations with high surface charge density.

References

(1) Armand, M.; Tarascon, J. M., *Nature* **2008**, 451, 652.

(2) Yoo, H. D.; Shterenberg, I.; Gofer, Y.; Gershinsky, G.; Pour, N.; Aurbach, D., *Energy Environ. Sci.* **2013**, 6, 2265.

(3) Gregory, T. D.; Hoffman, R. J.; Winterton, R. C., *J. Electrochem. Soc.* **1990**, 137, 775.

(4) Novák, P.; Imhof, R.; Haas, O., *Electrochim. Acta* **1999**, 45, 351.

(5) Besenhard, J. O.; Winter, M. A., *ChemPhysChem* **2002**, 3, 155.

(6) Lu, Z.; Schechter, A.; Moshkovich, M.; Aurbach, D., *J. Electroanal. Chem.* **1999**, 466, 203.

(7) Aurbach, D.; Lu, Z.; Schechter, A.; Gofer, Y.; Gizbar, H; Turgeman, R.; Cohen, Y.; Moshkovich, M.; Levi, E., *Nature* **2000**, 407, 724–727.

(8) Aurbach, D.; Schechter, A.; Moshkovich, M.; Cohen, Y., *J. Electrochem. Soc.* **2001**, 148, A1004.

(9) Aurbach, D.; Gizbar, H.; Schechter, A.; Chusid, O.; Gottlieb, H. E.; Gofer, Y.; Goldberg, I., *J. Electrochem. Soc.* **2002**, 149, A115.

(10) Mizrahi, O.; Amir, N.; Pollak, E.; Chusid, O.; Marks, V.; Gottlieb, H.; Larush, L.; Zinigrad, E.; Aurbach, D., *J. Electrochem. Soc.* **2008**, 155, A103.

(11) Pour, N.; Gofer, Y.; Major, D. T.; Aurbach, D., *J. Am. Chem. Soc.* **2011**, 133, 6270.

(12) Kim, H. S.; Arthur, T. S.; Allred, G. D.; Zajicek, J.; Newman, J. G.;

Rodnyansky, A. E.; Oliver, A. G.; Boggess, W. C.; Muldoon, J., *Nat. Commun.* **2011**, 2, 427.

(13) Barile, C. J.; Spatney, R.; Zavadil, K. R.; Gewirth, A. A., *J. Phys. Chem. C* **2014**, 118, 10694.

(14) Mohtadi, R.; Matsui, M.; Arthur, T. S.; Hwang, S.-J., *Angew. Chem. Int. Ed.* **2012**, 51, 9780.

(15) Doe, R. E.; Han, R.; Hwang, J.; Gmitter, A. J.; Shterenberg, I.; Yoo, H. D.; Pour, N.; Aurbach, D., *Chem. Commun.* **2013**, 50, 243.

(16) Shao, Y.; Liu, T.; Li, G.; Gu, M.; Nie, Z.; Engelhard, M.; Xiao, J.; Lv, D.; Wang, C.; Zhang, J.-G.; Liu, J., *Sci. Rep.* **2013**, 3, 3130.

(17) Ha, S.-Y.; Lee, Y.-W.; Woo, S. W.; Koo, B.; Kim, J.-S.; Cho, J.; Lee, K. T.; Choi, N.-S., *ACS Appl. Mater. Interfaces* **2014**, 6, 4063.

(18) Orikasa, Y.; Masese, T.; Koyama, Y.; Mori, T.; Hattori, M.; Yamamoto, K.; Okado, T.; Huang, Z.-D.; Minato, T.; Tassel, C.; Kim, J.; Kobayashi, Y.; Abe, T.; Kageyama, H.; Uchimoto, Y., *Sci. Rep.* **2014**, 4, 5622.

(19) Fukutsuka, T.; Asaka, K.; Inoo, A.; Yasui, R.; Miyazaki, K.; Abe, T.; Nishio, K.; Uchimoto, Y., *Chem. Lett.* **2014**, 43, 1788.

(20) Carter, T. J.; Mohtadi, R.; Arthur, T. S.; Mizuno, F.; Zhang, R.; Shirai, S.; Kampf, J. W., *Angew. Chem. Int. Ed.* **2014**, 53, 3173.

(21) Shterenberg, I; Salama, M.; Yoo, H. D.; Gofer, Y.; Park, J.-B.; Sun, Y. –K.; Aurbach, D., *J. Electrochem. Soc.* **2015**, 162, A7118.

(22) Shao, Y.; Rajput, N. N.; Hu, J.; Hu, M.; Liu, T.; Wei, Z.; Gu, M.; Deng, X.; Xu, S.; Han, K. S.; Wang, J.; Nie, Z.; Li, G.; Zavadil, K. R.; Xiao, J.; Wang, C.; Henderson, W. A.; Zhang, J. –G.; Wang, Y.; Mueller, K. T.; Persson, K.; Liu, J., *Nano Energy.* **2015**, 12, 750.

(23) Rajput, N. N.; Qu, X.; Sa, N.; Burrell, A. K.; Persson, K. A., *J. Am. Chem. Soc.***2015**, 137, 3411.

(24) Watkins, T.; Kumar, A.; Buttry, D. A., *J. Am. Chem. Soc.* **2016**, 138, 641.

(25) Arthur, T. S.; Glans, P. –A.; Singh, N.; Tutusaus, O.; Nie, K.; Liu, Y. –S.; Mizuno, F.; Guo, J.; Alsem, D. H.; Salmon, N. J.; Mohtadi, R., *Chem. Mater.* **2017**, 29, 7183.

(26) Chang, J.; Haasch, R. T.; Kim, J. –W.; Spila, T.; Braun, P. V.; Gewirth, A. A.; Nuzzo, R. G., *ACS Appl. Mater. Interfaces* **2015**, 7, 2494.

(27) Nakayama, Y.; Kudo, Y.; Oki, H.; Yamamoto, K.; Kitajima, Y.; Noda, K. *J. Electrochem. Soc.* **2008**, 155, A754.

(28) Wan, L. F.; Prendergast, D., *J. Am. Chem. Soc*. **2014**, 136, 14456.

(29) Ravel, B.; Newville, M., *J. Synchrotron Rad.* **2005**, 12, 537.

(30) Taylor, R. C.; Schultz, D. R.; Emery, A. R., *J. Am. Chem. Soc*. **1958**, 80, 27.

(31) Emery, A. R.; Taylor, R. C., *J. Chem. Phys.* **1958**, 28, 1029.

(32) Shirk, A. E.; Shriver, D. F., *J. Am. Chem. Soc.* **1973**, 95, 5904.

(33) Marks, T. J.; Kolb, J. R., *Chem. Rev.* **1977**, 77, 263.

(34) Cerny, R.; Filinchuk, Y.; Hagemann, H.; Yvon, K., *Angew. Chem. Int., Ed.* **2007**, 46, 5765.

(35) Parker, S. F., *Chem. Rev.* **2010**, 254, 215.

(36) Muetterties, E. L.; Merrifield, R. E.; Miller, H. C.; Knoth, W. H. Jr.; Dowing, J. R., *J. Am. Chem. Soc.* 1962, 84. 2506.

(37) Ohara, K.; Umebayashi, Y.; Ichitsubo, T.; Matsumoto, K.; Hagiwara, R.; Arai, H.; Mori, M.; Orikasa, Y.; Okamoto, S.; Oishi, M.; Aiso, Y.; Nohira, T.; Uchimoto, Y.; Ogumi, Z.; Matsubara, *RSC Adv.* 2015, 5, 3063.

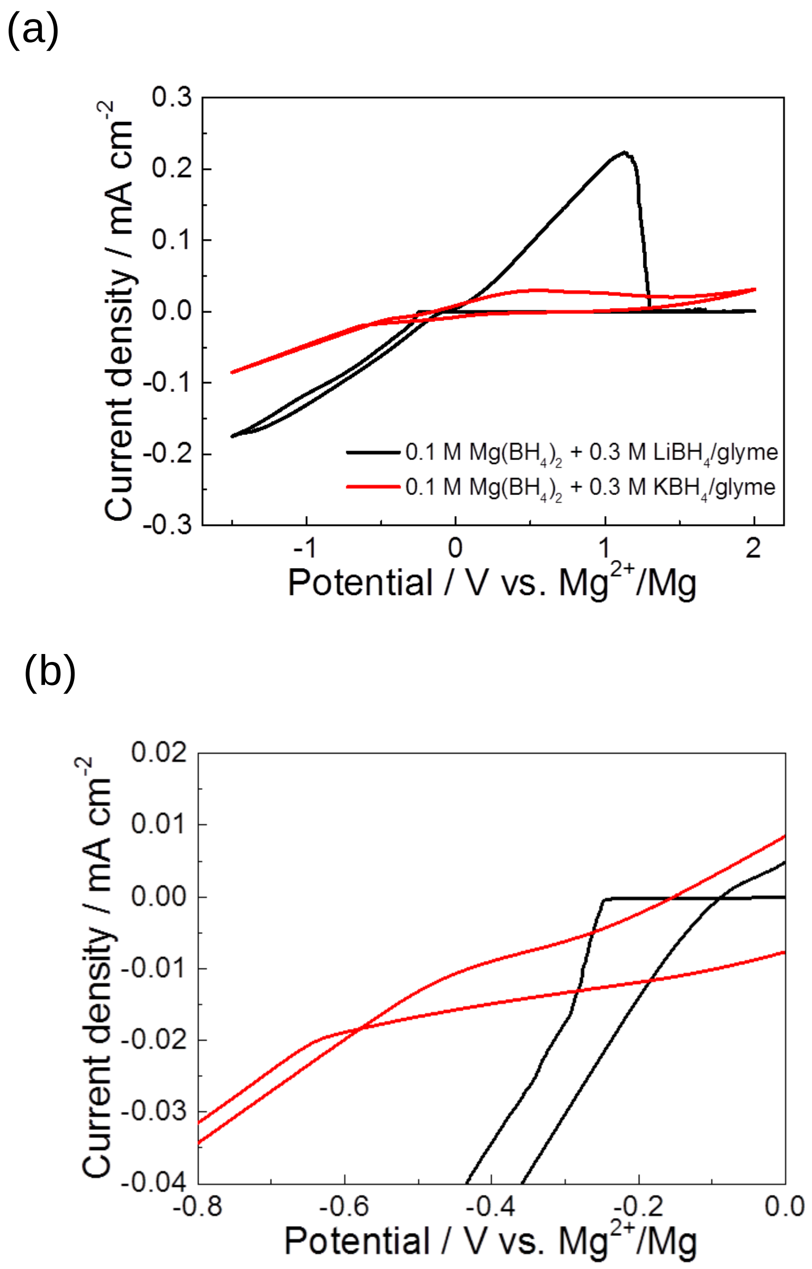

Figure 5-1. (a) Cyclic voltammograms of bismuth electrode in 0.1 M $Mg(BH_4)_2$ + 0.3 M $LIBH_4$/glyme and 0.1 M $Mg(BH_4)_2$ + 0.3 M KBH_4/glyme at a scanning rate of 5 mV/sec. (b) Enlarged figure of (a) between -0.9 V and 0 V (vs. Mg^{2+}/Mg).

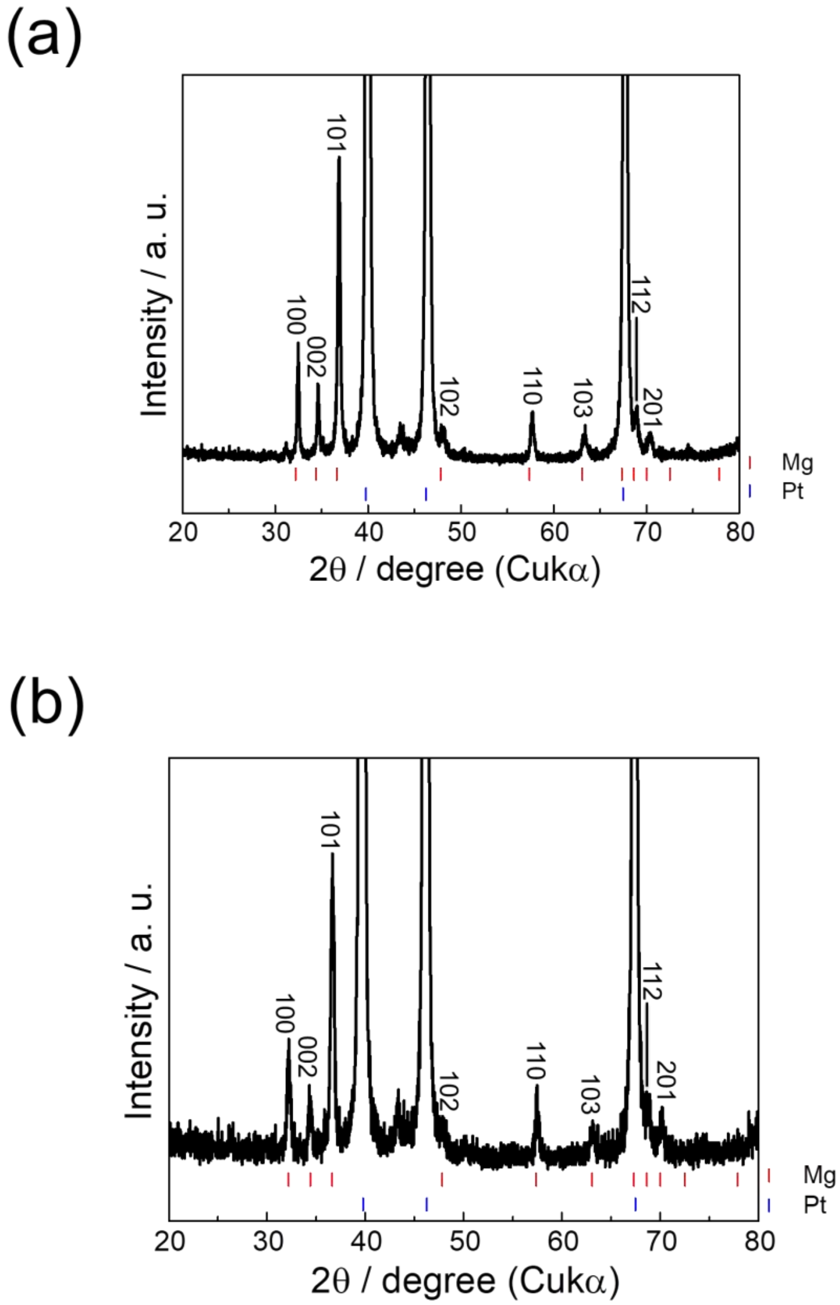

Figure 5-2. XRD patterns of electrodeposited of (a) 0.1 M $Mg(BH_4)_2$ + 0,3 M $LiBH_4$/glyme and (b) 0.1 M $Mg(BH_4)_2$ + 0.3 M KBH_4/glyme on Pt substrate after electrochemical measurements.

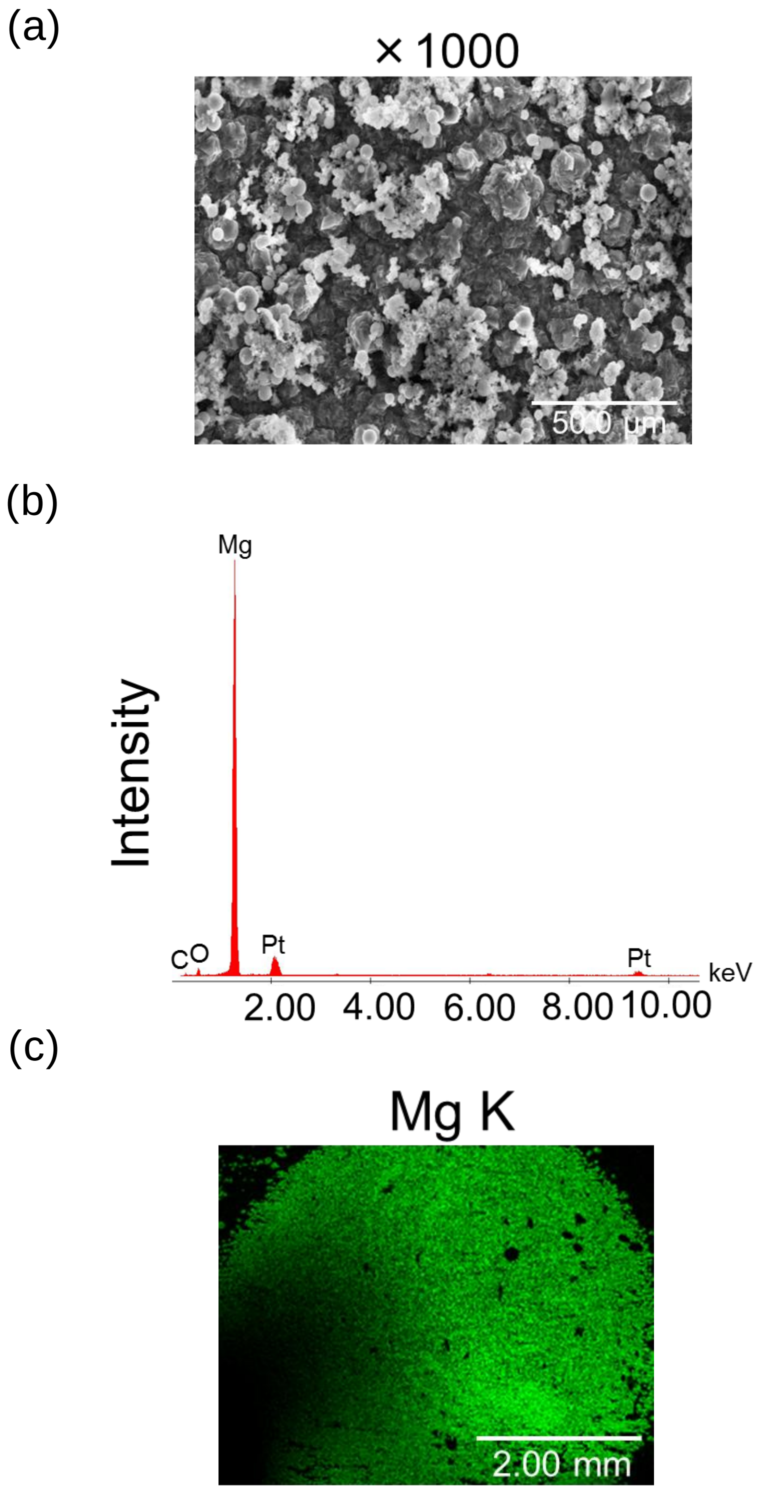

Figure 5-3. (a) SEM image, (b) EDX spectrum and (c) EDX mapping of Mg K for electrodeposited on Pt substrate after electrochemical measurement in 0.1 M $Mg(BH_4)_2$ + 0.3 M $LIBH_4$/glyme.

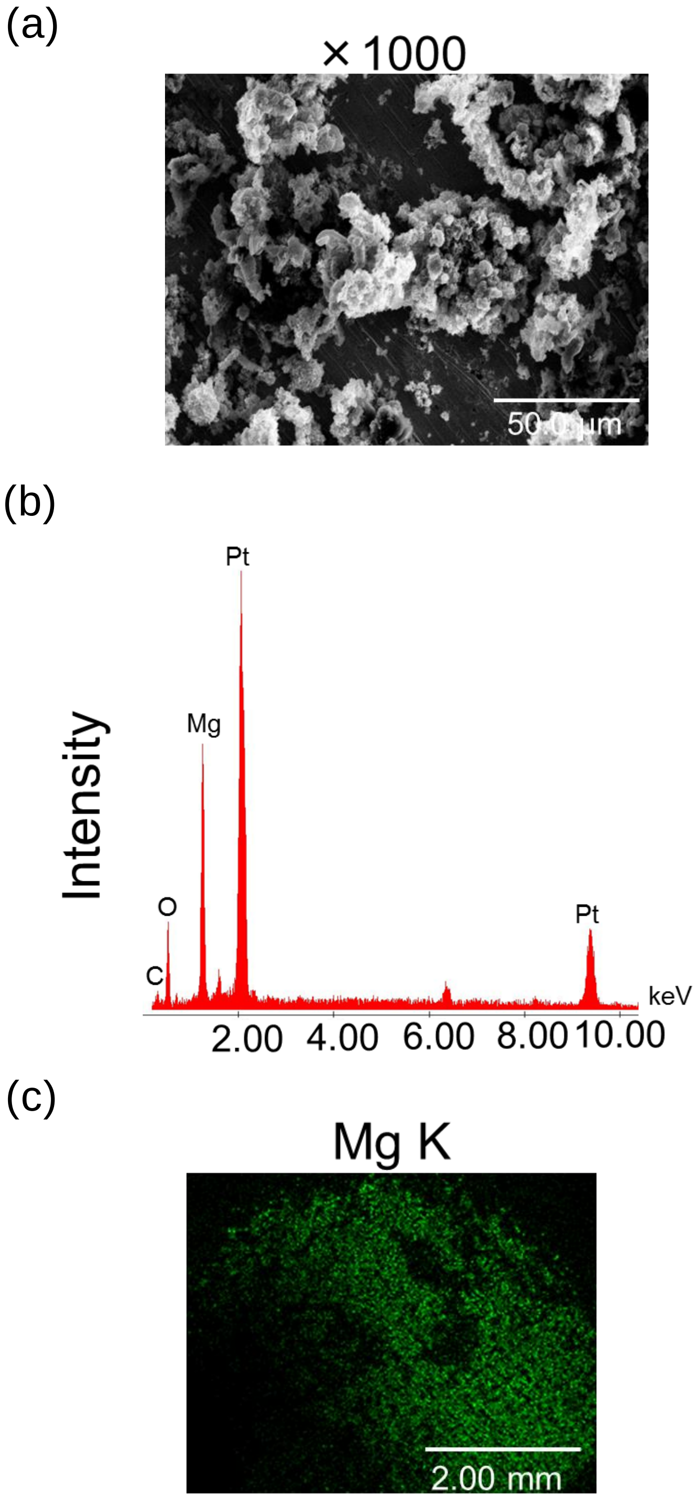

Figure 5-4. (a) SEM image, (b) EDX spectrum and (c) EDX mapping of Mg K for electrodeposited bismuth on Pt substrate after electrochemical measurement in 0.1 M $Mg(BH_4)_2$ + 0.3 M KBH_4/glyme.

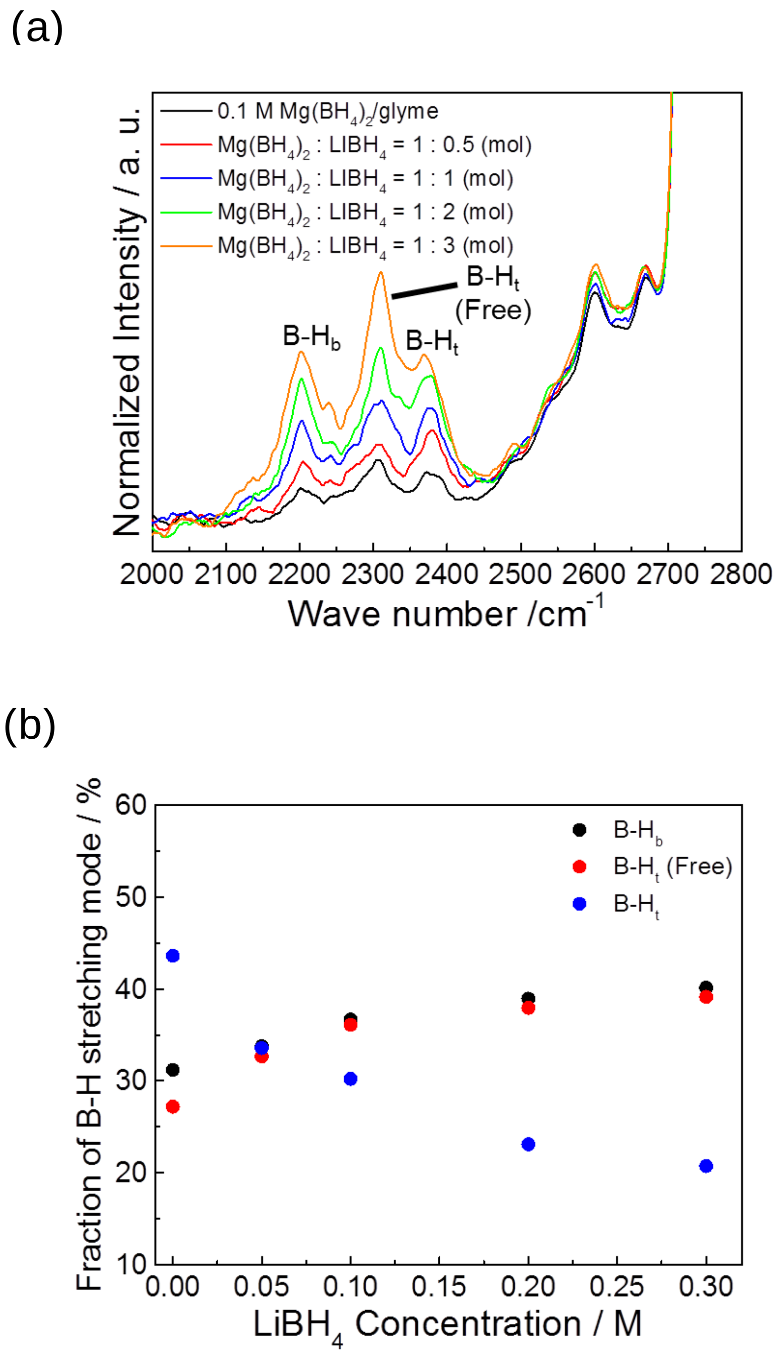

Figure. 5-5. Raman spectra of (a) 0.1 M Mg(BH$_4$)$_2$ + LiBH$_4$/glyme in several concentration in the region between 2000 and 2800 cm^{-1}. (b) Fraction of solvate species of BH$_4$ anion of 0.1 M Mg(BH$_4$)$_2$ + LiBH$_4$/glyme in several concentration. b : bridging. t : terminal coordinations.

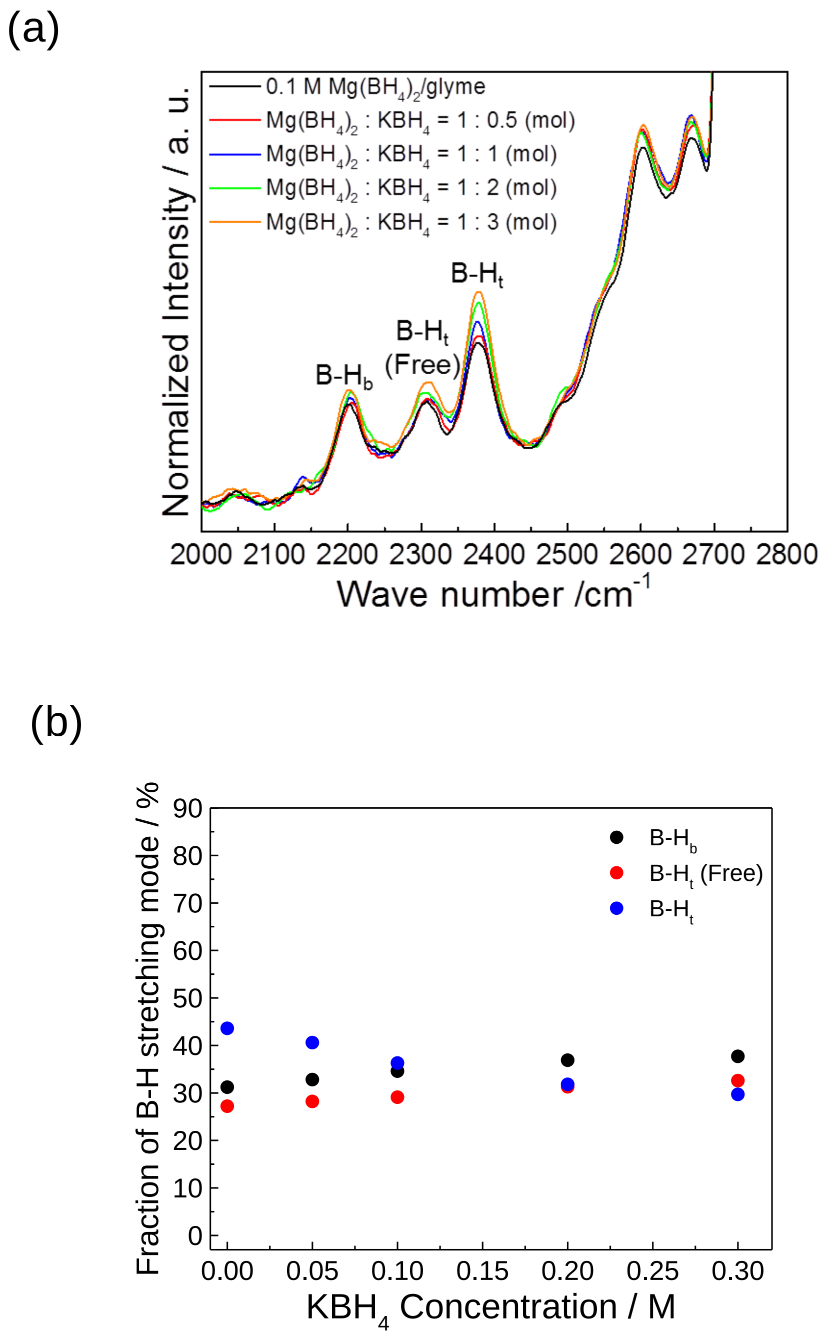

Figure 5-6. Raman spectra of (a) 0.1 M Mg(BH$_4$)$_2$ + KBH$_4$/glyme in several concentration in the region between 2000 and 2800 cm^{-1}. (b) Fraction of solvate species of BH$_4$ anion of 0.1 M Mg(BH$_4$)$_2$ + KBH$_4$/glyme in several concentration. b : bridging. t : terminal coordinations.

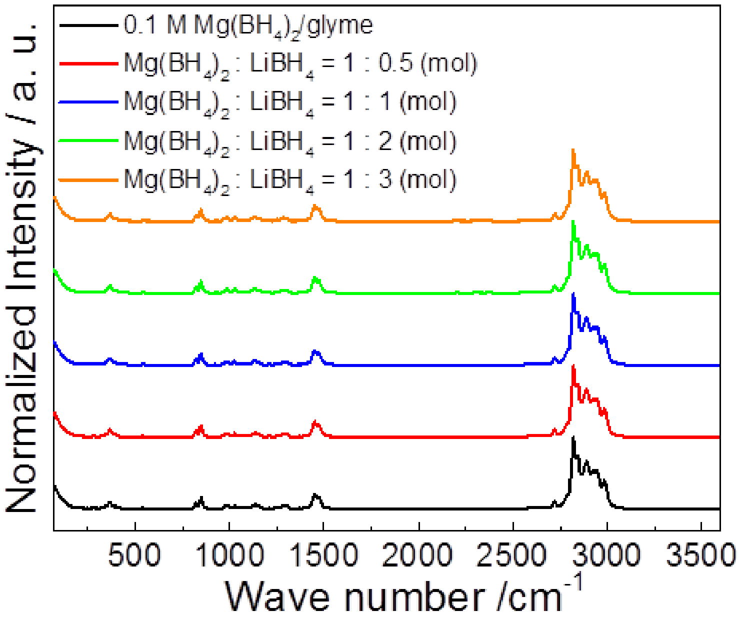

Figure 5-7. Raman spectra of the 0.1 M $Mg(BH_4)_2$ + $LiBH_4$/glyme for 70 – 3600 cm^{-1}.

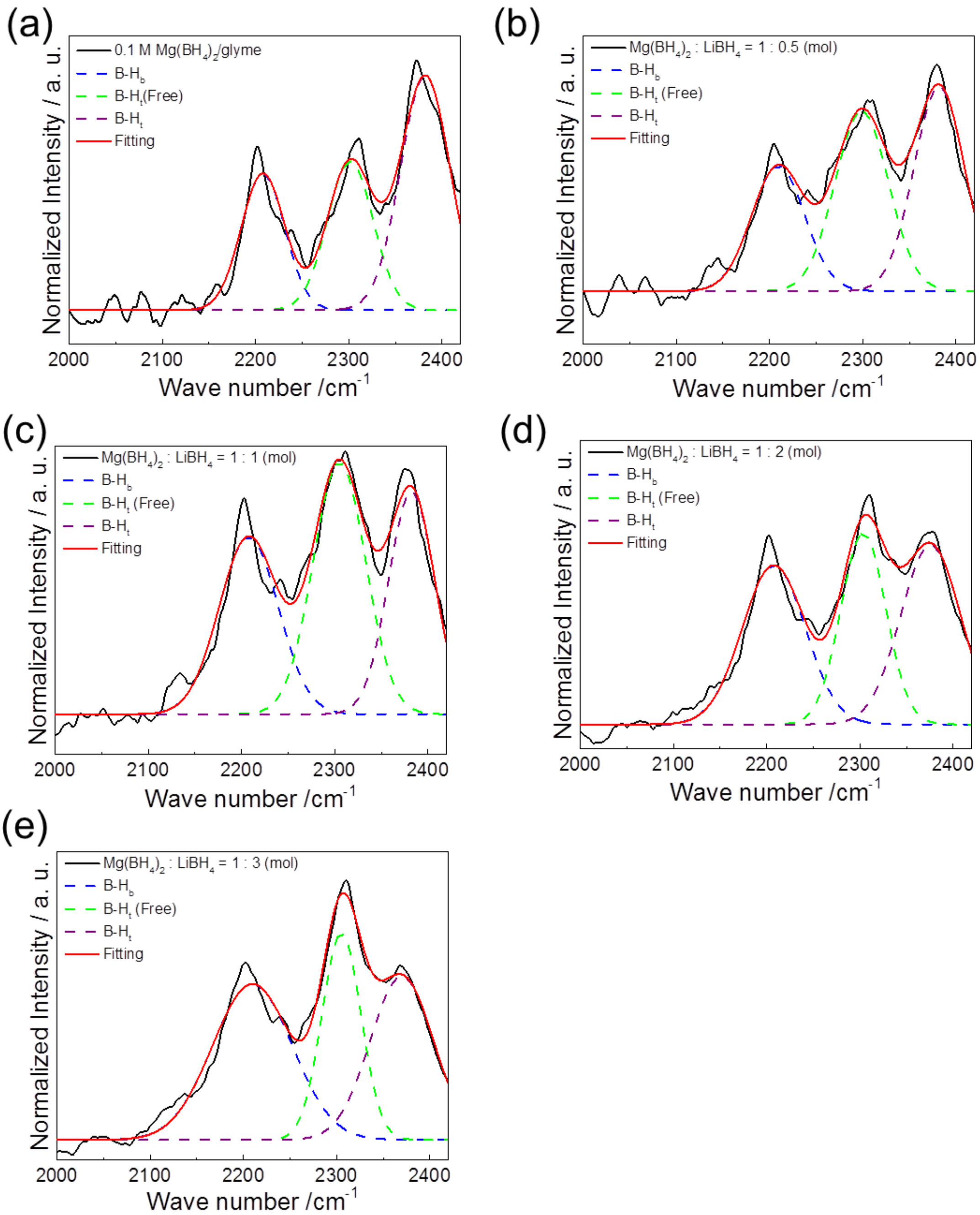

Figure. 5-8. Raman spectra and Gaussian fitting results of 0.1 M $Mg(BH_4)_2$ + $LiBH_4$/glyme in several concentration in the region between 2100 and 2500 cm^{-1}

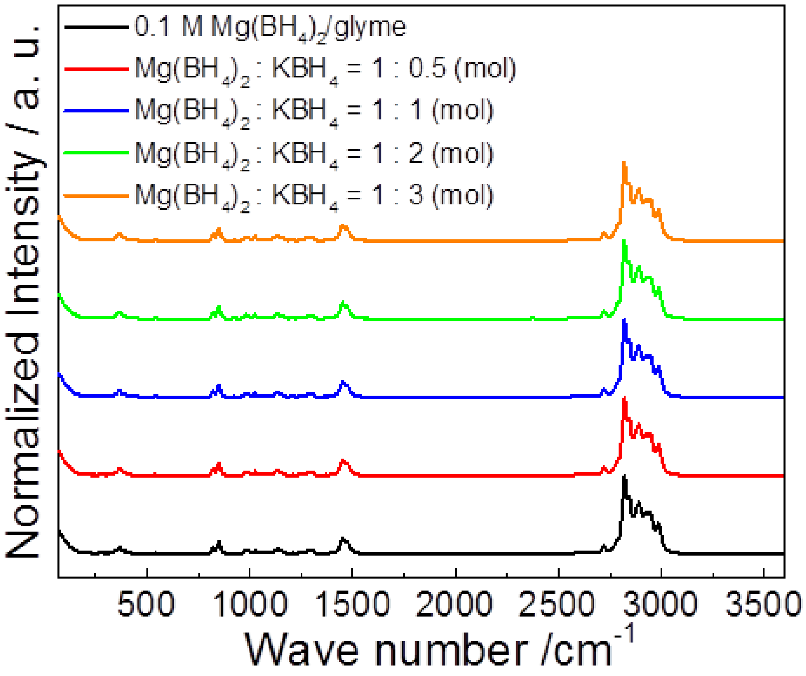

Figure. 5-9. Raman spectra of the 0.1 M $Mg(BH_4)_2$ + KBH_4/glyme for $70 – 3600\ cm^{-1}$.

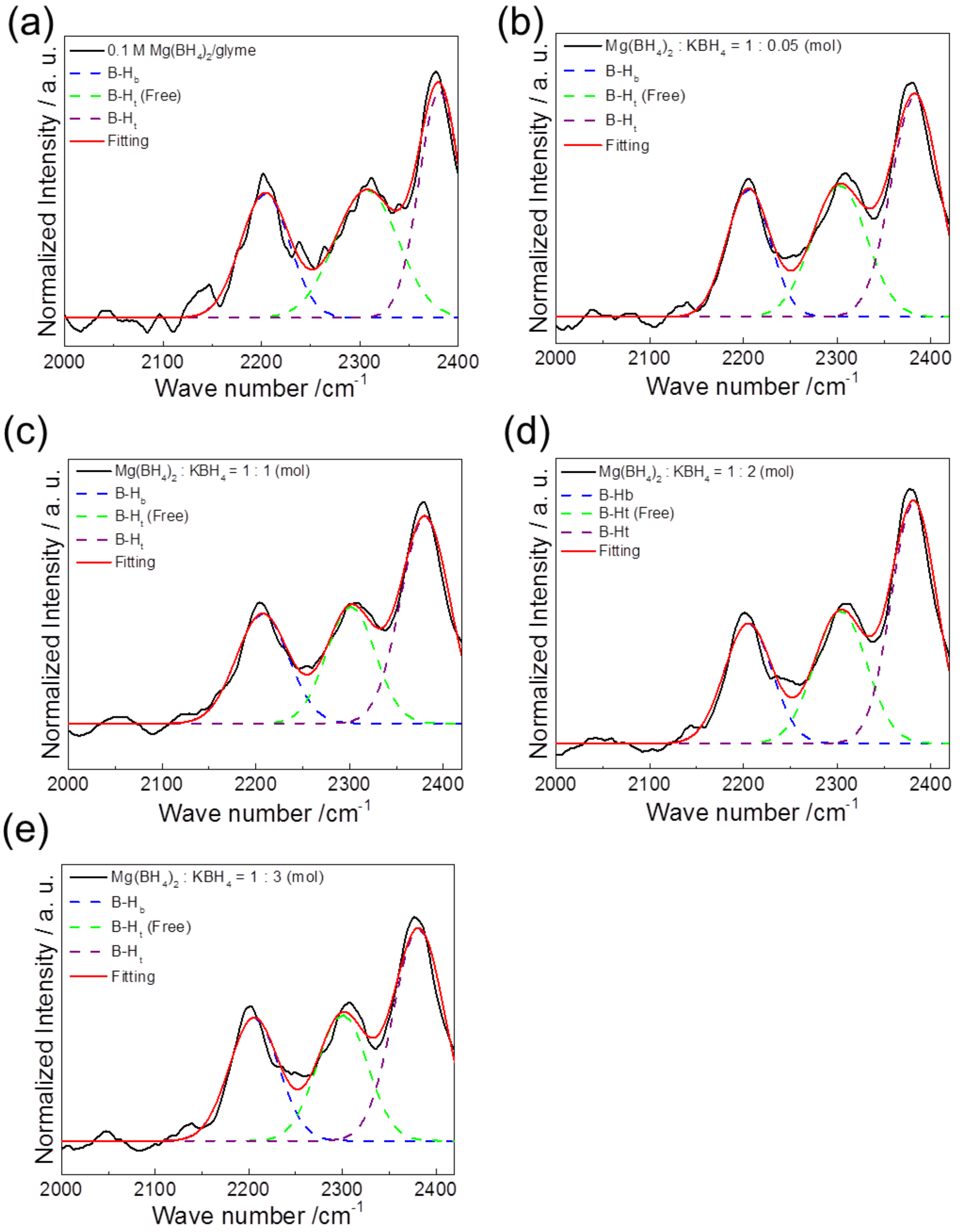

Figure. 5-10. Raman spectra and Gaussian fitting results of0.1 M $Mg(BH_4)_2$ + KBH_4/glyme in several concentration in the region between 2100 and 2500 cm^{-1}

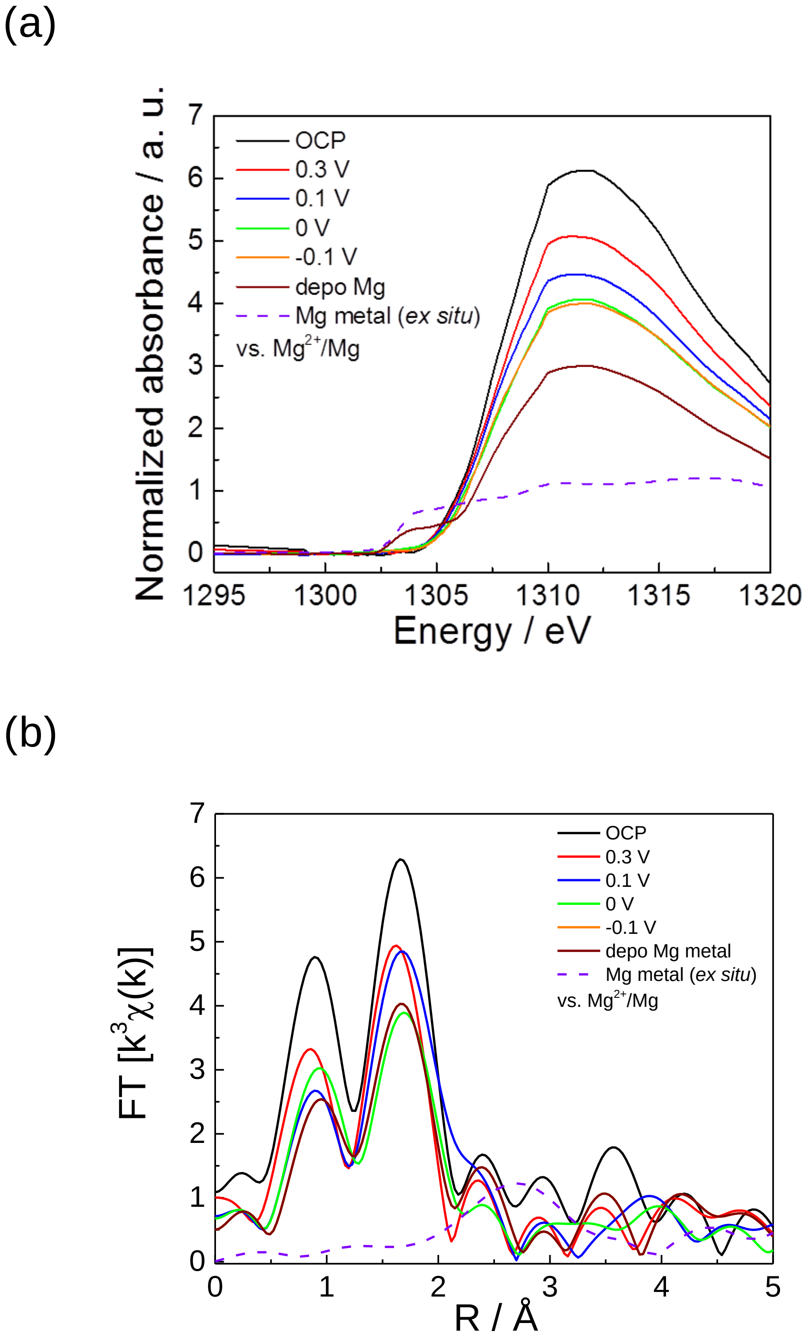

Figure. 5-11. Mg *K*-edge (a) XANES and (b) Fourier-transformed EXAFS spectra obtained from *operando* XAS measurements 0.1 M $Mg(BH_4)_2$ + 0.3 M $LiBH_4$/glyme. The potential is expressed on vs. Mg^{2+}/Mg.

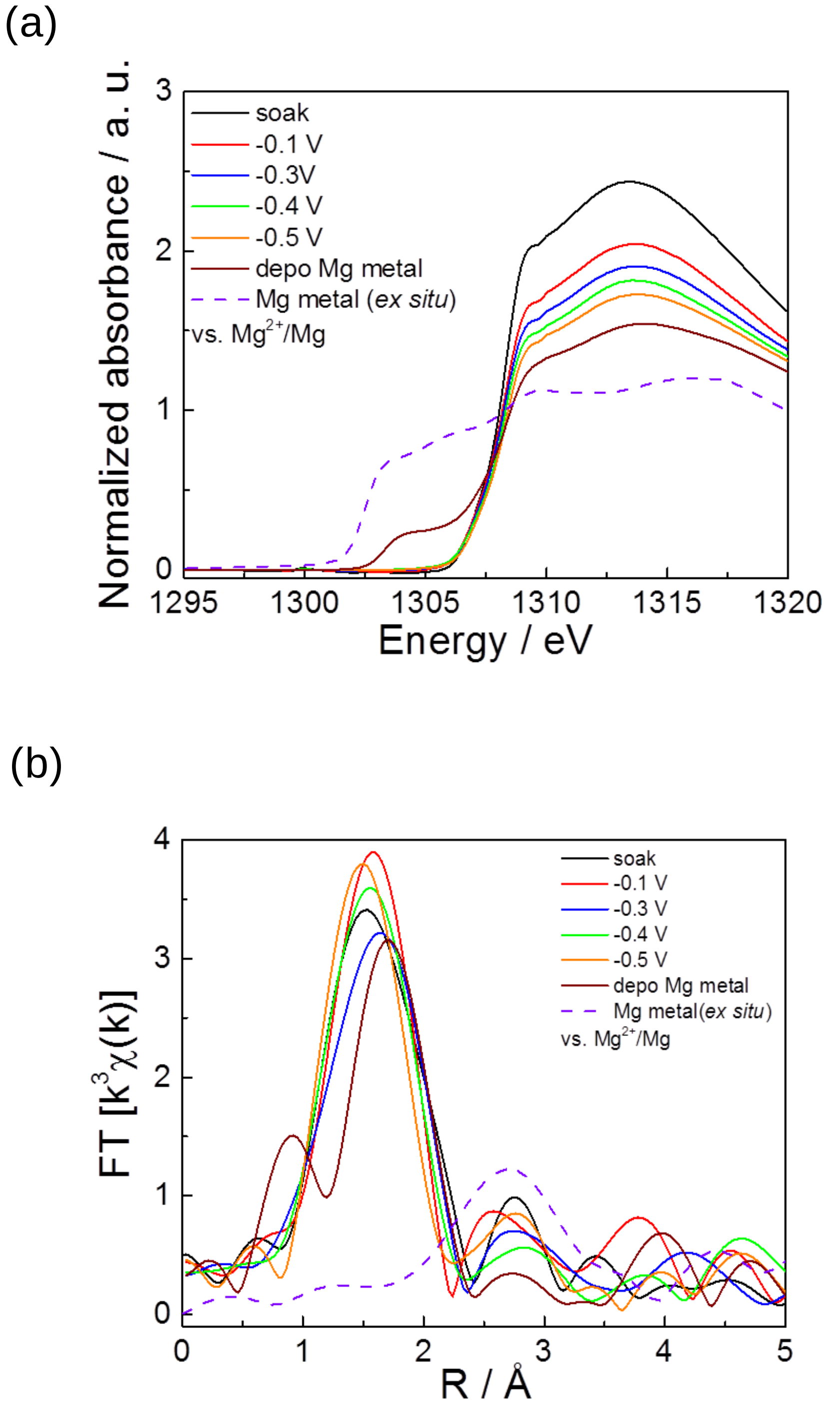

Figure. 5-12. Mg *K*-edge (a) XANES and (b) Fourier-transformed EXAFS spectra obtained from *operando* XAS measurements 0.1 M $Mg(BH_4)_2$ + 0.3 M KBH_4/glyme. The potential is expressed on vs. Mg^{2+}/Mg.

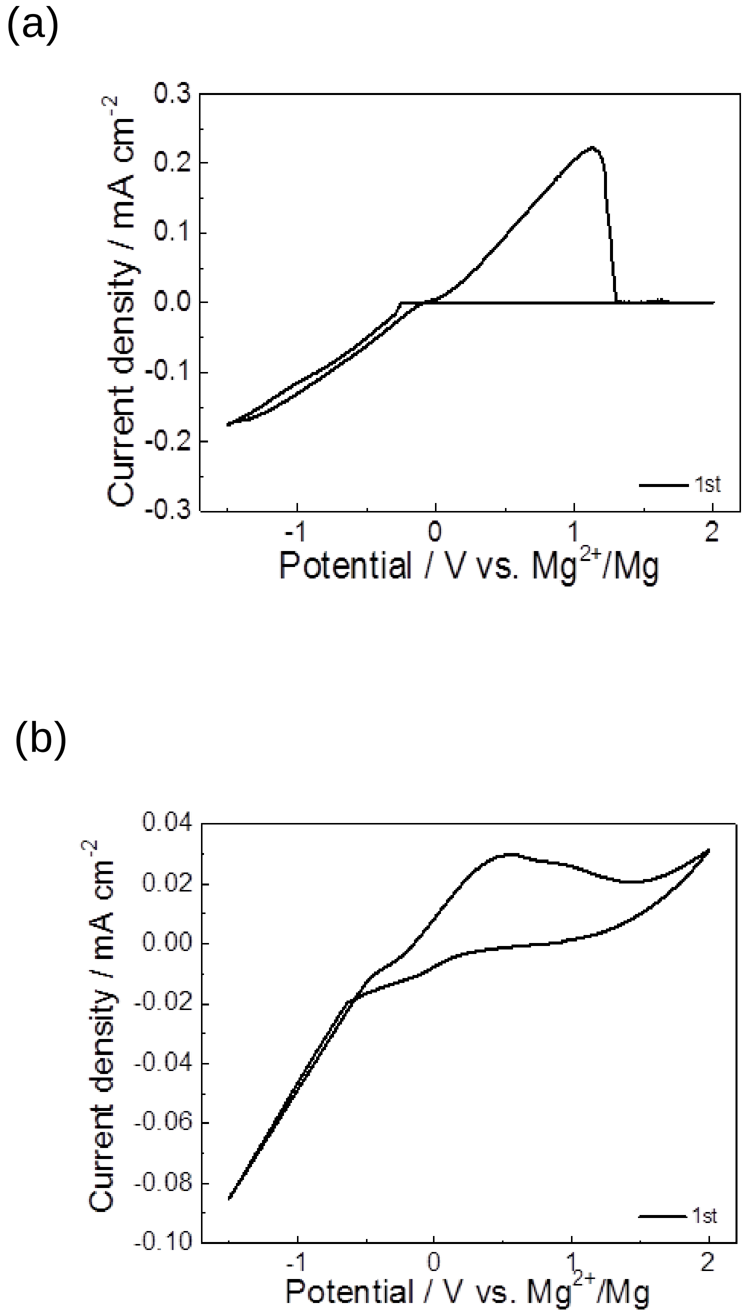

Fig. 5-13. Cyclic voltammograms of (a) 0.1 M $Mg(BH_4)_2$ + 0.3 M $LiBH_4$/glyme and (b) 0.1 M $Mg(BH_4)_2$ + 0.3 M KBH_4/glyme using *operando* XAS cell.

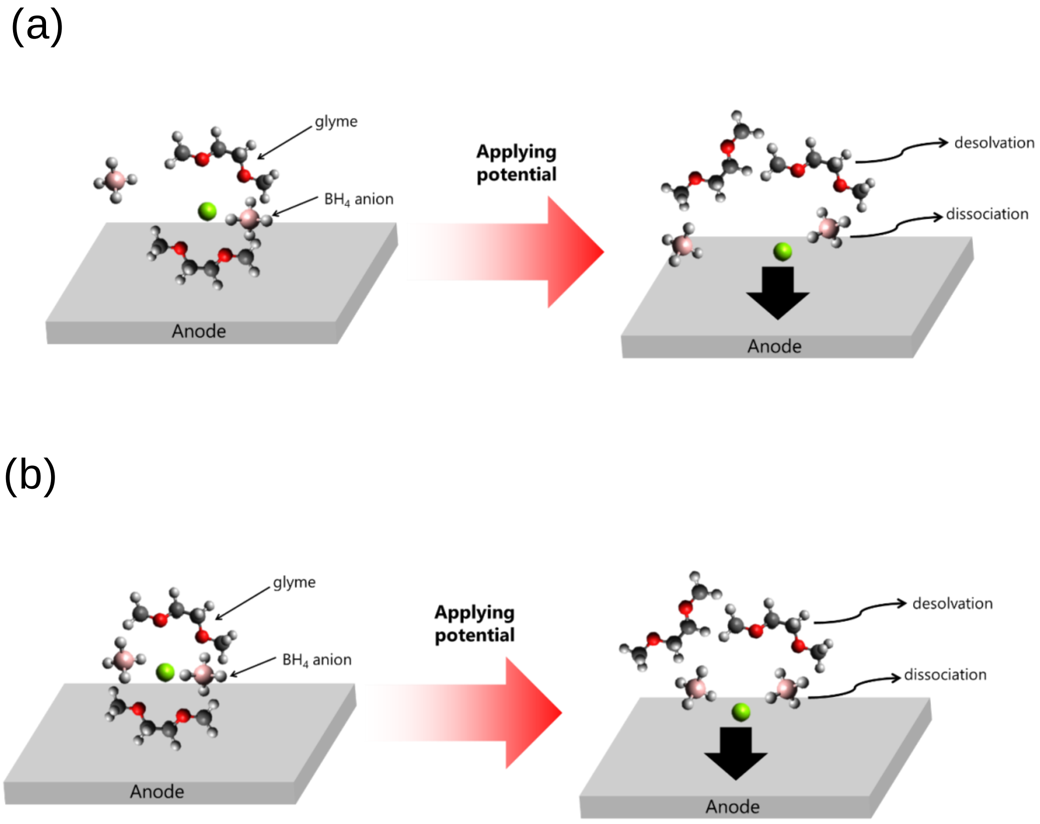

Fig. 5-14. Schematic illustrations of the behavior of magnesium ion at negative electrode/electrolyte interface in the (a) 0.1 M $Mg(BH_4)_2$ + 0.3 M $LiBH_4$/glyme, (b) 0.1 M $Mg(BH_4)_2$ + 0.3 M KBH_4/glyme.

Chapter 6: General Conclusions

Magnesium rechargeable batteries are one of the candidates for the next generation batteries, because high energy density, low cost and safety. However, the combination of electrolytes and anode being studied is limited. In order to establish the material design guideline of electrolyte, it is desired to elucidate the anode reaction mechanism. In this study, we have developed *operando* soft X-ray absorption spectroscopy measurement system and apply to the analysis of electronic and local structure of electrolyte during magnesium metal deposition reaction or magnesium ion insertion reaction. Furthermore, bulk structure of electrolyte is investigated by Raman spectroscopy.

In chapter 1, the necessity of magnesium rechargeable batteries was described. We reported the past magnesium rechargeable battery electrolytes and anode. The importance of understanding the anode reaction mechanism in magnesium rechargeable batteries was presented, especially focusing on the interface between electrolytes and anodes were reviewed.

In chapter 2, the coordination structures of TFSA anion based electrolyte during magnesium metal deposition reaction were investigated by Raman spectroscopy and *operando* XAS measurements. TFSA anions do not coordinate with magnesium ions in $Mg(TFSA)_2$/triglyme system, while TFSA anions strongly coordinate with magnesium ions in $Mg(TFSA)_2$/2-MeTHF system. In $Mg(TFSA)_2$/triglyme, magnesium ions are enable to approach anode by applying potential, because TFSA anions are not coordinated with magnesium ions. On the other hand, magnesium metal deposition reaction does not occur, because the bond between magnesium ions and TFSA anions does not be broken. Then, magnesium ions does not approach anode by applying potential.

In chapter 3, we investigated bismuth anode reaction mechanism via Raman spectroscopy and *operando* XAS measurements. TFSA anions contain uncoordinated states with magnesium ions in $Mg(TFSA)_2$/acetonitrile system. By *operando* soft X-ray absorption spectroscopy measurements, we revealed that desolvation reaction occurs in $Mg(TFSA)_2$/acetonitrile and $Mg(TFSA)_2$/2-MeTHF system. Magnesium ion insertion reaction occurs in $Mg(TFSA)_2$/acetonitrile, because TFSA anions do not inhibit for magnesium ions to approach anode surface. However the magnesium ion insertion reaction does not occur in $Mg(TFSA)_2$/2-MeTHF system, because TFSA anions, which strongly coordinate with magnesium ions, inhibit for magnesium ions to approach anode surface.

In chapter 4, the coordination structures of BH_4 anion based electrolyte during magnesium metal deposition reaction were investigated by Raman spectroscopy and *operando* XAS measurements. In the case of $Mg(BH_4)_2$/THF system, the all BH_4 anions were coordinated with magnesium ions. However, the BH_4 anions exists that uncoordinated states with magnesium ions in the case of $Mg(BH_4)_2$/glyme system. In $Mg(BH_4)_2$/THF, it is difficult to magnesium metal deposition reaction, because it is difficult to dissociate BH_4 anions . On the other hands, it is easy to magnesium metal deposition reaction, because it is easy to dissociate BH_4 anions.

In chapter 5, In the case $Mg(BH_4)_2$/glyme added with $LiBH_4$, the ratio of uncoordinated state of BH_4 anion is increasing. Then, magnesium metal deposition reaction tends to occur in $Mg(BH_4)_2$ + $LIBH_4$/glyme system. On the other hand, in the case of $Mg(BH_4)_2$/glyme added with KBH_4, the ratio of uncoordinated state of BH_4 anion does not increase. Magnesium metal deposition reaction hardly occurs in $Mg(BH_4)_2$ + KBH_4/glyme system..

In chapter 6, the results of this thesis were summarized. By using Raman spectroscopy and *operando* XAS measurements, it is demonstrated that the interaction between magnesium ion and anion plays important role of the anode reaction mechanism of magnesium rechargeable batteries. This paper mainly focused on the coordination structures in the electrolyte and at interface between anode and electrolyte. For further improvement of design guideline for magnesium rechargeable batteries, it is necessary to understand the behavior of kinetic magnesium ions at the interface between anode and electrolyte.

Acknowledgements

The study has been carried out at Graduate School of Human and Environmental Studies, Kyoto University.

First of all, I would like to express the deepest appreciation to Prof. Yoshiharu Uchimoto at Graduate School of Human and Environmental Studies, Kyoto University, for his accurate research guidance and numerous valuable advices.

I would like to offer my special thanks to Dr. Kentaro Yamamoto at Graduate School of Human and Environmental Studies, Kyoto University, for his useful comments and discussions.

I would like to appreciate Dr. Yuki Orikasa at Department of Applied Chemistry, Ritsumeikan University, for his effective suggestions. I would also like to appreciate Dr. Koji Nakanishi at Research organization of science and engineering, Ritsumeikan University, and Dr. Tomoki Uchiyama at Graduate School of Human and Environmental Studies, Kyoto University, Yusuke Tamenori at Research & Utilization Division, Japan Synchrotron Radiation Research Institute for their helps on measuring XAFS spectra. I would like to express my graduate to Ashu Choudhary and Yoshitaka Tateyama at Center for Green Research on Energy and Environmental Materials, National Institute for Materials Science, Keitaro Sodeyama at International Center for Materials Nanoarchitectonics, National Institute for Materials Science, for their helps on calculating Density functional theory calculations.

I am grateful to Toshihiko Mandai and Tatsuya Takeguchi at Graduate School of Engineering, Iwate University, Masaki Matsui at Department of Chemical Science and Engineering, Kobe University and Kiyoshi Kanamura at Department of Applied Chemistry, Graduate School of Urban Environmental Sciences, Tokyo Metropolitan University, for their effective discussions and advices to writing papers.

I am deeply grateful to Prof. Hisao Yoshida and Prof. Mitsuo Tosaki at Graduate School of Human and Environmental Studies, Kyoto University for their helpful comments of this thesis.

I would like to thank to all the members of Prof. Uchimoto's laboratory for their helps, discussions and encouragement.

Finally, I would like to appreciate my parents and my brother for their understanding, support and encouragement.

Masashi Hattori

Kyoto, JAPAN

October, 2018